

BOSTON UNIVERSITY
SCHOOL OF ENGINEERING

Dissertation

THE DEVELOPMENT AND VALIDATION OF HYBRID FREQUENCY-DOMAIN AND BROADBAND DIFFUSE OPTICAL SPECTROSCOPY FOR MONITORING TISSUE WATER CONTENT DURING HEMODIALYSIS

by

DIANA JACQUELINE SUCIU

B.S., Case Western Reserve University, 2017
M.S., Case Western Reserve University, 2018

Submitted in partial fulfillment of the
requirements for the degree of
Doctor of Philosophy

2025

© 2025 by
DIANA JACQUELINE SUCIU
All rights reserved

Approved by

First Reader

Darren M. Roblyer, Ph.D.
Professor of Biomedical Engineering
Professor of Electrical and Computer Engineering

Second Reader

Irving J. Bigio, Ph.D.
Professor of Biomedical Engineering
Professor of Electrical and Computer Engineering
Professor of Physics
Professor of Medicine

Third Reader

Vipul C Chitalia, MD, PhD.
Professor of Pathology & Laboratory Medicine
Boston University, School of Medicine

Fourth Reader

Aurelie Ewards, PhD
Research Professor of Biomedical Engineering

Fifth Reader

Kavon Karrobi, Ph.D.
Lecturer of Biomedical Engineering

DEDICATION

To all my friends and family

ACKNOWLEDGMENTS

I would like to begin by expressing my deepest gratitude to my advisor, Dr. Darren Roblyer, for their guidance, encouragement, and unwavering support throughout my doctoral studies. His mentorship has not only shaped the direction of this dissertation but also greatly influenced my development as a scientist and engineer. I am also grateful to my dissertation committee members, Dr. Irving Bigio, Dr. Aurelie Edwards, and Dr. Kavon Karrobi, for their insightful feedback, constructive criticism, and valuable suggestions that strengthened this work.

I wish to especially thank Dr. Vipul Chitalia, and his lab specifically Isaac and Pranav for being my collaborators and colleagues during the clinical trial. Your contributions and discussions played a central role in advancing this research.

I would like to thank all of the study participants for their time and patience, helping me collect data.

Additionally, within the Roblyer lab, I am indebted to Lina, Eric, and Thao for their technical and computational assistance, thoughtful input that made this work possible. I would also like to acknowledge the contributions of past and present lab members, whose dedication and teamwork created an environment of innovation and support. Special thank you to Raeef, Carlos, Anahita, and Sam for being my predecessors and guiding me and creating a supportive lab culture.

I gratefully acknowledge funding from the National Institutes of Health, National Institute of Diabetes and Digestive and Kidney Diseases (Grant No. R21DK132784), whose resources were essential for carrying out the studies described here.

Finally, I would like to extend my heartfelt thanks to my family and friends. Thank you all, your love and support has been a constant source of strength and comfort throughout this journey.

**THE DEVELOPMENT AND VALIDATION OF HYBRID FREQUENCY-
DOMAIN AND BROADBAND DIFFUSE OPTICAL SPECTROSCOPY FOR
MONITORING TISSUE WATER CONTENT DURING HEMODIALYSIS**

DIANA JACQUELINE SUCIU

Boston University College of Engineering, 2025

Major Professor: Darren M. Roblyer, Ph.D., Professor of Biomedical Engineering,
Professor of Electrical and Computer Engineering

ABSTRACT

Poor fluid management during hemodialysis in patients with end-stage kidney disease (ESKD) contributes to adverse clinical outcomes. Current clinical tools for assessing volume status, such as Crit-Line hematocrit monitoring, are limited in their predictive capability, underscoring the need for objective and quantitative measurement techniques. To address this gap, a frequency-domain and broadband near-infrared spectroscopy (FD-Bb-NIRS) system was developed to continuously and noninvasively monitor tissue optical properties in patients undergoing hemodialysis.

The FD-Bb-NIRS system integrates frequency-domain (FD) and continuous-wave (CW) diffuse optical spectroscopy (DOS) measurements to recover absolute absorption and reduced scattering spectra over the 700 to 1000 nm. These measurements were integrated using model-based analysis to provide broadband absorption and reduced scattering spectra. Beer's law was used to extract tissue chromophore concentrations.

Across 27 hemodialysis sessions, the Water Ratio ($[\text{Water}]/([\text{Water}] + [\text{Lipid}])$) was the only chromophore based metric that was significantly different between subjects with (N=18) and without (N=9) intradialytic adverse events ($p = 0.0313$), with a decrease observed in patients without adverse events. Additionally, a multivariate discriminant analysis combining Δ Water Ratio, scattering amplitude (A) and slope (b) achieved the highest classification performance (AUC = 0.88). An analysis of these features also demonstrated predictive power at earlier timepoints, indicating potential for pre-symptomatic identification of patients at risk (AUC=0.93 at 25% dialysis completion, with respect to total dialysis time).

While these results are promising, further improvements in tissue water quantification could enhance the accuracy of monitoring. To address this need, the FD-Bb-NIRS system was extended to incorporate measurements in the short-wave infrared (SWIR) range (900–1300 nm). Extending frequency domain diffuse optical spectroscopy (FD-DOS) into the short-wave infrared region has the potential to improve measurements of key biological tissue chromophores such as water and lipids, given their higher absorption in SWIR compared with near-infrared wavelengths. Few studies have explored FD-DOS in the SWIR range.

The first demonstration of a frequency domain broadband SWIR spectroscopy (FD-Bb-SWIRS) system was developed to measure optical properties from 685 to 1300 nm. A custom hybrid system was developed, combining frequency domain measurements from 685 to 980 nm at discrete wavelengths with broadband continuous wave measurements from 900 to 1300 nm. This setup provided absolute absorption (μ_a) spectra from 685 to

1300 nm. Validation was performed using mineral oil-based solid phantoms, deuterium oxide (D_2O) liquid phantoms, and desiccating porcine tissue.

The FD-Bb-SWIRS system was sensitive to changes in μ_a from varying concentrations of absorbers in solid and liquid phantoms. Ex vivo measurements of μ_a spectra indicated differences in tissue water content across different porcine tissue samples during baseline and desiccation. μ'_s values were within the anticipated range for both porcine tissue and phantom measurements. The FD-Bb-SWIRS system enables precise quantification of water in biological tissues. It represents a significant step forward in advancing SWIR-based optical spectroscopy for clinical applications.

TABLE OF CONTENTS

DEDICATION	iv
ACKNOWLEDGMENTS	v
ABSTRACT	vii
TABLE OF CONTENTS.....	x
LIST OF TABLES.....	xiv
LIST OF FIGURES	xv
LIST OF ABBREVIATIONS.....	xxi
CHAPTER 1: Introduction	1
1.1 Background.....	1
1.1.1 End Stage Kidney Disease Treatment and Current Limitations	1
1.1.2 Overview of Diffuse Optical Spectroscopy	3
1.1.3 Physics of Water in NIR and SWIR Wavelengths.....	5
1.2 Thesis Chapter Structure.....	9
1.3 Specific Aims.....	10
Chapter 2: Aim 1: Creation of FD-NIRS System	11
2.1 Background/Motivation	11
2.2 FD-Bb-NIRS Instrumentation.....	13
2.3 Data Processing for FD-Bb-NIRS	16
2.4 Monte Carlo Modeling Simulations.....	17
Chapter 3: Aim 2: Clinical Study.....	19
3.1 Introduction of Existing ESKD Clinical Fluid Management.....	19

3.2 Methods.....	20
3.2.1 Clinical Exponential Procedure	20
3.2.2 Chromophore Extraction.....	22
3.3 Results.....	24
3.3.1 Subject Overview.....	24
3.3.2 Adverse vs Non-Adverse Events Chromophores	<u>26</u> ²⁷
3.3.3 Tissue Scattering of Patients with Adverse vs Non-Adverse Events	30
3.3.4 Discriminant analysis.....	32
3.3.5 Comparison with Crit-Line and Blood Pressure Metrics.....	33
3.4 Discussion.....	35
3.5 Conclusion	40
Chapter 4: Aim 3: Develop and validate an FD-SWIRS system	41
4.1 Motivation/ Introduction.....	41
4.2 Materials and Methods.....	44
4.2.1 Wavelength Selection and Inverse Model considerations	44
4.2.2 Bb-FD-SWIRS Instrumentation.....	45
4.2.3 FD-Bb-SWIRS Data Processing Overview	49
4.3: Validation Experiments	52
4.3.1 In Vitro Validations on Mineral Oil based Phantoms.....	52
4.3.2 In Vitro Validation on D ₂ O liquid Phantoms.....	53
4.3.3 Ex vitro Validations on porcine samples during desiccation.....	53
4.4 Results.....	56

4.4.1 Uncertainty in Extracted Optical Properties using FD Model	56
4.4.2 In Vitro Validations on Mineral Oil based Phantoms.....	57
4.4.3 In Vitro Validation on D ₂ O liquid Phantoms.....	59
4.4.4 Ex vitro Validations on porcine samples during desiccation.....	60
4.5 Discussion	63
4.6 Conclusion	67
Chapter 5: Discussion and Conclusions.....	68
5.1 Summary of Findings.....	68
5.2 Impact and Innovations.....	69
5.3 Future Work	70
5.3.1 SWIRS Human Measurements (and updates to the FD-Bb-SWIRS System)	70
5.3.2 Multi-Layer Monte Carlo Simulations.....	72
5.3.3 Further Clinical Studies and Exploring the three-compartment model	73
5.4 Overall Conclusion	74
APPENDIX.....	75
Chapter 2 Appendix	75
Chapter 2 Supplemental Figures:.....	75
Chapter 3 Appendix	76
Chapter 3 Supplemental Figures:.....	76
Chapter 4 Appendix	83
Chapter 4 Supplemental Figures:.....	84
Chapter 5 Appendix	86

Chapter 5 Supplemental Figures.....	86
BIBLIOGRAPHY	89
CURRICULUM VITAE.....	101

LIST OF TABLES

Table 1 Demographic and clinical characteristics of study participants (N = 27). Values are presented as mean \pm standard deviation unless otherwise indicated. Fluid removed represents the average ultrafiltration volume per session. Crit-Line refers to subjects whose hematocrit was continuously monitored during dialysis via the Fresenius Crit-Line IV Monitor.....	25
Table S1 Demographic and treatment characteristics of subjects stratified by occurrence of intradialytic adverse events (N=18 with adverse events, N=9 without). Values are presented as mean \pm standard deviation unless otherwise indicated. Fluid removed represents the average ultrafiltration volume per session. Crit-Line data was available for a subset of participants (N=13 with adverse events, N=6 without) and refers to subjects whose hematocrit was continuously monitored during dialysis via the Fresenius Crit-Line IV Monitor.....	77
Table S2 Comparison of absolute changes (Δ) in optical and clinical parameters between subjects with (N=18) and without (N=9) intradialytic adverse events. Reported values reflect the mean \pm standard deviation of changes from baseline to end of dialysis treatment for optically measured biomarkers: oxyhemoglobin ([HbO ₂]), deoxyhemoglobin ([Hb]), total hemoglobin ([HbT]), tissue oxygen saturation (StO ₂), and water ratio. Clinical measurements including relative blood volume (BV) as measured by Crit-Line, and systolic blood pressure (SBP). A two-sided unpaired t-test was performed to assess statistical differences between groups. Of the parameters evaluated, Water Ratio (p = 0.044) and SBP (p = 0.039) were significantly different between groups, with adverse event subjects exhibiting a relative increase in water ratio and a more pronounced decline in systolic blood pressure.....	79

LIST OF FIGURES

Figure 1: The three vibrational modes of water and their associated frequencies (in wavenumber and wavelength respectively) Figure adapted from Stomp et al [53] ...	6
Figure 2: The absorption spectrum of pure water in the visible to SWIR wavelengths. Peaks in the absorption spectrum correspond to harmonics of the three modes. Peaks centered around 975nm and 1200nm being noted in this graph as combinations of asymmetric and symmetric stretch, and all three modes respectively. Figure from Stomp et al [53].....	7
Figure 3: Graph of the pure water absorption spectra from 600 to 1000nm at temperatures ranging from 15C to 65C. Note how around the 970 absorption peak and beyond there is a distinct increase in absorption as the thermal energy of the water increase. Data compiled from multiple sources [52,55,56,57].....	8
Figure 4 Spectra of absorption coefficients (μ_a) and the resulting reduced scattering coefficient (μ'_s) for four dominant chromophores (oxyhemoglobin HbO ₂ , deoxy hemoglobin Hb, water, and lipids) of human tissue in the NIR spectrum (~600 to 1000 nm). These plots are generated from values obtained from typical muscle tissue chromophore concentrations (Total Hemoglobin ([HbT]) = 117 μ M, Oxygen Saturation (StO ₂) = 65%, [Water] = 60%, [Lipid] = 20%) and scattering parameters (μ'_s (800 nm) = 1.3 mm ⁻¹ , b = 1) [22,23,24].....	13
Figure 5 A) Schematic diagram of the custom FD-Bb-SWIRS system. Key components include the following: ADC, analog-to-digital converter; APD, avalanche photodiode; DC, direct current; DDS, direct digital synthesizer; LPF, low-pass filter; Amp, amplifier; BPF, bandpass filter. Frequency-domain (FD) sources (730, 785, 930, and 940 nm) and FD detector are indicated by red lines, and continuous-wave (CW) source and detector are indicated by blue lines. B) Probe containing the FD and CW source and detector fibers with a source-detector separation (SDS) of 20 mm. C) FD-Bb-NIRS clinical system. The black enclosure houses the electronics controlled via a Windows 10 laptop.	15
Figure 6 Processing pipeline of the FD-Bb-NIRS system that combines FD-NIRS and broadband CW-NIRS systems. Note that λ_0 = 800 nm for the scattering power law fit.	17
Figure 7 Illustration of the experimental workflow for acquiring and processing optical measurements during hemodialysis using the FD-CW-NIRS clinical system. (Left): The probe was positioned over the main muscle body of the lateral gastrocnemius muscle. (Center): FD and CW measurements were acquired once per minute throughout the dialysis session. Top panels show representative time traces of FD absorption (μ_a) and scattering (μ'_s) at 730, 785, 830, and 940 nm. The bottom panel	

displays a representative calibrated CW reflectance spectra at wavelengths from 700-1000 nm recorded over time. (Right): Broadband absorption spectra (μ_a) from 700-1000 nm were reconstructed from the calibrated broadband reflectance spectra using MC-LUT enabling chromophore quantification. Chromophore concentrations were estimated using Beer's law. Created with assets from BioRender.com. 23

Figure 8 A) Absorption coefficient spectra (μ_a) and B) Reduced scattering coefficients (μ_s') at three time points (0, 100, and 200 minutes). Discrete frequency-domain (FD) wavelengths (730, 785, 830, 940 nm) are shown as data points, while continuous-wave (CW) data span the full 700–1000 nm range. C) Calibrated CW reflectance spectra over time and D) Broadband μ_a spectra, color-coded from blue (start of dialysis) to red (end), arrows show the dominant trend. E) Temporal display of the relative chromophore concentrations changes over hemodialysis: oxyhemoglobin ($[HbO_2]$), deoxyhemoglobin ($[Hb]$), total hemoglobin (HbT) and tissue oxygen saturation (StO_2). F) Change in tissue Water Ratio. 26

Figure 9 Time-normalized traces (mean \pm standard error) comparing chromophore extractions of subjects with adverse events (red, $N=16$) and without (blue, $N=9$) **A)** $\Delta [HbO_2]$ **B)** $\Delta [Hb]$ **C)** ΔStO_2 **D)** Δ Water Ratio. Two subjects with short-duration sessions ($t \leq 114$ min) were excluded. 29

Figure 10 Boxplots of subject values and group means for the absolute $\Delta [HbO_2]$, $\Delta [Hb]$, $\Delta [HbT]$, ΔStO_2 , and Δ Water Ratio from the beginning to end of dialysis. Adverse event subjects are shown in red ($N=18$), and non-adverse event subjects in blue ($N=9$). A significant difference was observed for Δ Water Ratio ($p < 0.05$). No other parameters reached statistical significance. 29

Figure 11 A&B) Longitudinal group-averaged scattering coefficients (A and b respectively) over normalized dialysis time for adverse events (red, $N=16$) and non-adverse (blue, $N=9$) subjects. Two subjects with short-duration sessions ($t \leq 114$ min) were excluded. C) Box plots of absolute values of scattering coefficients A and b at the end of dialysis for subjects with adverse events (red, $N=18$) and non-adverse (blue, $N=9$). A 2-sided t-test was used to assess whether group means differed significantly from zero ($p < 0.05$). Statistically significant changes were observed in scattering coefficient A..... 31

Figure 12 A) Confusion matrix from a top-performing 3-feature classification model (Δ Water Ratio, A, b). B) ROC curves showing classification performance of individual features and the combined model. While Δ Water Ratio, A, and b at 100% dialysis completion individually gave low AUC values of 0.6, 0.75 and 0.7 respectively, with the combined model achieved an AUC of 0.88. 33

Figure 13 A) Box plots of absolute change in relative blood volume (ΔBV) from start to end of dialysis, as measured by Crit-Line. Subjects with adverse events (red, $N=13$)

and without (blue, N = 6) presented similar means. No statistically significant difference was observed between groups. B) Box plots of the absolute change in systolic blood pressure (Δ SBP) from start to end of dialysis Subjects with adverse events (red, N = 18) and without (blue, N = 8). A 2-sided t-test ($p=0.039$) shows there is a statistically significant difference was observed between groups 35

Figure 14 Spectra of absorption coefficients (μ_a) and the resulting reduced scattering coefficient (μ'_s) for four dominant chromophores (oxyhemoglobin HbO_2 , deoxy hemoglobin Hb , water, and lipids) of human tissue. The total μ_a is calculated by adding the individual chromophore absorptions to get the human tissue absorption spectra. The region with white background indicates the NIR spectrum (~650 to 1000 nm) The shaded region indicates the SWIR spectrum (1000 nm and up). These plots are generated from values obtained from typical muscle tissue chromophore concentrations (Total Hemoglobin ([HbT]) = 117 μM , Oxygen Saturation (StO_2) = 65%, [Water] = 60%, [Lipid] = 20%) and scattering parameters ($\mu'_s(800 \text{ nm}) = 1.3 \text{ mm}^{-1}$, $b = 1$) [22,23,24,57,64,77,82,93,98,99]..... 43

Figure 15 Schematic diagram of the custom FD-Bb-SWIRS system. Key components include ADC = Analog-to-Digital Converter, APD = Avalanche Photo Diode, DC = Direct Current, DDS = Direct Digital Synthesizer, LPF = Low Pass Filter, Amp = Amplifier, BPF = Band Pass Filter. FD source and detector indicated by red lines, CW source and detector indicated by blue lines. 48

Figure 16 A) The adjustable probe containing the FD and CW source and detector fibers set to a source-detector separation (SDS) of 10mm B) The FD-Bb-SWIRS system. The black enclosure houses the electronic system which is controlled by a laptop. 48

Figure 17 Processing pipeline of the FD-Bb-SWIRS system that combines FD-NIRS and broadband CW-SWIRS systems. Note that $\lambda_0 = 900 \text{ nm}$ for the scattering power law fit 51

Figure 18 Example FD-Bb-SWIRS measurements of a liquid intralipid phantom composed of 1.5% lipid v/v calibrated against a 1% lipid volume/volume calibration liquid intralipid phantom. The FD-NIRS μ_a and μ'_s are overlaid with the respective CW-SWIRS spectra 51

Figure 19 Photos of the two porcine samples, muscle (M) sample and muscle with an adipose layer (M+A) sample. Photos were taken at baseline (before desiccation). . 55

Figure 20 Uncertainties in A) μ_a and B) μ'_s obtained from simulations with frequency-domain (FD) reflectance data. Optical property examples (shown as red crosses) are shown for human muscle tissue at 800 nm ($\mu_a = 0.02 \text{ mm}^{-1}$, $\mu'_s = 1 \text{ mm}^{-1}$) and 1200 nm ($\mu_a = 0.11 \text{ mm}^{-1}$, $\mu'_s = 0.6 \text{ mm}^{-1}$). These plots are generated from values obtained from typical muscle tissue chromophore concentrations (Total Hemoglobin

([HbT]) = 117 μM , Oxygen Saturation (StO_2) = 65%, [Water] = 60%, [Lipid] = 20%) and scattering parameters ($\mu'_s(500 \text{ nm}) = 1.5 \text{ mm}^{-1}$, $b = 0.9$) [22,23,24,57,64,77,82,93,98,99] 57

Figure 21 Spectra of A) μ_a and B) μ'_s of three solid mineral oil-based phantoms with carbon black concentrations at 0.05, 0.08, and 0.16 g/L. C) Values of μ_a D) values of μ'_s at 685, 852, 925, and 1210 nm vs different the carbon black concentrations in the phantoms. Lines in (C and D) indicate the linear fits across all data points. 58

Figure 22 Spectra of A) μ_a and B) μ'_s of the ten titration steps. The titration was preformed from 0% D_2O to 90% D_2O . C) Values of μ_a and D) values of μ'_s at 730, 852 (from FD measurements), 980, and 1200 nm (from broadband measurements) vs the different D_2O concentrations. Lines in (C and D) indicate the linear fits over all data points. 60

Figure 23 Optical properties and chromophore extraction results for two porcine tissues: a muscle (M) sample and a muscle with adipose layer (M+A) sample. Data were collected every hour over an 8-hour desiccation period. μ_a spectra A&B) and μ'_s spectra C&D) are presented for each desiccation hour, with values shown as means and standard errors based on three separate location measurements. Panels E&F) display the extracted water concentrations for both samples over time, with means and standard errors from measurements at three distinct locations 62

Figure 24 The raw spectrometer counts taken of a healthy volunteer's forearm compared to a dark calibration phantom at 15mm SDS. 71

Figure 25 Diagram showing the three-compartment fluid model during dialysis, Blue arrows indicate the movement of water as fluid is removed from the vascular space by ultrafiltration, with sequential refilling first from the interstitial and then from the intracellular compartments. Future work will focus on identifying optical signatures corresponding to these compartmental shifts in tissue fluid during vascular refill. (Modified from OpenStax CNX (OpenStax.org)) 73

Figure S1 Validation measurements of 11 phantoms taken by the the FD-Bb-NIRS system against a gold standard Network Analyzer (NA). This graph compares A) μ_a and B) μ'_s of both systems at their overlapping wavelength (730 nm). The dashed line represents the identity line. The FD-Bb-NIRS system preformed comparably to the NA system in this validation test. 75

Figure S2 Box plot of [Melanin] across subject's (N=27) self-reported race, stratified by self-identified race into three groups: Black (N=19), White (N=4), and Other (N=4). [Melanin] was derived from baseline measurements taken of pre-dialysis. These findings reflect expected physiological variability in epidermal melanin content across racial groups 76

Figure S3 Box plots represent the absolute relative change (Δ) in the measured chromophore derived parameters for each subject (N=27): oxyhemoglobin (HbO₂), deoxyhemoglobin (Hb), total hemoglobin (HbT), tissue oxygen saturation (StO₂), Water Ratio (RWater), and relative blood volume (BV) derived from crit line (N=19). A one-sample t-test was used to assess whether group means differed significantly from zero ($p < 0.05$). Statistically significant changes were observed in HbO₂, HbT, StO₂, and BV across the cohort..... 76

Figure S4 Box plots of the demographic and treatment characteristics are shown for subjects who experienced intradialytic adverse events (red, N=18) and those who did not (blue, N=9). Parameters include age, height, weight, fluid volume removed, and dialysis session duration. There is no statistically significant difference in the characteristics between the two groups..... 78

Figure S5 Longitudinal changes of A) Δ [Water] (%) and B) Δ [Lipid] (%), across subjects with (red, N=16) and without (blue, N=9) adverse events during dialysis. Solid lines represent mean absolute chromophore concentration change; shaded regions represent the standard error. Subjects who experienced adverse events demonstrated a relative increase in [Water] during dialysis, while those without adverse events showed progressive decreases in [Water]. Conversely, likely due to the partial volume effect, [Lipid] tended to decrease in the adverse group and increase slightly in the non-adverse group. 78

Figure S6 Longitudinal changes in relative blood volume change (Δ BV%) measured by Crit-Line over the course of dialysis for subjects with (N = 12, red) and without (N = 6, blue) intradialytic adverse events. Solid lines represent mean BV change; shaded regions represent the standard error. One subject was excluded from the analysis due to insufficient data points ($t \leq 114$ min) as described in Section 3.2. Δ BV% trends between groups were not statistically different. 79

Figure S7 The AUC from the top-performing 3-feature classification models (Δ Water Ratio, A, b) and the combined features over the normalized time course of dialysis completion..... 80

Figure S8 Time-normalized traces (mean \pm standard error) comparing chromophore extractions of subjects with adverse events (red, N = 16) and without (blue, N = 9) of the Δ Water Ratio (Two subjects with short-duration sessions ($t \leq 114$ min) were excluded from the normalized time trace). The black dots overlay indicate the timestamp of adverse events occurring. The average adverse event occurred at 51.72% \pm 24.84 % of dialysis completion 81

Figure S9 Time-normalized traces (mean \pm standard error) comparing chromophore extractions of subjects with Hypotensive events (red, N = 14) and without (blue,

N = 11) A) Δ [HbO₂] B) Δ [Hb] C) Δ StO₂ D) Δ Water Ratio. Two subjects with short-duration sessions ($t \leq 114$ min) were excluded. 81

Figure S10 Boxplots of subject values and group means for the absolute Δ [HbO₂], Δ [Hb], Δ [HbT], Δ StO₂, and Δ Water Ratio from the beginning to end of dialysis. Hypotensive subjects are shown in red (N = 16), and non-Hypotensive subjects in blue (N = 11). A significant difference was observed for Δ Water Ratio ($p < 0.05$). No other parameters reached statistical significance. 82

Figure S11 Examples of extracted absorption (μ_a , panel A) and reduced scattering (μ'_s , panel B) distributions, showing for two sets of optical properties representing values for human muscle tissue at 800 nm ($\mu_a = 0.02 \text{ mm}^{-1}$, $\mu'_s = 1 \text{ mm}^{-1}$, shown in blue) and 1200 nm ($\mu_a = 0.11 \text{ mm}^{-1}$, $\mu'_s = 0.6 \text{ mm}^{-1}$, shown in red). Ground truth values are indicated by solid lines, while the distribution mean values are shown in dashed lines. Panels C and D display the absolute differences between the ground truth values and the distribution means across different μ_a and μ'_s values. 84

Figure S12 Example raw spectra at A) Baseline and B) Hour 8 for both M and M+A porcine samples as well as dark phantoms at similar integration times. All porcine sample spectrometer counts were several hundred counts above the dark phantom to ensure good SNR. 85

Figure S13 Effect of gelatin concentration on water absorption peak positions. (Left) Peak wavelength near the 980 nm water peak. (Right) Peak wavelength near the 1200 nm water peak. Both peaks experienced red shifts with increasing gelatin concentration, with the 1200 nm peak experiencing a $\sim 3X$ greater shift than 980 nm. Error bars represent standard deviation across phantoms. 86

Figure S14 Collagen absorption spectrum from 900–1250 nm. Data is from Sekar et al 2017 [116]. Note the peak near ~ 1190 to 1200 nm and elevated absorption around 980 to 1000 nm these features greatly overlap with the water absorption peak features at 980 and 1200 nm. (See Figure 14 in chapter 4.1) 87

Figure S15 (Left) The average calibrated CW spectra of gelatin phantoms at varying collagen concentrations (0–24 g). (Right) The corresponding local minima at ~ 980 nm and ~ 1200 nm. 88

LIST OF ABBREVIATIONS

A.....	Scattering amplitude
ADC.....	Analog to Digital Converter
Amp.....	Amplifier
ANSI	American National Standards Institute
APD	Avalanche photodiode
AUC	Area Under the Curve
b.....	Scattering slope
Bb.....	Broadband
BMC.....	Boston Medical Center
BP.....	Blood Pressure
BPF	Bandpass Filter
BV.....	Blood Volume
CHS.....	Coherent Hemodynamics Spectroscopy
CKD	Chronic Kidney Disease
CW	Continuous Wave
D ₂ O.....	Deuterium Oxide
DC.....	Direct Current
DDS	Direct Digital Synthesizer
DI	Deionized Water
DOS	Diffuse Optical Spectroscopy
ESKD	End Stage Kidney Disease

FD	Frequency Domain
FD-Bb-NIRS	Frequency-Domain Broadband Near-Infrared Spectroscopy
FD-Bb-SWIRS	Frequency-Domain Broadband Shortwave Near-Infrared Spectroscopy
FD-DOS	Frequency-Domain Diffuse Optical Spectroscopy
FD-NIRS	Frequency-Domain Near-Infrared Spectroscopy
FD-SWIRS	Frequency-Domain Shortwave Near-Infrared Spectroscopy
FWHM	Full Width half max
GUI	Graphic User Interface
GPUs	Graphical Processing Units
Hb	Deoxyhemoglobin
HbO ₂	Oxyhemoglobin
HbT	Total Hemoglobin
HD	Hemodialysis
IDH	Intradialytic Hypotension
IRB	Institutional Review Board
IVUS	Intravascular Ultrasound
LDPE	low-density polyethylene
LPF	Low Pass Filter
LUTs	Look-up Tables
MAP	Mean Arterial Pressure
MC	Monte Carlo
MC-LUT	Monte Carlo Look-up Table

MCX	Monte Carlo eXtreme
NA.....	Numeric Aperture
NIR.....	Near Infrared
NIRS	Near Infrared Spectroscopy
NKF KDOQI.....	National Kidney Foundation's Kidney Disease Outcomes Quality Initiative
ROC	Receiver Operating Characteristic
RWater	Water Ratio
SBP	Systolic Blood Pressure
SDS	Source Detector Separation
SEBS	polystyrene-block-poly(ethylene-ran-butylene)
SFDI.....	Spatial Frequency Domain
StO ₂	Oxygen Saturation
SWIR.....	Short Wave Infrared
SWIRS	Shortwave Infrared Spectroscopy
TARA.....	Transient Artifact Reduction Algorithm
TD	Time-Domain
TD-NIRS.....	Time-Domain Near-Infrared Spectroscopy
μ_a	Absorption
μ_s'	Reduced Scattering

CHAPTER 1: Introduction

Note: Section 1.1.1 of this chapter was part of a complete manuscript submitted for peer review to the journal SPIE Biophotonics Discovery.

Suciuc D^a, Pham T^a, Wei LL^a, Hokestra I^{ab}, Yadati P^{ab}, Chitalia V^{abc}, Roblyer D^{ad}.
“Frequency Domain Near Infrared Spectroscopy for Fluid Volume Status Monitoring during Hemodialysis”.

^aBoston University, Department of Biomedical Engineering, Boston, MA, USA

^bRenal Section, Department of Medicine, Boston Medical Center and Boston University Medical School, Boston, MA

^cBoston Veterans Affairs Healthcare System, Boston, MA

^dBoston University, Department of Electrical and Computer Engineering, Boston, MA, USA

1.1 Background

1.1.1 End Stage Kidney Disease Treatment and Current Limitations

Chronic kidney disease (CKD) affects approximately one in seven adults in the United States, representing an estimated 30 million individuals [1]. Of these, over 700,000 are classified as end-stage kidney disease (ESKD) patients [1,2]. In ESKD, renal function becomes insufficient to sustain life without intervention [1,2]. Kidney transplantation remains the optimal long-term treatment for ESKD; however, due to organ shortages and transplant waitlists exceeding five years, ESKD patients rely on dialysis as their primary lifeline [1,2]. Hemodialysis, the most common renal replacement therapy, removes excess

solutes, toxins, and water (also called volume) from the bloodstream. In 2017 and 2018, 70% of the over 700,000 Americans with CKD were on hemodialysis [1,3]. Patients with ESKD accumulate fluid in between hemodialysis sessions, whose removal is a quintessential function of hemodialysis. Achieving a clinically optimal fluid balance during hemodialysis remains one of the most challenging aspects of clinical ESKD management. The median survival for patients undergoing maintenance hemodialysis is approximately 5 to 7 years, with a five-year survival rate of approximately 50% [5,4]. A major contributor to mortality in patients with CKD is cardiovascular complications driven by inadequate volume management during hemodialysis [6,7]. Even mild fluid overload is an independent risk factor for all-cause and cardiovascular mortality in CKD patients. Excess fluid removal results in hypotension, muscle cramps. These clinical complications result in a premature termination of the hemodialysis session in close to 20% patients, compromising patient long term vitality [8]. Nearly half of all hemodialysis patient deaths and a quarter of all hospitalizations are associated with cardiovascular disease [7,9]. With an estimated 20-50% of all ESKD patients undergoing inaccurate fluid removal during treatment [10], there is a critical need for improved, long-term sustainable support strategies for this patient population.

A fundamental challenge in hemodialysis care is the accurate assessment of a patient's "dry weight," or the weight at which a patient is euvolemic, meaning they have neither too much nor too little volume [11,12]. In current standard-of- care technique for volume assessment or mongering when a patient achieves "dry weight" is often based on subjective symptoms such as cramping, dizziness, or nausea, and clinical signs such as

edema and inter-dialysis weight changes, which can occur when fluid is removed too quickly or in too high a quantity during treatment [11]. This approach is imprecise and is subject to change based on current status of the patient's health, prior studies have shown that poor volume assessment results in erroneous ultrafiltration, causing up to 50% to develop dialysis-related hypotension, and experience a poor quality of life after treatment [13-15]. Despite the recognized importance of accurate volume assessment, current methods remain subjective, crude, and generally unreliable in routine clinical practice [12,16-18]. Volume assessment during hemodialysis is a research priority by the Kidney Health Initiative, given that there are currently no quantitative standards for monitoring the volume status of patients undergoing treatment [19,20]. This unmet clinical need has driven interest in noninvasive optical techniques, such as diffuse optical spectroscopy (DOS), which could provide quantitative information about changes in tissue composition and fluid status.

1.1.2 Overview of Diffuse Optical Spectroscopy

Diffuse optical spectroscopy (DOS) technologies are a class of optical techniques for non-invasively quantifying biologic tissue [21]. These methodologies can use light to probe tissue and quantify absorption (μ_a) and reduced scattering (μ_s') properties and acquire chromophore extractions. The four dominant chromophores in human tissue in the near-infrared (NIR) and short-wave infrared (SWIR) spectral regions are oxyhemoglobin, deoxyhemoglobin, water, and lipid [22-26].

Four main DOS modalities are used in biological measurements: continuous-wave (CW), temporal frequency-domain (FD), spatial frequency domain (SFDI), and time-domain (TD) [21,27-]. Of these, only temporal (FD-NIRS and TD-NIRS) and spatial (SFDI) modalities allow for the independent quantification of absolute tissue absorption (μ_a) and scattering (μ_s') properties, with FD-NIRS accomplishing this by measuring the amplitude and phase shift of intensity-modulated light after it travels through tissue [21,31,32]. While CW-NIRS systems are simpler, more compact, and capable of covering a broad spectral range, they cannot independently resolve scattering and absorption. Therefore, CW systems are typically limited to monitoring relative trends in absorption or chromophore concentration [28,33-35].

To overcome the trade-off between quantitative accuracy and broad spectral range, hybrid FD+CW systems have been developed enabling the recovery of absolute broadband μ_a and μ_s' spectra [36,37]. Prior hybrid FD+CW NIRS techniques, namely FD-Bb-NIRS, have largely focused on quantifying concentrations of oxygenated and deoxygenated hemoglobin [27,38-43], but there has been a growing interest in using diffuse optical techniques to measure tissue concentrations of water and lipids [44-47].

Quantification of these chromophore species is commonly reached by extracting the absorption and reduced scattering (μ_a and μ_s') optical properties of the tissue [21]. Beer's Law (Equation 1) is used to calculate the absolute concentrations of the chromophore species. Reduced scattering coefficients can be fit to a power law. Beer's Law displays the relationship between the attenuation of light through a material and the

properties of that material. Where A is the absorbance, ε is the molar absorption coefficient, c is the concentration of the material, and l is the optical path length.

$$A = \varepsilon cl \quad (1)$$

The power law (Equation 2) is the empirical description of the wavelength dependence of scattering in tissue; to yield the scattering amplitude (a) and scattering power (b). where λ is the desired wavelength of μ'_s , λ_0 is the reference wavelength, a is the scattering amplitude at λ , b is the scattering power, which is always a positive value.

$$\mu'_s = a\left(\frac{\lambda}{\lambda_0}\right)^{-b} \quad (2)$$

Having established the theoretical framework and instrumentation of diffuse optical spectroscopy, the next consideration is the physics of water absorption in the NIR and SWIR, which provides the basis for its quantification in tissue using these methods.

1.1.3 Physics of Water in NIR and SWIR Wavelengths

There are few prior studies of noninvasive measurements monitoring water volume changes in ESKD patients undergoing hemodialysis [48-51]. None to our knowledge have used DOS techniques to acquire continuous fluid dynamic changes. The intention of the FD+CW hybrid devices design was to take measurements in the NIR and SWIR wavelength ranges, due to their sensitivity changes in water absorption, this section will review the fundamental optical characteristics of water in the NIR (600-1000 nm) and SWIR (900-1310 nm) wavelength ranges.

Pure water has a distinct and highly sensitive optical absorption spectra due mainly to its three vibrational modes. Water molecules are never at rest, they rotate, twist, and vibrate. The vibrational modes of water occur in three forms, and are classified as: symmetric stretch, asymmetric stretch, and bending. The vibrational modes relate to how the two hydrogen molecules in water move in relation to the oxygen molecule [23,52,53]. A water molecule resides in a singular vibrational mode which is independent of the surrounding water molecule's modes.

Each vibrational mode has a distinct fundamental frequency, related to the rate at which that molecule's hydrogen atoms oscillate around the oxygen atom. The exact frequency depends on the state and temperature of water but at 25C in a pure water system, symmetric stretching (v_1) has a frequency of 3280 cm^{-1} , asymmetric stretching (v_3) is 3490 cm^{-1} and bending (v_2) is 1654 cm^{-1} . (Figure 1) [53]. The frequency of the vibrational mode is important when considering the absorbance spectrum of water.

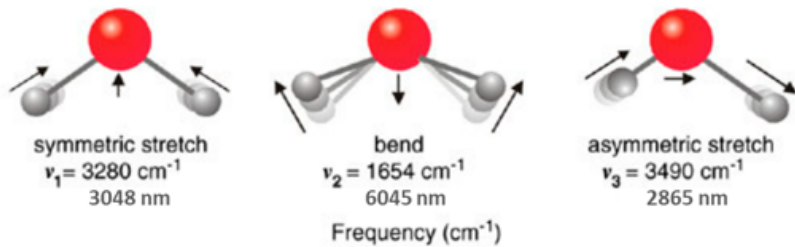


Figure 1: The three vibrational modes of water and their associated frequencies (in wavenumber and wavelength respectively). Figure adapted from Stomp et al [53].

By converting the fundamental frequencies of the vibrational modes into wavelength, the harmonic pattern occurring within the pure water spectra can be observed. Symmetric and asymmetric stretch have very similar energy requirements, and thus their

absorption peaks converge into one large peak around 3000 nm [53]. Bending has lower energy requirements, thus has an absorption peak at a higher wavelength, around 6000 nm. The harmonics of these vibrations occur at shorter wavelengths (higher energy levels), at double to even triple the required energy. Thus, the harmonics of bending and stretching vibrational modes can be recognized in visible and NIR ranges of the water absorption spectrum [54]. Water has low absorbance in the visible spectra, with increasing absorbance in the far NIR to SWIR wavelength ranges, where water becomes the main absorber of the four main biologic chromophores. There are multiple known water absorbance peaks, notably the 975 nm and 1200 nm absorbance peaks (for liquid water at 25C). The distinct absorption peak at around 975 nm has been identified as the third harmonic of symmetric and asymmetric stretch vibration, and the 1200 nm absorbance peak is also associated with the third harmonic of bending (Figure 2) [53].

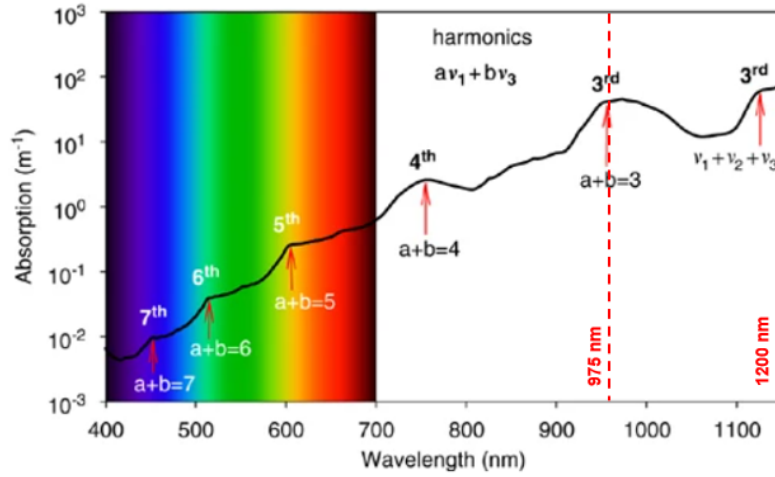


Figure 2: The absorption spectrum of pure water in the visible to SWIR wavelengths. Peaks in the absorption spectrum correspond to harmonics of the three modes. Peaks centered around 975 nm and 1200 nm being noted in this graph as combinations of asymmetric and symmetric stretch, and all three modes respectively. Figure from Stomp et al [53].

As stated above, the exact fundamental frequencies, and therefore the exact absorption peak of any given harmonic of water will depend on the state of the system being measured. A simple example of changing harmonic properties affecting the water spectra can be seen with temperature change. As temperature increases the energy of the system goes up, causing water molecules to vibrate faster, which can be observed in the water absorbance spectra, particularly at the harmonic peaks (Figure 3) [55]. The vibrational modes of water are impacted by much more complex interactions than simply increasing the energy within the system. Changes in vibrational mode are largely affected by water's hydrogen bonds.

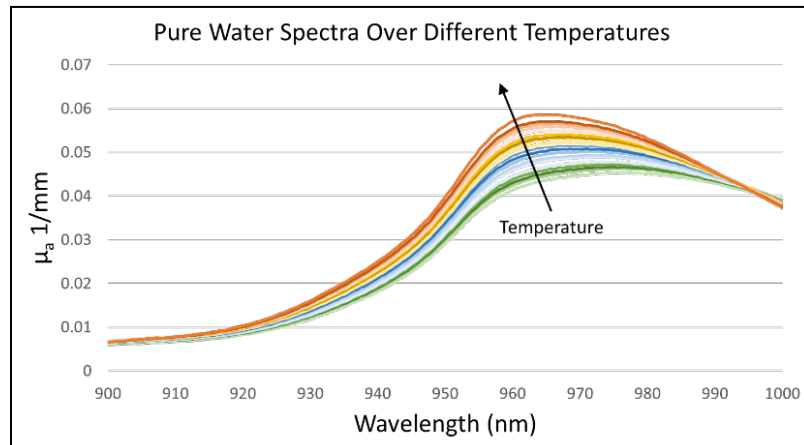


Figure 3: Graph of the pure water absorption spectra from 600 to 1000 nm at temperatures ranging from 15C to 65C. Note how around the ~970 nm absorption peak and beyond there is a distinct increase in absorption as the thermal energy of the water increases. Data compiled from multiple sources [52,55,56,57].

In water, the two hydrogen atoms are covalently bonded to the core oxygen atom. Water molecules interact with all other molecules via hydrogen bonds, which are significantly weaker than covalent bonds. These weak hydrogen bonds have a significant

effect on the vibrations of a water molecule. Lower frequency components are attributed to water molecules with stronger hydrogen bonds (stretch) and higher frequency components have weaker hydrogen bonds (bending) [58]. As observed in the temperature example stated above, changing temperature causes hydrogen bond strength to change, causing changes in vibration, resulting in a change in harmonics, thus changing the absorbance spectra. As the system changes the vibration of the water molecules will change at different rates depending on hydrogen bond strength, meaning the harmonics will change dissimilarly [53,58].

Hydrogen bonds further affect the optical properties of water when considering changes to the system such as within biologic tissues. In tissue water makes hydrogen bonds with non-water molecules, such as protein molecules [59]. Proteins are highly charged, and thousands to hundreds of thousands of times bigger than a single water molecule, meaning that many water molecules can bind to a single protein molecule. When water binds to the protein, the vibration of the water molecule changes. In patients with ESKD as free water is removed by hemodialysis and what remains is intracellular or intramuscular water, the average vibrational frequency of the system will go down, resulting in increased absorption of the system. Additionally, it is anticipated that the absorption peaks will widen as free water is removed, it will take on the optical profile more similar to anticipated healthy tissue [59].

1.2 Thesis Chapter Structure

This thesis is organized into four main chapters. Chapter 2 focuses on the development and characterization of a Frequency-Domain Broadband Near-Infrared Spectroscopy (FD-

Bb-NIRS) system, describing the instrumentation, design, and data processing pipeline methodologies. Chapter 3 presents a clinical study in which the FD-Bb-NIRS system was used to monitor tissue chromophore changes in patients undergoing hemodialysis. Chapter 4 extends the scope of FD+CW based optical technologies into the shortwave infrared region (FD-Bb-SWIRS). This chapter describes the design, development, and validation of the next-generation system. Finally, Chapter 5 provides a discussion of findings, limitations, and future directions for wearable and clinically translatable FD+CW optical systems.

1.3 Specific Aims

The Specific Aims of this dissertation are as follows:

Aim 1: Creation of the FD-Bb-NIRS System

Develop, optimize, and validate a high-speed FD-Bb-NIRS platform for quantitative, broadband tissue measurements.

Aim 2: FD-Bb-NIRS Clinical Study

Using the FD-Bb-NIRS system to take continuous FD+CW measurements of hemodialysis patients. Perform data analysis to determine the FD-Bb-NIRS system's ability to monitor tissue chromophores and detect early signs of adverse events.

Aim 3: Development and Validation of the FD-Bb-SWIRS System

Design, test and validate a FD-Bb-SWIRS system to expand the accessible spectral range and improve sensitivity to tissue water chromophore extractions. Validation was performed using mineral oil-based solid phantoms, deuterium oxide (D_2O) liquid phantoms, and desiccating porcine tissue.

Chapter 2: Aim 1: Creation of FD-NIRS System

Note: Sections 2.1-2.3 of this chapter were part complete manuscript submitted for peer review to the journal SPIE Biophotonics Discovery:

Suciú D, Pham T, Wei LL, Hokestra I, Yadati P, Chitalia V, Roblyer D. “Frequency Domain Near Infrared Spectroscopy for Fluid Volume Status Monitoring during Hemodialysis”.

2.1 Background/Motivation

Near-infrared spectroscopy (NIRS) offers a potential solution to the unmet clinical need of noninvasive, objective fluid volume monitoring during hemodialysis. NIRS uses light propagation in highly scattering media to measure tissue optical properties in the near-infrared (NIR, 650 to 1000 nm) wavelength range. NIRS has been widely applied across biomedical fields, including oncology, neuroscience, and clinical diagnostic care [21]. The four main NIRS methods were described in Chapter 1.1.2. In summary, FD, TD, and SFDI enable independent quantification of absorption (μ_a) and scattering (μ_s'), while CW systems are simpler and broadband but limited to relative absorption trends. To address this trade-

off, hybrid FD+CW systems (FD-Bb-NIRS) have been developed to recover absolute broadband spectra of chromophores.

A custom-built frequency-domain broadband near-infrared spectroscopy (FD-Bb-NIRS) system was created for the application of real-time monitoring of tissue physiology during hemodialysis in a clinical study (clinical study findings in Chapter 3). Previous works have monitored changes in oxygen saturation and cerebral tissue oxygenation in hemodialysis patients using frequency-domain near-infrared spectroscopy (FD-NIRS) and focused on extracting oxygenated and deoxygenated hemoglobin concentrations due to the limited wavelength selection [49-51]. Utilizing a broadband wavelength range through the FD-Bb-NIRS systems allows for more accurate assessment of absolute hemoglobin concentrations together with water and lipid content. To our knowledge, no previous studies have utilized a combined FD+CW NIRS system for continuous monitoring of tissue optical properties during hemodialysis, nor have they evaluated such measurements in the context of categorizing adverse clinical outcomes. The FD-Bb-NIRS system enables quantitative assessment of absolute chromophore concentrations ($[\text{HbO}_2]$, $[\text{Hb}]$, $[\text{Water}]$, $[\text{Lipid}]$) and optical scattering properties (A , b) over the course of hemodialysis, with the goal of detecting physiological patterns associated with intradialytic adverse events. Our findings demonstrate that tissue-level changes in relative tissue water fraction and absolute scattering parameters exhibit statistically significant associations with hemodynamic instability, outperforming the clinically available tool (Crit-Line) in identifying dialysis sessions in which adverse events occurred. These results suggest the potential for noninvasive optical techniques to enhance fluid status assessment and improve patient

safety in reducing adverse events and augmenting treatment efficacy through adequate volume removal in the hemodialysis patient population.

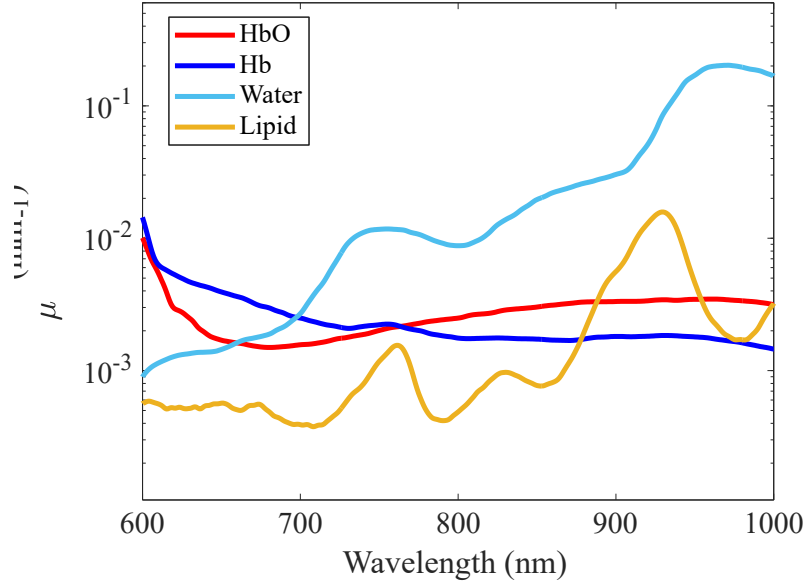


Figure 4 Spectra of absorption coefficients (μ_a) and the resulting reduced scattering coefficient (μ'_s) for four dominant chromophores (oxyhemoglobin HbO₂, deoxy hemoglobin Hb, water, and lipids) of human tissue in the NIR spectrum (~600 to 1000 nm). These plots are generated from values obtained from typical muscle tissue chromophore concentrations (Total Hemoglobin ([HbT]) = 117 μM , Oxygen Saturation (StO₂) = 65%, [Water] = 60%, [Lipid] = 20%) and scattering parameters ($\mu'_s(800 \text{ nm}) = 1.3 \text{ mm}^{-1}$, $b = 1$) [22,23,24].

2.2 FD-Bb-NIRS Instrumentation

The FD-Bb-NIRS system combined FD and broadband NIRS components (Figure 5A). Details of the custom digital FD-NIRS component have been previously described [60]. The FD component of the system used illumination wavelengths of 730, 785, 830, and 940 nm (LP730-SF15, LP785-SF20, LP830-SF30, LP940-SF30, Thorlabs, Newton, NJ). The FD laser illumination power ranged from 9.5mW to 14mW per laser depending on the wavelength, such that the system's combined FD lasers power output was within the American National Standards Institute (ANSI) safety standard. Direct digital

synthesizer (DDS) boards were used to simultaneously modulate each laser diode at the selected discrete frequencies between 119 and 134 MHz. A broad-spectrum tungsten halogen lamp (HL-2000-HP-B, Ocean Optics, wavelength range from 360-2400 nm) was used as the illumination source for the CW measurements.

Custom optical fibers were made by Fiberoptic Systems Inc. (Simi Valley, CA) for both FD and CW measurements. All fibers terminated at a right angle so they could lay flat against the subject's skin. Two source and detector fibers were used to increase optical power to allow for a 20 mm source detector separation (SDS), allowing for sensitivity to tissue depths of at least several mm [45,61]. A custom fiber holder was 3D printed to hold the fibers for clinical measurements as seen in (Figure 5B). The source FD fibers were 400 μm diameter fibers with a numeric aperture (NA) of 0.55 to deliver light to the tissue. A 2.3 mm fiber (NA: 0.55) was used for FD detection, and a 1 mm fiber (NA: 0.55) was used for CW source and detection.

For FD-NIRS detection, a 3-mm-diameter silicon avalanche photodiode (APD) (S11519, Hamamatsu) was used to detect laser light. A 250 mega-sample per second analog-to-digital converter (ADC) was used to digitize the APD signal. The Goertzel algorithm was implemented in the system's microprocessor to calculate the phase and amplitude of the FD reflectance measurements at each wavelength. The CW-NIRS emitted broadband light was detected using a 2048-pixel CCD spectrometer (AvaSpec-HS2048XL, Avantes). The grating and slit width were selected to achieve a usable measurement range of 700-1000 nm with a spectral resolution of 7.5 nm full width at half maximum (FWHM). A calibration procedure was used to remove the instrument response function of clinical

system as previously described using the solid silicone phantom for calibration [62]. The clinical system was controlled by a custom interface written in MATLAB (MathWorks Inc., Natick, MA) and operated on a Windows 10 laptop. The FD and CW data were collected sequentially as described in [62], at a final sampling rate of 110 to 1200 ms per measurement (subject dependent). The assembled system could fit on a portable cart that was brought bedside during clinical measurements (Figure 5C).

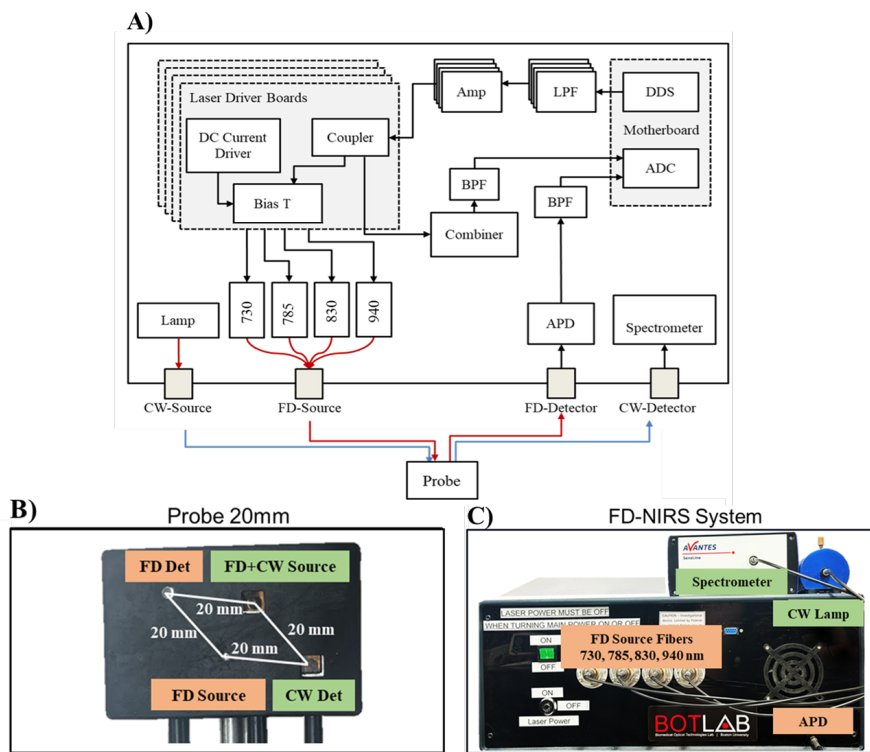


Figure 5 A) Schematic diagram of the custom FD-Bb-SWIRS system. Key components include the following: ADC, analog-to-digital converter; APD, avalanche photodiode; DC, direct current; DDS, direct digital synthesizer; LPF, low-pass filter; Amp, amplifier; BPF, bandpass filter. Frequency-domain (FD) sources (730, 785, 930, and 940 nm) and FD detector are indicated by red lines, and continuous-wave (CW) source and detector are indicated by blue lines. **B)** Probe containing the FD and CW source and detector fibers with a source-detector separation (SDS) of 20 mm. **C)** FD-Bb-NIRS clinical system. The black enclosure houses the electronics controlled via a Windows 10 laptop.

2.3 Data Processing for FD-Bb-NIRS

For data processing, a previous developed MC-LUT approach [61-63] was used for a homogeneous medium with semi-infinite geometry in order to integrate FD and CW NIRS to recover tissue broadband absorption coefficient (μ_a) and reduced scattering coefficient (μ_s') over the 700–1000 nm spectral range. An overview of the data processing pipeline for the FD-Bb-NIRS system can be seen in Figure 6. The construction of MC-LUT was described in detail in previous works [60,61]. A brief summary of MC-LUTs can be found in Chapter 2.4. Look-up tables (LUTs) at different modulation frequencies (for FD data) and at 0 MHz (CW MC-LUT for CW data) were generated for the ranges of μ_a from 0 mm^{-1} to 0.3 mm^{-1} and μ_s' from 0 mm^{-1} to 2 mm^{-1} . For measurements on solid calibration phantoms and tissue, the refraction index and scattering anisotropy were assumed to be $n = 1.4$ and $g = 0.9$ [64].

FD μ_a and μ_s' values of the 730, 785, 830, and 940 nm lasers were extracted from the calibrated amplitude and phase values using the MC-LUT inverse model. Calibration was conducted on solid silicone phantoms with known optical properties. The power law was fit to the FD μ_s' using the wavelength dependence of scattering [64]. The broadband μ_a spectra ranging from 700 to 1000 nm were obtained from the calibrated CW-NIRS measurements and known μ_s' spectra. This was achieved by first calibrating the CW measurements using a Spectralon standard (Labsphere, North Sutton, NH) to correct for features of the broad-spectrum halogen lamp source. The broadband CW reflectance was then scaled to match with the expected values at the overlapping FD wavelengths, which were computed from the first step using the CW MC-LUT forward model. Thus, the

broadband μ_a spectra was computed by then applying the CW MC-LUT inverse model to the calibrated CW reflectance data and the known μ_s' at 700-1000 nm.

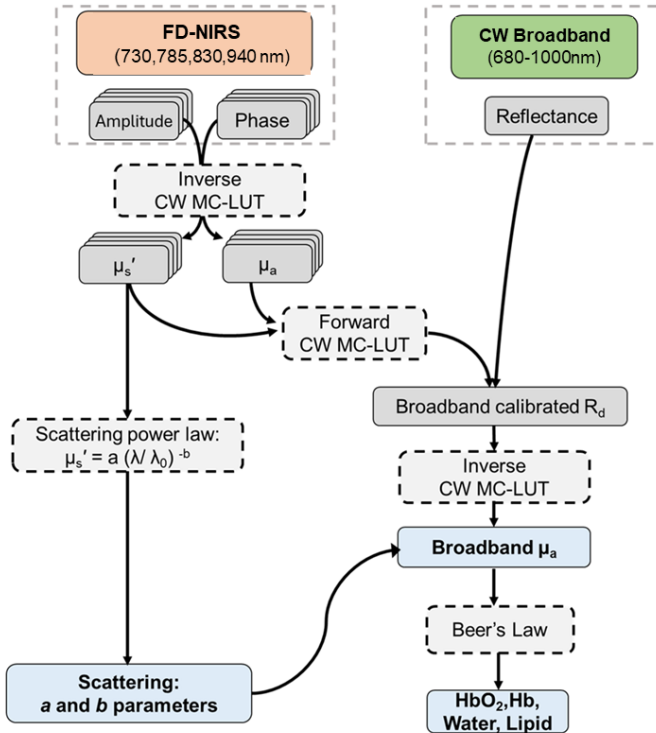


Figure 6 Processing pipeline of the FD-Bb-NIRS system that combines FD-NIRS and broadband CW-NIRS systems. Note that $\lambda_0 = 800$ nm for the scattering power law fit. The calibrated CW reflectance data and known FD μ 's values are used with CW MC-LUT inverse model to compute μ_a spectrum.

2.4 Monte Carlo Modeling Simulations

In order to extract absorption (μ_a) and reduced scattering (μ_s') contrasts from FD-Bb-NIRS measurements, accurate models are required to relate detected FD amplitude and phase to underlying tissue optical properties. This is achieved through look-up tables (LUTs) derived via Monte Carlo (MC) Modeling. MC Modeling is a flexible technique used to predict the probability of an outcome when random variables are present. This allows for the simulation of light propagating in tissue. This is done by repeated simulations

of random walks and statistical analyses to simulate photons interacting and traveling through tissue [65,66].

To create a typical MC simulation three components are required. 1) A statistical model describing photon and tissue/phantom interactions, 2) defined inputs parameters and their probability distributions, and 3) a generated set of random variables from the distribution to simulate photon step sizes and scattering angles [65,67]. Repeated simulations of millions of photon trajectories produced reflectance and transmittance distributions, which were subsequently compiled into LUTs spanning physiologically relevant μ_a and μ_s' ranges. These LUTs served as the foundation for inverse models that enabled reliable recovery of tissue optical properties from experimental data.

Historically, the computational burden of running sufficiently large MC simulations limited their accessibility, as accurate predictions required extensive photon statistics and high-performance computing resources [67]. Recent advances in computing hardware, particularly graphical processing units (GPUs), have significantly reduced these barriers. Monte Carlo eXtreme (MCX) is an open-source optical imaging package, and is one of the fastest, most accurate and most versatile Monte Carlo particle simulators freely available to users [67]. Our previous work with MC-based simulations in diffuse optical technologies provided the foundation for the inverse modeling approaches used in this dissertation [61,63]. Validation of the FD-Bb-NIRS system was performed against a gold-standard Network Analyzer (NA). Experimental protocol and results are described in Chapter 2 Appendix and Figure S1.

Chapter 3: Aim 2: Clinical Study

Note: This chapter was part of a complete manuscript submitted for peer review to the journal of SPIE Biophotonics Discovery:

Suciuc D, Pham T, Wei LL, Hokestra I, Yadati P, Chitalia V, Roblyer D. “Frequency Domain Near Infrared Spectroscopy for Fluid Volume Status Monitoring during Hemodialysis”.

3.1 Introduction of Existing ESKD Clinical Fluid Management

Currently utilized clinical monitoring methods, such as optical hematocrit tracking, bioimpedance, and intravascular ultrasound assessment of inferior vena cava diameter, each have their own limitations related to cost, invasiveness, technical complexity, and limited sensitivity to early physiological changes. Direct hematocrit monitoring methods, which involve blood draws, are labor-intensive and susceptible to operator variability [68,69]. Indirect hematocrit monitoring, with the most common technology being Crit-Line (Fresenius Medical Care, Bad Homburg, Germany), optically monitors *ex vivo* blood being directed to the dialysis device, and is often inadequate for fluid assessment, measuring relative blood volume changes, however it provides inconsistent results or is improperly used when assessing patients risk during dialysis [68-72]. Bioimpedance, which utilizes small electrical current to probe core and limb impedance, is influenced by electrolyte shifts and temperature [69,70,73]. Intravascular ultrasound (IVUS), in which an intravenous ultrasound measures the diameter of the inferior vena cava to assess intravascular water volume changes in response to dialysis. This method requires catheterization, which is invasive and often unavailable in routine clinical settings

[1,16,17,18,48,68,69]. Current approaches to volume assessment during dialysis remain largely out of reach and inaccurate in current clinical settings. For patients with ESKD, accurate monitoring of fluid status during dialysis may improve long-term outcomes by reducing cardiovascular and pulmonary complications associated with fluid overload, thereby lowering the risk of adverse events and hospitalizations. Furthermore, precise fluid volume assessment could assist clinicians in determining a patient's proximity to their 'dry weight', ultimately improving quality of life while awaiting kidney transplantation. There is a present need for clinically accessible, objective, and accurate methods for fluid monitoring to improve patient care and reduce the risk of adverse outcomes.

3.2 Methods

3.2.1 Clinical Exponential Procedure

A clinical study was conducted to assess the ability of the FD-Bb-CW NIRS system in monitoring tissue changes during hemodialysis, and to identify potential physiological markers associated with intradialytic adverse events. Participants for this study were recruited from the inpatient hemodialysis care center patient population at Boston Medical Center from July 2023 to November 2024. All measurements were conducted under an institutionally approved protocol (BU BMC IRB H-41696). The inclusion criteria encompassed individuals above the age of 18 of any race, gender, or ethnicities with ESKD who were prescribed fluid removal during their inpatient hemodialysis treatment. The exclusion criteria included anyone with below knee amputations, had restless leg syndrome, or medical anxiety that included symptoms of restlessness. Additionally,

subjects who only had blood cleaning with no fluid volume removed were excluded from the study. All participants consented to the study in person. In total, 27 participants consented to the study (Table 1 shows further participant demographic information. Every session was taken as an independent study. 0 patients underwent more than one study).

The measurement setup is shown in Figure 7. For each subject, their lateral gastrocnemius muscle was palpated to identify the main head of the muscle body. The probe containing the source and detector fibers was placed on the skin above the muscle body, oriented longitudinally to the muscle fibers, and secured using Tegaderm tape. This location was chosen based on previous works by Colucci et al, where it was observed with MRI imaging of the lower extremities that the lateral gastrocnemius corresponds to overall fluid status during hemodialysis [48]. Subjects were reclined in a hospital bed throughout the duration of dialysis. FD and CW measurements were taken sequentially once a minute over the entire duration of dialysis. During this time intradialytic adverse events, clinical interventions, visible movements or postural changes were timestamped and logged for post processing data discrimination and motion correction. Additionally, blood pressure (BP), heart rate, and ultrafiltration rate were recorded every 15 minutes.

Intradialytic adverse events were defined as follows: vomiting, cramping, dizziness, headache, shortness of breath, sweating, stroke, fluid return, or intradialytic hypotension (IDH). IDH is defined by the National Kidney Foundation as a decrease in systolic blood pressure (SBP) by ≥ 20 mm Hg or a decrease in Mean Arterial Pressure (MAP) by 10 mm

Hg associated with additional symptoms described in the National Kidney Foundation's Kidney Disease Outcomes Quality Initiative (NKF KDOQI) guidelines [74].

3.2.2 Chromophore Extraction

Tissue chromophore concentrations ($[HbO_2]$, $[Hb]$, $[Water]$, $[Lipid]$) were determined by least-squares fitting of the full μ_a spectrum using Beer's law. The fitting method for chromophore concentrations was carried out with an assumption of a spectrally constant background absorption. The fit assumed that the overall absorption spectrum was modeled as the sum of absorption contributions from $[HbO_2]$, $[Hb]$, $[Water]$, $[Lipid]$, Melanin, and the constant background

$$\mu_{a\text{Tissue}} = \varepsilon_{HbO}[HbO] + \varepsilon_{Hb}[Hb] + \varepsilon_{H_2O}[H_2O] + \varepsilon_{Lip}[Lipid] + \varepsilon_{Mel}[Melanin] + \mu_{a\text{Background}}.$$

Melanin concentration was calculated at baseline (pre-dialysis) and then was assumed to remain constant over the course of treatment. The chromophore concentrations and background absorption were then calculated over time using the assumed constant $[Melanin]$ value. Supplemental Figure 2 shows the measured $[Melanin]$ at baseline across self-reported race categories. Additionally, a constant background absorption $\mu_{a,bkg}$ was added to account for tissue heterogeneity or missing chromophores [75]. Extinction coefficients of the extracted chromophores are based on values from literature [22-26,75].

In order to mitigate motion-induced artifacts in our longitudinal tissue measurements a Transient Artifact Reduction Algorithm (TARA) algorithm was applied to the extracted

chromophore measurements [26]. The motion artifacts identified by the TARA algorithm corresponded closely with the timestamped instances of observed motion (described in Chapter 3.2.2). This artifact correction step ensured that the longitudinal chromophore extractions were optimized for quantitative analysis. For Figures 3 E and F local regression smoothing was applied using weighted linear least squares and a 2nd degree polynomial model, implemented with a moving window model that spans 5% of the data set at a time.

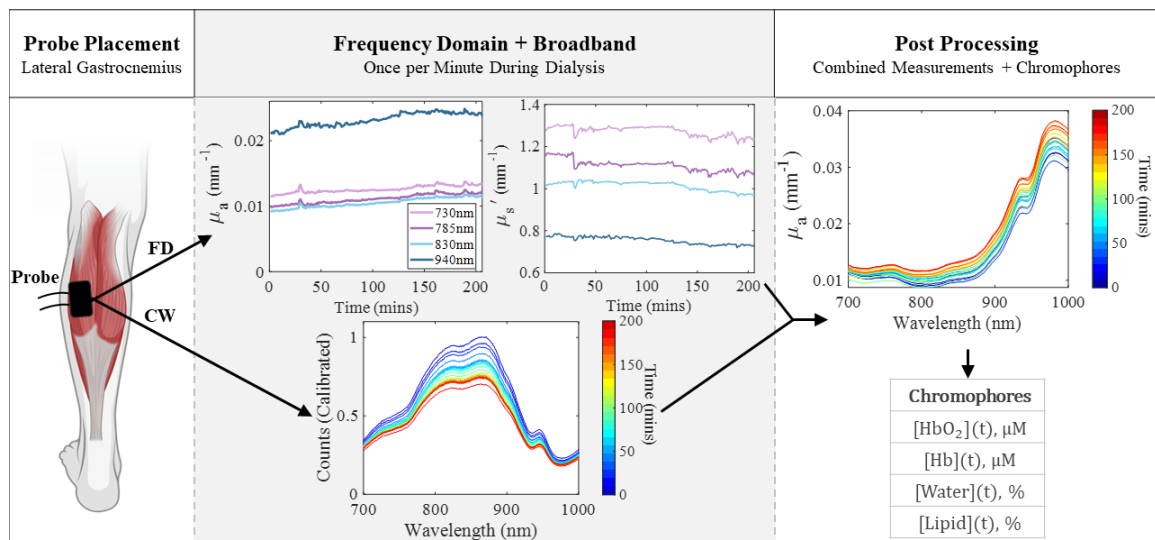


Figure 7 Illustration of the experimental workflow for acquiring and processing optical measurements during hemodialysis using the FD-CW-NIRS clinical system. (Left): The probe was positioned over the main muscle body of the lateral gastrocnemius muscle. **(Center):** FD and CW measurements were acquired once per minute throughout the dialysis session. Top panels show representative time traces of FD absorption (μ_a) and scattering (μ_s') at 730, 785, 830, and 940 nm. The bottom panel displays a representative calibrated CW reflectance spectra at wavelengths from 700-1000 nm recorded over time. **(Right):** Broadband absorption spectra (μ_a) from 700-1000 nm were reconstructed from the calibrated broadband reflectance spectra using MC-LUT enabling chromophore quantification. Chromophore concentrations were estimated using Beer's law. Created with assets from BioRender.com.

3.3 Results

3.3.1 Subject Overview

A total of 27 participants were enrolled in the study (Table 1). The cohort included 16 male and 11 female subjects. The racial distribution was predominantly Black (N=19), with smaller representations from White (N=4) and Other racial groups (N=4). The mean age of participants was 58.8 ± 14.2 years, with an average height of 1.7 ± 0.1 meters and a mean body weight of 78.9 ± 15.4 kilograms. This demographic and clinical profile reflects a representative inpatient population receiving hemodialysis at the Boston Medical Center and ESKD patients in the US.

An example dataset from a single subject illustrating the post processing results and physiological trends during dialysis is shown in Figure 8. Figure 8 A and B display absolute FD and broadband μ_a and μ_s' spectra at three discrete time points (0, 90, and 180 minutes) during hemodialysis. There is an overall increase in μ_a and a decrease in μ_s' . The increase in absorption, further emphasized in Figure 8D, correlates with the increase in $[HbO_2]$ observed in Figure 8E. As shown in Figure 8E, this representative subject exhibited a progressive increase in tissue oxygen saturation (StO_2) and oxyhemoglobin concentration $[HbO_2]$ over the entire course of hemodialysis. This is consistent with expected physiological responses during hemodialysis [38,49].

In addition to changes in tissue oxygenation, changes in tissue water concentration were considered. The Water Ratio, as defined in Lam et al. [45], $[Water]/([Water]+[Lipid])$, was used here (Figure 8F). Lam et al indicates that the Water Ratio may be more agnostic to fluctuations or inaccurate assumptions of μ_s' . We have found

that this metric provided a more temporally stable and less noisy measurement as compared to direct [Water] measurements. The change in Water Ratio showed a net increase over the dialysis session, potentially reflecting fluid redistribution during ultrafiltration. Data outside six mean absolute deviations was assigned a weight of zero. The temporal trends in optical properties and chromophore concentrations observed in this subject were broadly representative of cohort-wide responses, capturing the general trends in increasing absorption, decreasing scattering, and progressive changes in [HbO₂], StO₂, and tissue water content during dialysis. The absolute delta of relative extracted chromophores for all subjects is displayed in Supplemental Figure 3.

Table 1 Demographic and clinical characteristics of study participants (N = 27). Values are presented as mean \pm standard deviation unless otherwise indicated. Fluid removed represents the average ultrafiltration volume per session. Crit-Line refers to subjects whose hematocrit was continuously monitored during dialysis via the Fresenius Crit-Line IV Monitor.

Patients	
Total	N=27
Crit-Line	N=19
Sex	
Male	N=16
Female	N=11
Race	
Black	N=19
White	N=4
Other	N=4
Ethnicity	
Hispanic	N=7
Non-Hispanic	N=19
Other	N=1
Mean \pm StdDev	
Age	58.8 \pm 14.2 (Y.O.)
Height	1.7 \pm 0.1 (m)
Weight	78.9 \pm 15.4 (Kg)
Fluid Removed	1.6 \pm 0.8 (L)

	Median	Range
Dialysis Duration	3	1-4 (Hr)

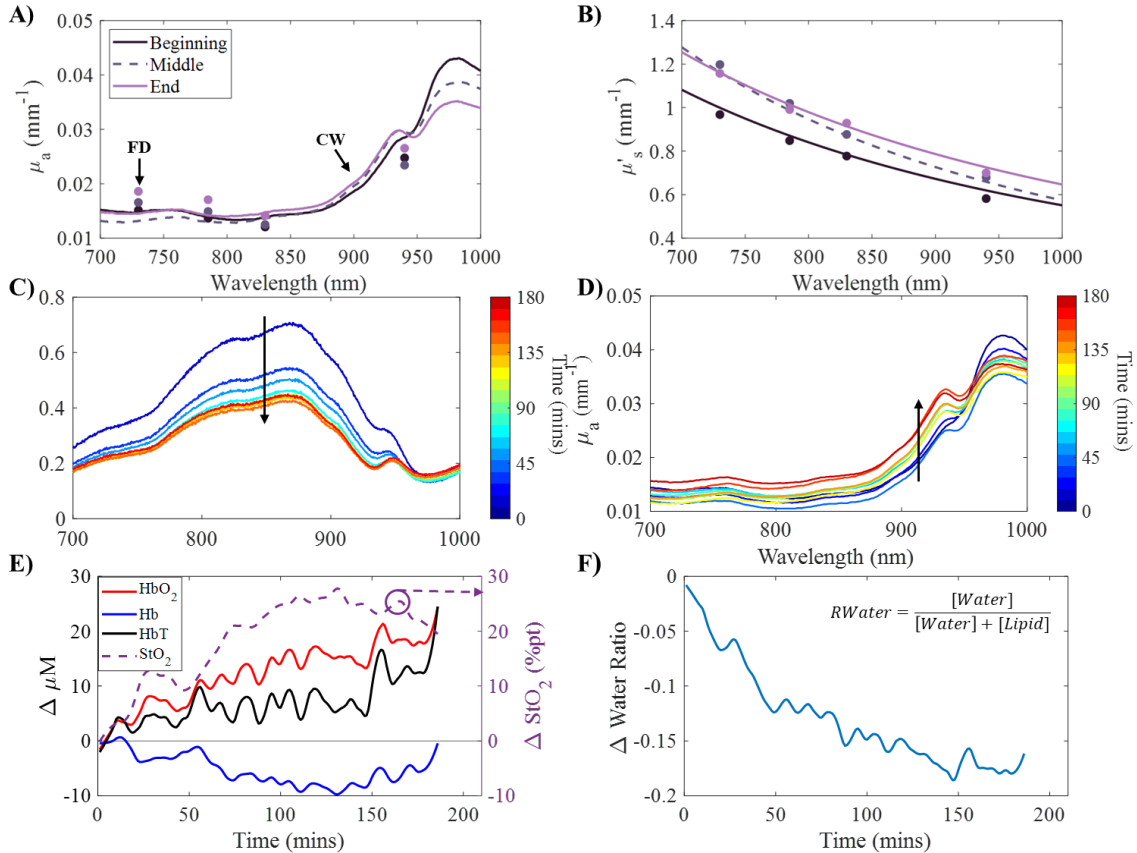


Figure 8 A) Absorption coefficient spectra (μ_a) and B) Reduced scattering coefficients (μ_s') at three time points (0, 90, and 180 minutes). Discrete frequency-domain (FD) wavelengths (730, 785, 830, 940 nm) are shown as data points, while continuous-wave (CW) data span the full 700–1000 nm range. C) Calibrated CW reflectance spectra over time and D) Broadband μ_a spectra, color-coded from blue (start of dialysis) to red (end), arrows show the dominant trend. E) Temporal display of the relative chromophore concentrations changes over hemodialysis: oxyhemoglobin ($[HbO_2]$), deoxyhemoglobin ($[Hb]$), total hemoglobin (HbT) and tissue oxygen saturation (StO_2). F) Change in tissue Water Ratio.

3.3.2 Adverse vs Non-Adverse Events Chromophores

To further correlate FD-Bb-NIRS measurements with physiological changes during dialysis, subjects were stratified into two subgroups: those who experienced an adverse

event during treatment ($N=18$), as defined in Chapter 3.2.1, and those who completed dialysis without an adverse event ($N=9$). Demographic and treatment characteristics for each group are summarized in Supplemental Table 1 and Supplemental Figure 4. No statistically significant differences were observed between groups in terms of ultrafiltration volume or other baseline characteristics.

Group-averaged dynamics of major chromophores and tissue water ratio were then analyzed over the normalized time course of hemodialysis to identify trends associated with adverse events. These longitudinal trends are presented in Figure 9, which displays group means \pm standard error for all subjects over normalized time (% Dialysis Completion). The longest dialysis duration was 227 minutes; two subjects with treatment durations less than half ($t \leq 114$) this time were excluded from the longitudinal analysis to ensure sufficient temporal resolution for trend comparisons. Across hemodialysis, both groups demonstrated a general increase in $[\text{HbO}_2]$ with respect to baseline (i.e., $\Delta[\text{HbO}_2]$) (Figure 9A), with slightly higher variability in the adverse events group, though overall both groups had a similar total mean change of $13.79 \pm 16.37 \mu\text{M}$ for subjects with adverse events and $16.02 \pm 11.39 \mu\text{M}$ for subjects without adverse events in $\Delta[\text{HbO}_2]$. $\Delta[\text{Hb}]$ levels showed slightly divergent patterns (Figure 9B), remaining near baseline or slightly negative for subjects without adverse events, while subjects with adverse events had a higher increase over time. $\Delta[\text{Hb}]$ increased by an average value of $2.06 \pm 6.56 \mu\text{M}$ for subjects with adverse events and $1.01 \pm 3.49 \mu\text{M}$ for those without adverse events during the dialysis. Changes in ΔStO_2 (Figure 9C) exhibit a more rapid rise within the first 25% of dialysis in subjects who experienced adverse events; however, by the end of treatment,

both groups reach a comparable absolute change in StO₂ at an average of 10.25 ± 13.20 % pt for the adverse events group and 9.43 ± 14.52 % pt for the non-adverse group. Most notably, the Δ Water Ratio (Figure 9D) diverged substantially between groups: while the group without adverse events exhibited a gradual decline (with an average of 0.006 ± 0.034 for the adverse event group and -0.04 ± 0.085 for the non-adverse event group over the course of dialysis), which would be anticipated with effective fluid removal, the adverse event group showed minimal change with a slight increase in water ratio. A summary table of the Δ chromophores means, standard deviations, and statistics (2-sided t-test) is provided in Supplemental Table 2. The time courses of Δ [Water] and Δ [Lipid] extractions used to calculate Δ Water Ratio are presented in Supplemental Figure 5.

In addition to assessing temporal dynamics, the overall magnitude of physiological change was quantified for each tissue parameter by calculating the absolute Δ from the beginning to the end of dialysis for each subject (Figure 10). Among the parameters assessed, Δ Water Ratio was the only measure to show a statistically significant difference between groups ($p < 0.05$ by a two-sample t-test), with subjects who experienced adverse events exhibiting notably smaller reductions or even slight increases in Water Ratio compared to those without adverse events. No significant group-level differences were observed for Δ [HbO₂], Δ [Hb], Δ [HbT], or Δ StO₂. The distinct behavior of Δ Water Ratio suggests it may capture relevant fluid-handling differences associated with adverse events and warrants further investigation as a potential marker during hemodialysis. Supplemental Figure 8 displays the time traces of adverse events over % dialysis

completion. Adverse events on average occurred at 51.72% +/- 24.84 % of dialysis completion.

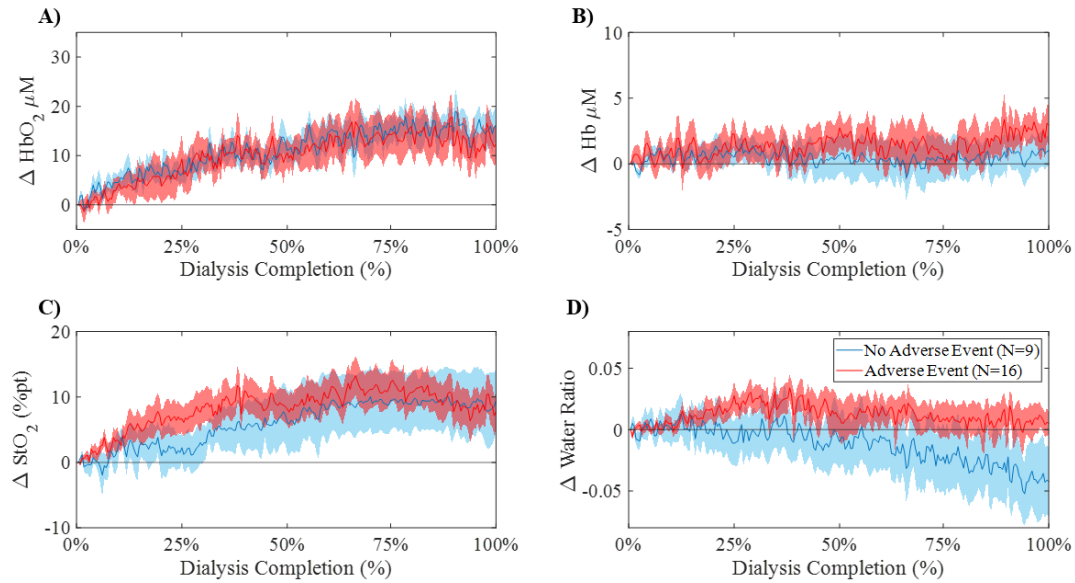


Figure 9 Time-normalized traces (mean \pm standard error) comparing chromophore extractions of subjects with adverse events (red, $N=16$) and without (blue, $N=9$) A) Δ [HbO₂] B) Δ [Hb] C) Δ StO₂ D) Δ Water Ratio. Two subjects with short-duration sessions ($t \leq 114$ min) were excluded.

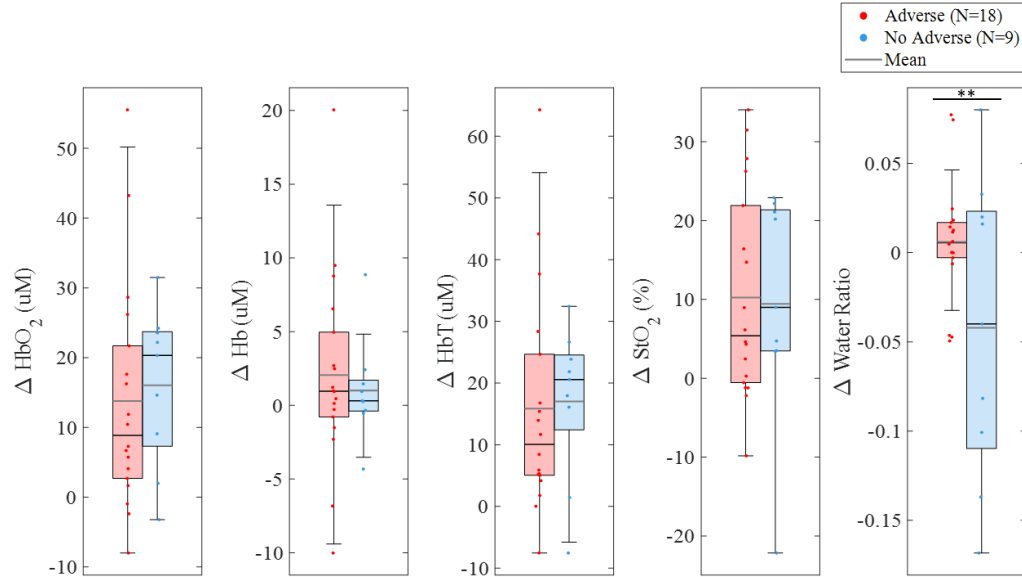


Figure 10 Boxplots of subject values and group means for the absolute Δ [HbO₂], Δ [Hb], Δ [HbT], Δ StO₂, and Δ Water Ratio from the beginning to end of dialysis (100% dialysis completion). Adverse event subjects are shown in red ($N=18$), and non-adverse event

subjects in blue (N = 9). A significant difference was observed for Δ Water Ratio ($p < 0.05$). No other parameters reached statistical significance.

3.3.3 Tissue Scattering of Patients with Adverse vs Non-Adverse Events

Our initial hypothesis related to reduced scattering changes during dialysis was that biological tissue hydration would directly affect the overall reduced scattering value. Specifically, we hypothesized that higher tissue water content would lead to lower reduced scattering due to lower cellular packing, whereas lower hydration status due to dialysis would increase scattering.

However, reduced scattering reflects both the density and size of tissue scatterers, which have been shown to affect the scattering amplitude (A) and the scattering slope (b), respectively [118,119,120]. Parameter A has been shown to be sensitive to the density of scattering centers, while b is sensitive to the size of scatters. With the A and b parameters under consideration, we expanded our hypothesis as follows: As the cellular density increased over dialysis the scattering A parameter would also increase. Also, since the physical size of cellular structures would likely not substantially change during dialysis, so to, the b parameter would not change. An additional consideration is that both parameters are also influenced by the refractive index ratio between the scatterers and the fluid media surrounding them, which may shift dynamically during fluid removal.

To complement the longitudinal analysis of chromophores and tissue water content, the A and b optical scattering parameters were also examined [77], which are shown in Figure 11 A & B. Subjects who did not experience adverse events exhibited higher baseline A values and increasing b over the course of dialysis, while those with adverse events

showed comparatively flatter profiles. Comparison of scattering coefficients at the end of hemodialysis are displayed in Figure 11C. A two-sided unpaired t-test was performed to assess statistical differences between the groups. Of the parameters evaluated, at 100% dialysis completion, scattering coefficient A ($p = 0.0130$) was significantly different between groups.

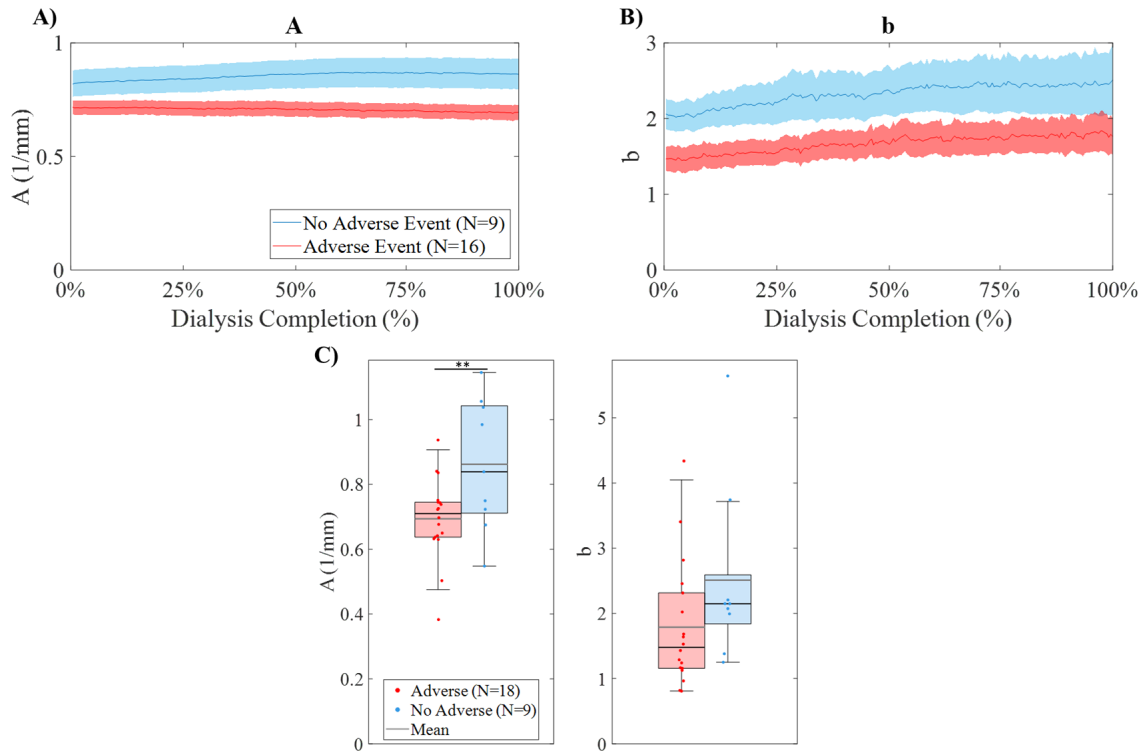


Figure 11 A&B) Longitudinal group-averaged scattering coefficients (A and b respectively) over normalized dialysis time for adverse events (red, $N = 16$) and non-adverse (blue, $N = 9$) subjects. Two subjects with short-duration sessions ($t \leq 114$ min) were excluded. **C)** Box plots of absolute values of scattering coefficients A and b at the end of dialysis for subjects with adverse events (red, $N=18$) and non-adverse (blue, $N=9$). A 2-sided t-test was used to assess whether group means differed significantly from zero ($p < 0.05$). Statistically significant changes were observed in scattering coefficient A.

3.3.4 Discriminant analysis

All measured optical parameters (including chromophore extractions, water ratio, and scattering parameters) were included in a classification analysis to evaluate their ability to differentiate between groups. A three-feature combination of Δ Water Ratio, A, and b yielded the highest classification performance of all tested features, with a true positive of 16, a true negative of 6, a false positive of 3, and a false negative of 2 (Figure 12A). While individual features gave low AUC values (Figure 12B), the combined model achieved a markedly improved Area Under the Curve (AUC) of 0.88 (Figure 12B) for the parameters measured at 100% dialysis completion. These results suggest that multivariate integration of scattering and water ratio parameters may enhance the detection of adverse events in this dataset. Notably, this feature set also demonstrated predictive value earlier in treatment, achieving an AUC of 0.93 at 25% dialysis completion. These results suggest that the FD-Bb-NIRS system may provide clinical utility in early identification of at-risk patients. Supplemental Figure 7 shows the AUC across the three features over dialysis completion %

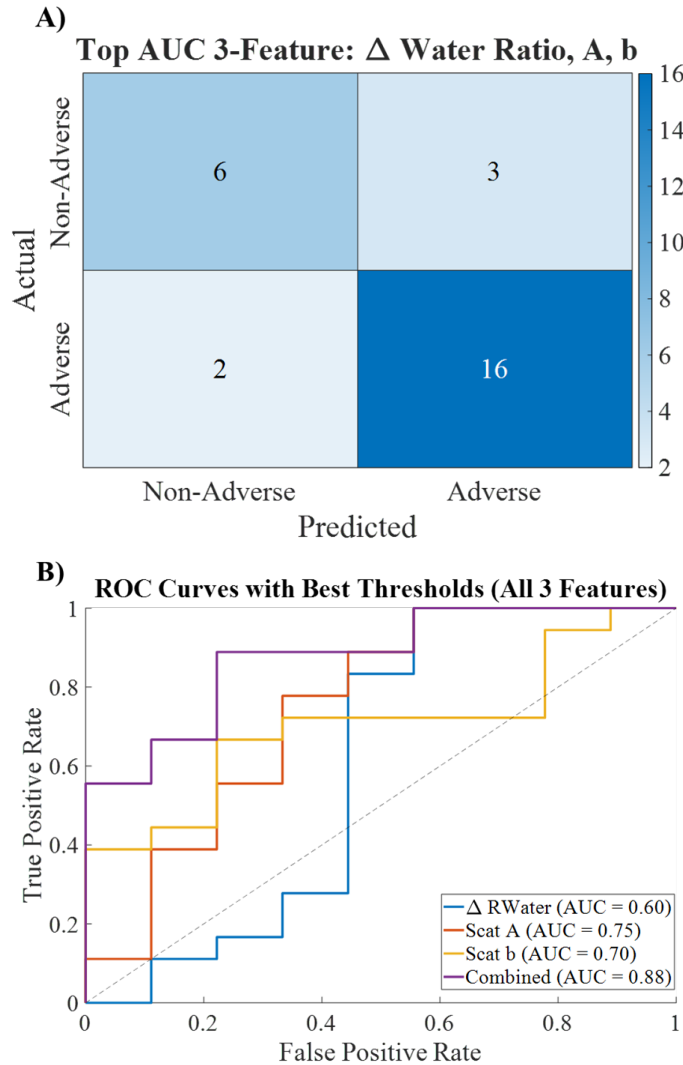


Figure 12 A) Confusion matrix from a top-performing 3-feature classification model (Δ Water Ratio, A, b). **B)** ROC curves showing classification performance of individual features and the combined model. While Δ Water Ratio, A, and b at 100% dialysis completion individually gave low AUC values of 0.6, 0.75 and 0.7 respectively, with the combined model achieved an AUC of 0.88.

3.3.5 Comparison with Crit-Line and Blood Pressure Metrics

To evaluate whether Crit-Line measurements of relative blood volume change (Δ BV) could be used to differentiate between patient groups with adverse vs non-adverse

event, percent changes in hematocrit-derived BV were compared from the start to the end of hemodialysis (Figure 13A). While the adverse event group exhibited a wider distribution of Δ BV values, there was no statistically significant difference between groups. Longitudinal plots of Δ BV are shown in Supplemental Figure 6, no statistically significant difference was found between longitudinal Crit-Line measurements. These findings suggest that Δ BV alone, as measured by Crit-Line, was not a reliable discriminator of adverse events within this cohort. This interpretation should consider that the sample size of Crit-Line (N=19) is smaller than the overall study population (N=27).

This contrasts with Δ Water Ratio (Figure 10), which was significantly different between groups and remains the only tissue-based optical parameter to reach statistical significance. Additionally, a summary of all measured physiological parameters, including chromophores, Δ BV, and systolic blood pressure, is provided in Supplemental Table 2. Among all variables assessed, only Δ Water Ratio was the only optical marker statistically associated with adverse events. Δ Systolic Blood Pressure (SBP) was also identified as a potential statistical marker (Figure 13B). However, it is noteworthy that 16 of the 18 subjects who experienced an adverse event had at least one documented episode of hypotension during dialysis. Supplemental Figures 9 and 10 show the longitudinal and delta chromophore plots of Hypotensive vs Non Hypotensive subject groups. Taken together, these findings suggest that Δ Water Ratio may serve as a distinct optical marker of adverse events and that noninvasive optical measurements could offer physiologically relevant information beyond traditional hemodynamic metrics.

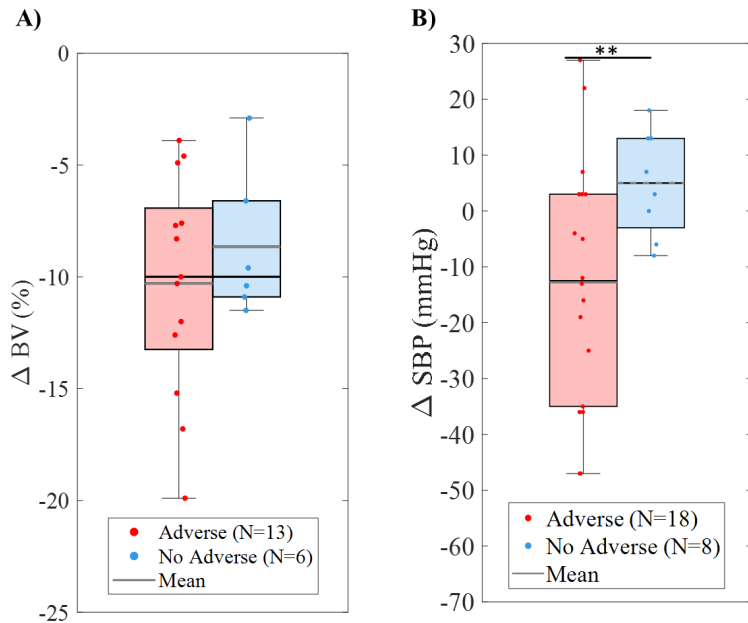


Figure 13 A) Box plots of absolute change in relative blood volume (Δ BV) from start to end of dialysis, as measured by Crit-Line. Subjects with adverse events (red, $N = 13$) and without (blue, $N = 6$) presented similar means. No statistically significant difference was observed between groups. **B)** Box plots of the absolute change in systolic blood pressure (Δ SBP) from start to end of dialysis. Subjects with adverse events (red, $N = 18$) and without (blue, $N = 8$). A 2-sided t-test ($p=0.039$) shows there is a statistically significant difference was observed between groups.

3.4 Discussion

We presented here the findings from a clinical study in which a FD-Bb-NIRS system was used to monitor optical and physiological changes during hemodialysis and evaluated their association with intradialytic adverse events. To date, few optical studies have systematically examined chromophore dynamics during hemodialysis, and none, to the best of our knowledge, have reported FD+CW NIRS measurements to longitudinally monitor tissue hydration status.

Among the parameters analyzed, Δ Water Ratio was the only chromophore related metric to show statistically significant differences between subjects with and without

adverse events. While chromophore trends such as those seen in HbO_2 , Hb , and StO_2 exhibited similar overall magnitudes between groups, Δ Water Ratio diverged substantially. The scattering parameters, A and b , demonstrated clear longitudinal differences and contributed to the top-performing three-feature classification model. When considering conventional clinical measurements, Crit-Line-derived blood volume changes (ΔBV), was not able to differentiate between groups. Although Δ Systolic Blood Pressure (SBP) also reached statistical significance, it is notable that the majority of adverse events (16 of 18) were hypotension-related, potentially narrowing the profile of the average captured adverse event.

The observed group-level divergence in Δ Water Ratio may reflect a mismatch between the prescribed ultrafiltration rate and the subject's vascular refill capacity (plasma refill rate) or tissue water clearance, potentially contributing to the onset of adverse events. A declining water ratio in non-adverse event subjects is consistent with effective interstitial and intracellular water removal, while the relative stability or increase in the adverse event group may reflect a disparity between ultrafiltration rate and vascular refill capacity, leading to insufficient compensation and a higher risk of hypotensive events. These findings suggest that optical measurements of tissue water behavior (interstitial volume) may precede the development of dialysis-related adverse events and thus can be leveraged as an early sign of hemodynamic instability not apparent in currently available clinical measurements such as blood pressure and hematocrit.

There is limited prior literature characterizing chromophore changes in patients during hemodialysis, the preliminary characterizations show here underscore the need for

further investigation in this area. The observed hemodynamic (e.g., HbT increasing by approximately 17 μM) were in agreement with previously published FD measurements taken in the context of dialysis by de Blasi et al. who reported a HbT increase of \sim 18 μM [31]. Additionally, the absolute tissue absorption and scattering values measured in the study population aligned with more broadly published ranges for skin and muscle [60]. Prior work by Pierro et al. measured cerebral blood flow in hemodialysis patients using FD-NIRS. In their preliminary application of coherent hemodynamics spectroscopy (CHS) a significantly prolonged capillary and venous transit times were shown in hemodialysis patients compared to healthy controls, potentially indicating microvascular dysfunction [22]. This NIRS optical work also explores hemodynamic tissue changes in the ESKD population, it differs from our study in physiological focus and analytical approach.

Differences in optical scattering are more challenging to interpret, likely due to multiple contributing factors such as edema, cellular swelling, and changes in vascular dynamics [24,27,37]. Prior literature has shown that as hydration status of tissue changes, scattering is altered [24,27]. This effect is potentially caused by shifts in hydration status altering cell packing density, thus altering the amplitude of μ_s' .

Fluid volume assessment is a vital aspect of hemodialysis care, yet many currently available methods present limitations in clinical utility or quantitative precision. Beyond the current widely utilized clinical protocol of tracking patient's subjective symptoms; suggested clinical techniques such as hematocrit monitoring, bioimpedance, and ultrasound-based assessments often face challenges of accessibility, ease of use, and patient-specific variability [9,10,11]. Direct hematocrit monitoring methods, which involve

blood draws, are labor-intensive and susceptible to operator variability [68,69]. Indirect hematocrit monitoring, with the most common technology being Crit-Line, optically monitors *ex vivo* blood being filtered through the hemodialysis machine and measuring relative blood volume changes. Crit-Line was designed to estimate risk of adverse events, and likelihood of achieving dry weight during a session [68-70,72]. However, measurements have been shown to be inconsistent in predicting adverse events relating to fluid volume shifts, limiting their clinical reliability [68-71]. Crit-Line monitoring was available for 19 study participants. Another method currently used for fluid monitoring is bioimpedance, which utilizes small electrical current to probe core and limb composition. Bioimpedance measurements are influenced by electrolyte shifts and temperature [69,70,73]. Intravascular ultrasound (IVUS), in which an intravenous ultrasound measures the diameter of the inferior vena cava to assess intravascular volume to predict changes in volume as a response to dialysis. This method requires catheterization, which is invasive and often unavailable in routine clinical settings [1,16,17,18,48,68,69]. Current approaches to volume assessment during dialysis remain largely out of reach and inaccurate in current clinical settings.

In contrast to these other techniques, our optical approach offers a noninvasive and physiologically specific alternative, with real-time sensitivity to changes in both chromophore and water content. All the above discussed clinical technologies focus on intravascular volume assessment, while >60% of total body water remains in extravascular spaces, for which there are no clinical methods to assess its flux [78].

A notable confounding factor in this study is that the participant cohort consisted of inpatient dialysis patients, who may differ clinically from the broader, stable, outpatient population, potentially limiting generalizability. Common comorbidities among study participants included: congestive heart failure, diabetes, hypertension, chronic infections, and anemia [2,7,68]. On average, 1.6 ± 0.8 liters of fluid were removed during dialysis. This volume is lower than typically observed in outpatient dialysis populations, which may reflect the higher comorbidity burden of the inpatient study cohort. Previous literature reports an accepted removal rate of 10-13ml/h/kg over an approximately 3.75-hour outpatient dialysis session. Thus, for an individual attending outpatient dialysis with a weight of 70kg, their expected ultrafiltration goal would be between 2.6 to 3.4 Liters) [2,11,79]. The median dialysis duration was 3 hours (range: 1 to 4 hours); however, nine sessions were terminated early due to the onset of severe intradialytic complications such as: the possibility of stroke, severe leg cramping, low blood pressure, blood clots, or onset of malaise or anxiety. These clinical constraints further contributed to variability in fluid removal and treatment duration.

While Δ Water Ratio demonstrated statistically significant group differences, the small sample size (N=27) is a limitation of this study. However, our objective was to examine the feasibility of the FD-Bb-NIRS system as a preliminary clinical study. Future studies with a higher power, larger, more diverse cohorts and a broader range of adverse event types will be important to validate the discriminatory power of the Water Ratio and other optical metrics. Additionally, a limitation of this study is the use of homogeneous Monte Carlo models, which do not account for the layered structure of tissue (skin, adipose,

and muscle) [80,81]. This simplification may lead to inaccuracies in absolute estimates of chromophore extractions. Our prior work has shown that FD-Bb-NIRS is effective at tracking dynamic relative changes in water content and other chromophores, though an overall more accurate quantification of water and lipid may be achievable in the SWIRS domain [62].

While the current study focused on hemodialysis, understanding tissue water dynamics may have broader clinical relevance. Similar methodologies could be used for assessing edema in patients with cardiovascular disease [23,82,83]. FD-Bb measurement techniques may also be useful for non-invasive quantification of hydration level and body composition [84], such as monitoring intentional weight gain or loss, or in sports medicine [85].

3.5 Conclusion

In this preliminary clinical study, a pilot clinical study was conducted using a combined FD-Bb-NIRS system to monitor tissue optical changes during hemodialysis. Among the parameters evaluated, Δ Water Ratio emerged as the only optical metric that significantly differentiated between subjects with and without adverse events. Changes in scattering parameters contributed to multivariate classification. The multivariate classification showed higher specificity and greater statistical significance than the clinically utilized Crit-Line metric in distinguishing adverse from non-adverse event groups. These findings support further investigation of FD-NIRS in a larger and more diverse cohort as a tool to guide ultrafiltration in hemodialysis, a predictive tool for

impending adverse events, and most importantly to assist in objectively defining the dry weight in hemodialysis.

Chapter 4: Aim 3: Develop and validate an FD-SWIRS system

Note: This work was published in the Journal of Biomedical Optics:

Suciú D^a, Pham T^a, Wei LL^a, Guruprasad S^a, Roblyer D^{a,b}. “Frequency domain broadband short-wave infrared spectroscopy for measurement of tissue optical properties from 685 to 1300 nm”. *J Biomed Opt.* 2025 Apr;30(4):045001. doi: 10.1117/1.JBO.30.4.045001.

^aBoston University, Department of Biomedical Engineering, Boston, MA, USA

^bBoston University, Department of Electrical and Computer Engineering, Boston, MA, USA

4.1 Motivation/ Introduction

Diffuse optical spectroscopy (DOS) is a technique that leverages light propagation in highly scattering media to measure tissue optical properties. This technique is also commonly referred to as near-infrared spectroscopy (NIRS) when utilizing wavelengths in the near-infrared (NIR) region (~650 to 1000 nm). DOS and NIRS have been widely applied in medical diagnostics in applications ranging from cancer to neuroscience[21].

Three types of NIRS modalities are commonly used in biological measurements: continuous wave (CW), frequency domain (FD), and time domain (TD) [21,27,28]. Among these techniques, only FD-NIRS and TD-NIRS allow for the decoupling of absolute absorption (μ_a) and reduced scattering (μ_s') from the measured optical signal [55]. Specifically, for FD-NIRS, the absolute measurements of both μ_a and μ_s' can be achieved by using calibrated amplitude and phase information of the detected light after traveling

through tissue [21,32]. One of the limitations of FD-NIRS is the added instrumental complexity compared to CW-NIRS, which typically restricts absolute measurements of optical properties to only a few wavelengths simultaneously. To address this, hybrid FD+CW systems have been developed to acquire absolute broadband μ_a and μ_s' spectra [32,36,37]. Though prior NIRS techniques have focused on quantifying oxygenated and deoxygenated hemoglobin (HbO_2 and Hb , respectively) [21,27], there has been a growing interest over the last decade in using diffuse optical techniques to measure tissue concentrations of water and lipids [25,45-47].

Noninvasive optical measurements of water and lipids may provide utility in a wide range of clinical applications, including chronic conditions such as end stage kidney disease, heart failure, and monitoring the side effects of cancer treatments among others [12,82,86-89]. Other applications include hydration monitoring of athletes and more accurate assessment of body composition during intentional weight loss or gain [85,90]. To date, however, most optical techniques designed to monitor water and lipids in biologic tissues have focused on using NIR wavelengths, especially the 900-1000 nm range [91-93]. Compared to NIR, the short-wave infrared (SWIR) wavelength range (often defined as 1000 to 2000 nm) potentially enables more accurate measurements of water and lipids, as these chromophores exhibit strong absorption in this region, with minimal interference from HbO_2 and Hb (as seen in Fig. 14). The SWIR wavelength range may also provide deep tissue measurements in certain circumstances, due to the lower tissue scattering and lower melanin absorption compared to NIR wavelengths [47]. There are a handful of prior studies that have explored SWIR wavelengths for monitoring water and lipids using diffuse

optical technologies [45,46,94]. To our knowledge there has been no prior work developing SWIR in a combined FD and CW system or similar technology to provide absolute tissue optical properties.

In this study we developed a hybrid FD and CW system to measure broadband and absolute μ_a and μ_s' up to 1300 nm. This frequency-domain broadband SWIR spectroscopy (FD-Bb-SWIRS) system utilizes FD-NIRS measurements from 685-980 nm, and broadband CW measurements from 900 to 1300 nm. Using broadband μ_a , we demonstrated that water and lipid concentrations can be obtained in phantoms and porcine tissue samples. Compared to other current SWIR techniques such as CW-SWIRS and spatial frequency domain imaging (SWIR-SFDI) [46,47,95-97], our approach offers several advantages, including the use of single source detector separation (SDS), direct extraction of optical properties, and greater sensitivity to deeper tissue regions.

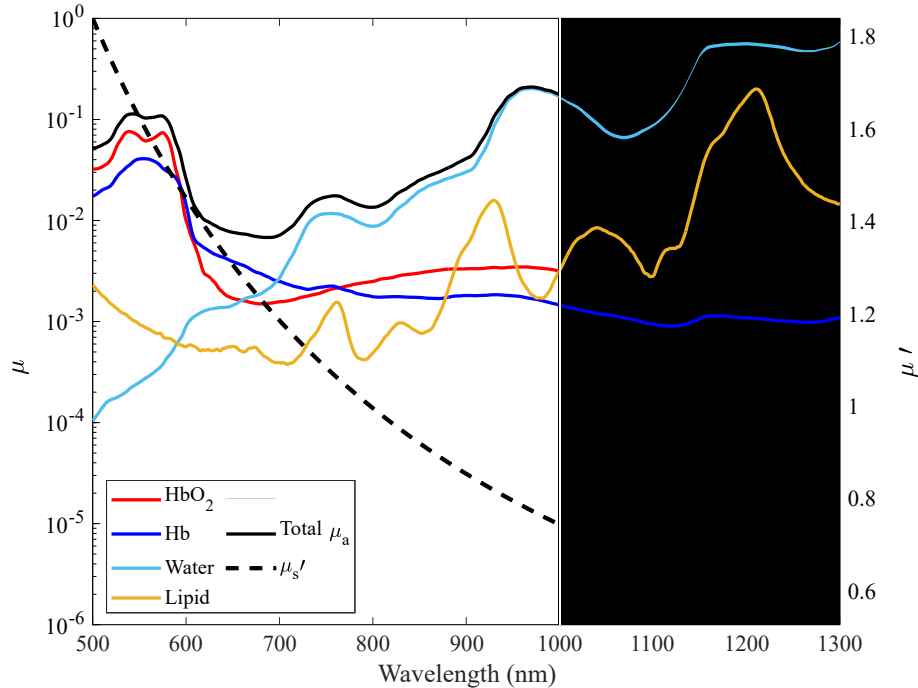


Figure 14 Spectra of absorption coefficients (μ_a) and the resulting reduced scattering coefficient (μ'_s) for four dominant chromophores (oxyhemoglobin HbO_2 , deoxy hemoglobin Hb , water, and lipids) of human tissue. The total μ_a is calculated by adding the individual chromophore absorptions to get the human tissue absorption spectra. The region with white background indicates the NIR spectrum (~650 to 1000 nm) The shaded region indicates the SWIR spectrum (1000 nm and up). These plots are generated from values obtained from typical muscle tissue chromophore concentrations (Total Hemoglobin ($[\text{HbT}]$) = 117 μM , Oxygen Saturation (StO_2) = 65%, [Water] = 60%, [Lipid] = 20%) and scattering parameters ($\mu'_s(800 \text{ nm}) = 1.3 \text{ mm}^{-1}$, $b = 1$) [22,23,24,57,64,77,82,93,98,99].

4.2 Materials and Methods

4.2.1 Wavelength Selection and Inverse Model considerations

One of the challenges of using FD technology with SWIR wavelengths is the combination of high μ_a and low μ'_s typically found in biological tissue. This combination of optical properties typically renders the diffusion equation (i.e., the analytical solution to the P1 diffusion approximation of the Boltzmann transport equation with semi-infinite boundary conditions) inaccurate [28,37]. To address this issue, we evaluated the feasibility of using FD measurements in the SWIR range through Monte-Carlo look-up table (MC-LUT) model (detailed in Chapter 2.4), which are accurate beyond the diffusive regime [31].

We first conducted a simulation study to estimate the uncertainties in optical properties based on the uncertainties in measured FD diffuse reflectance across a wide range of tissue optical properties, spanning those anticipated in the NIR and SWIR wavelength bands. We explored the range of μ_a from 0.002 to 0.2 mm^{-1} and a range of μ'_s from 0.2 to 2 mm^{-1} . For each combination of μ_a and μ'_s , we calculated FD reflectance using the MC-LUT forward model with a modulation frequency of 150 MHz. Then, for each FD reflectance value generated, we created a set of 1000 simulated FD data by introducing Gaussian random

noise to the ground-truth value. We added zero-mean Gaussian noise with $\sigma = 1\%$ to the amplitude and similarly, zero-mean Gaussian noise with $\sigma = 1^\circ$ to the phase of the reflectance data. Throughout this simulation, we assumed that the noise was consistent across all optical property values. Subsequently, optical properties were recovered from the simulated data by applying the MC-LUT inverse model. The uncertainties in μ_a and μ_s' associated with the uncertainties in reflectance data were estimated as standard deviations of the recovered optical property distributions for each specific set of ground-truth optical property values.

4.2.2 Bb-FD-SWIRS Instrumentation

The FD-Bb-SWIRS system combined a FD-NIRS component and a broadband CW-SWIRS component (Fig. 15). Details of the custom digital FD-NIRS component have been described elsewhere [60]. Depending on the specific experiment, the FD system used illumination wavelengths of either 730, 852, 940, and 980 nm (LP730-SF15 Thorlabs, LP852-SF30 Thorlabs, LP940-SF30 Thorlabs, and LDT-980-100-MM CNI) or 685, 730, 852, 915, and 980 nm (FMLE685-025SFOB BlueSky, LP730-SF15 Thorlabs, LP852-SF30 Thorlabs, LP915-SF40 Thorlabs, and FMLE980-025SFOB BlueSky). The laser illumination power for both systems ranged from 6mW to 14mW per laser depending on the wavelengths, such that each system's combined lasers power output was within the American National Standards Institute (ANSI) safety standard. Lasers were modulated at discrete frequencies between 127 and 177 MHz. A set of direct digital synthesizer (DDS) boards was used to simultaneously modulate each laser diode at the selected modulation

frequency. A broad-spectrum tungsten halogen lamp (HL-2000-HP-B, Ocean Optics, wavelength range from 360-2400 nm) was used as the illumination source for the CW measurements.

Custom optical fibers were used for both FD and CW measurements (Fiberoptic Systems, Simi Valley, CA). An eight-in-one source fiber was used for FD measurements in which eight 400 μ m core diameter fiber bundles were combined into a single straight ferrule to deliver light to the tissue sample. A single 3 mm active area fiber was used to deliver CW broadband light to the sample. A 2.3 mm fiber (NA: 0.55) was used for FD detection, and a 1 mm fiber (NA: 0.55) was used for CW detection. All four fibers were housed in a custom aluminum probe holder which was fabricated to position fibers on the sample as seen in Fig. 16.

For FD-NIRS detection, a 3-mm-diameter silicon avalanche photodiode (APD) (S11519, Hamamatsu) was used to detect laser light. A 250 mega-sample per second analog-to-digital converter (ADC) was used to digitize the APD signal. The Goertzel algorithm was implemented in the system microprocessor to calculate the phase and amplitude of the FD reflectance measurements. The CW-SWIRS remitted broadband light was detected using a 256-pixel uncooled InGaAs spectrometer (AvaSpec-NIR256-1.7-EVO, Avantes). The grating and slit width were selected to achieve a usable measurement range of 900-1300 nm with a spectral resolution of 22 nm full width at half maximum (FWHM). The exposure time of the broadband light source varied depending on the experiment and was adjusted to maximize photon counts while avoiding spectrometer saturation. To ensure reliable measurements, we also measured a dark phantom (fabricated

with a high nigrosin concentration as an absorbing agent) using exposure times similar to those used for sample measurements. This allowed us to confirm that the sample intensity counts stayed well above the dark phantom measurements (dark noise) at all wavelengths. The wavelengths at 915 nm, 940 nm, and 980 nm used by the FD-NIRS components of the systems overlapped with the spectral range of the spectrometer.

The FD-Bb-SWIRS system was controlled by a custom graphic user interface (GUI) written in MATLAB (MathWorks Inc., Natick, MA) and operated on a Windows 10 laptop. The FD and CW data were collected sequentially, with the FD amplitude and phase data acquired first at an acquisition time of approximately 11 ms per measurement, followed by the CW reflectance data collection at 25-1200 ms per measurement (experiment dependent). During FD data collection, the CW broad-spectrum lamp was turned off, and only the FD lasers were active. Conversely, during CW data collection, the FD lasers were switched off and the broad-spectrum lamp was turned on. Given the total acquisition time of 35-1211 ms, we do not anticipate significant optical, thermodynamic, or other physiologic changes that would impact the system's ability to capture static tissue optical properties.

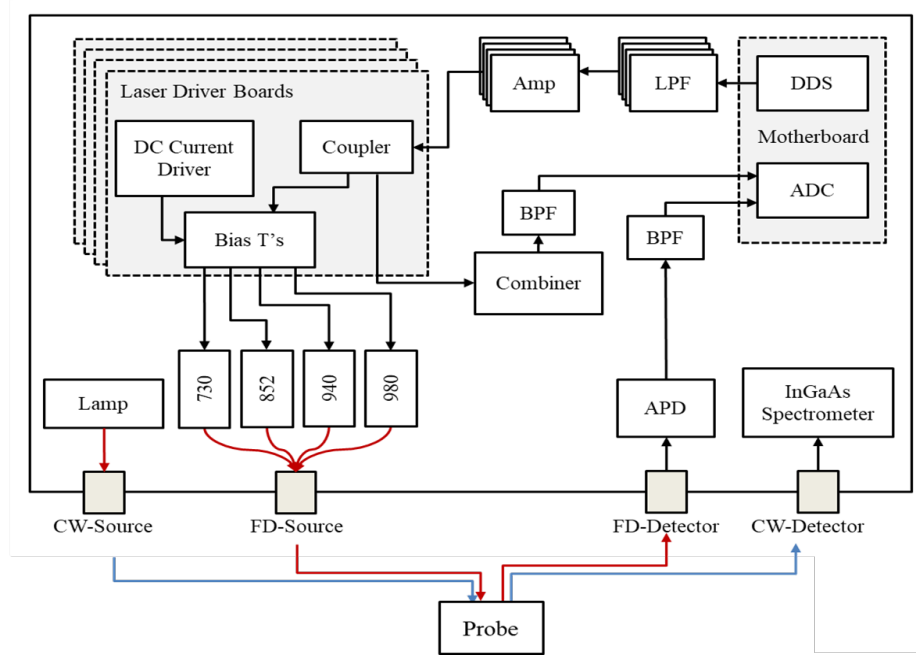


Figure 15 Schematic diagram of the custom FD-Bb-SWIRS system. Key components include ADC = Analog-to-Digital Converter, APD = Avalanche Photo Diode, DC = Direct Current, DDS = Direct Digital Synthesizer, LPF = Low Pass Filter, Amp = Amplifier, BPF = Band Pass Filter. FD source and detector indicated by red lines, CW source and detector indicated by blue lines.

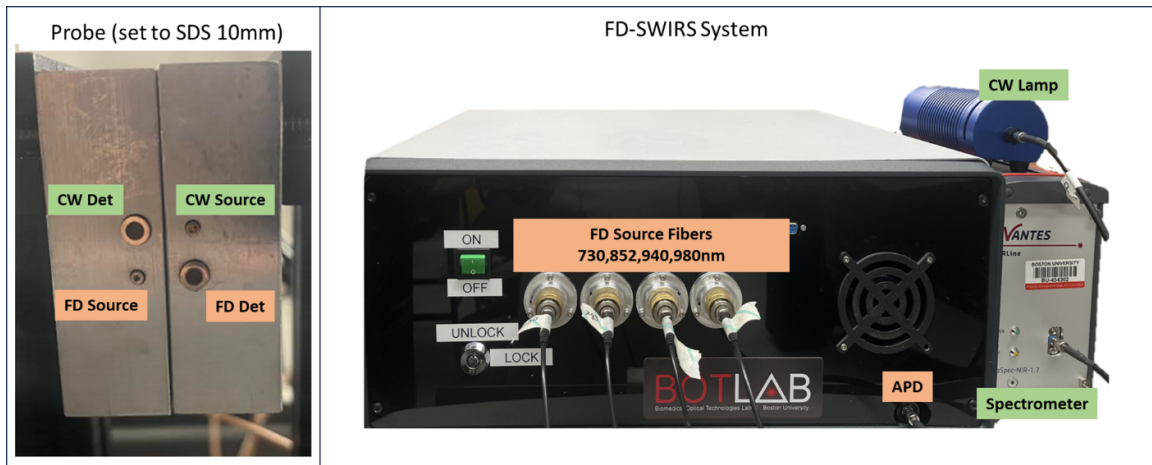


Figure 16 A) The adjustable probe containing the FD and CW source and detector fibers set to a source-detector separation (SDS) of 10mm B) The FD-Bb-SWIRS system. The black enclosure houses the electronic system which is controlled by a laptop.

4.2.3 FD-Bb-SWIRS Data Processing Overview

The processing pipeline for the FD-Bb-SWIRS system is shown in Fig. 17. It is adapted from a previously described algorithm used for combined broadband CW-SWIRS and FD-NIRS [37]. The NIRS processing pipeline is described previously in Chapter 2.3. In this case we leveraged the fact that there is a partial overlap between the FD-NIRS and broadband CW-SWIRS wavelengths to extract μ_a from 900-1300 nm. For data processing, we used the MC-LUT approach for a homogeneous medium with semi-infinite geometry to translate optical properties μ_a and μ_s' to theoretical reflectance data (forward model) and vice versa (inverse model). Look-up tables (LUTs) described in chapter 2.4 were used. For measurements on intralipid-based liquid phantoms (Sec. 3.2), the refraction index and scattering anisotropy were assumed to be $n = 1.33$ and $g = 0.7$ respectively [95]. For measurements on solid phantoms and porcine tissues, the values were set as $n = 1.4$ and $g = 0.9$ [77].

First, μ_a and μ_s' values at 685-980 nm were extracted from the calibrated amplitude and phase values of FD-NIRS measurements using the MC-LUT inverse model. Calibration was conducted using intralipid-based liquid phantoms or solid silicone phantoms. The optical properties of the calibration intralipid phantoms are known based on our previous work [95]. Using extracted μ_s' at 685 to 980 nm, the wavelength dependence of scattering was fit to a power law [77] and the scattering parameters a (scattering amplitude at 900 nm) and b (scattering power) were computed. These scattering parameters were used to obtain spectral μ_s' up to 1300 nm.

Next, broadband μ_a spectra at wavelengths >900 nm were obtained from calibrated CW-SWIRS measurements and known μ_s' spectra obtained as in the previous step. The broadband CW-SWIRS measurements were first calibrated by using a Spectralon standard (Labsphere, North Sutton, NH) to correct for spectral features of the lamp light source. The broadband CW-SWIRS reflectance was then scaled to match with the expected CW reflectance values at the overlapping FD wavelengths, as computed from the optical properties at those wavelengths obtained in the first step using the CW MC-LUT forward model. With the calibrated CW reflectance data and known μ_s' values at 900-1300 nm, we used the CW MC-LUT inverse model to compute μ_a spectrum. Figure 18 shows an example measurement of a liquid phantom composed of intralipid (1.5% lipid by volume), which clearly shows the expected absorption peak of water near 980 nm and 1200 nm.

For tissue measurements, tissue chromophore concentrations, i.e., $[\text{HbO}_2]$, $[\text{Hb}]$, $[\text{Water}]$, and $[\text{Lipid}]$, were obtained from the broadband μ_a spectra (at FD wavelengths from 685-980 nm and CW-wavelengths from 900-1300 nm) by applying the least-square fitting method to minimize μ_a spectra and Beer's law model (Sec. 2.4.3).

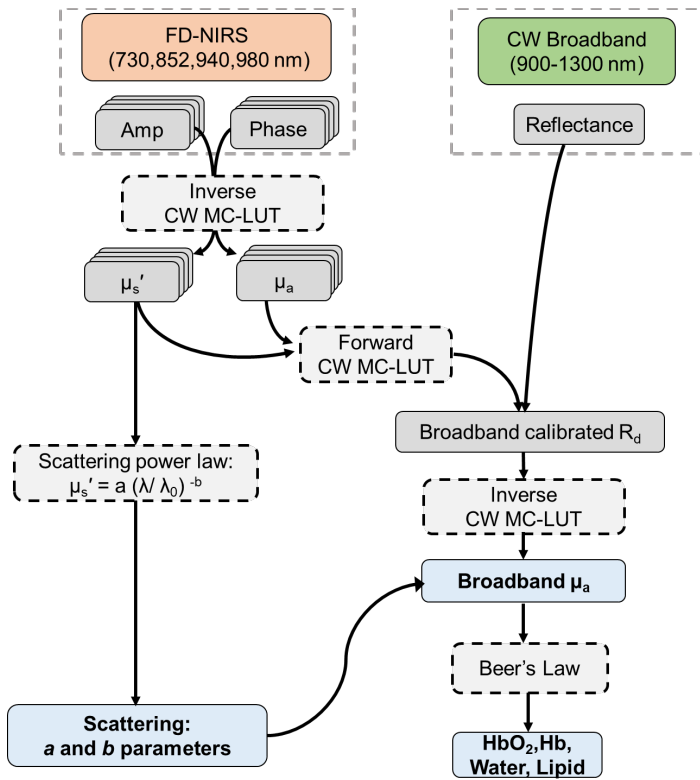


Figure 17 Processing pipeline of the FD-Bb-SWIRS system that combines FD-NIRS and broadband CW-SWIRS systems. Note that $\lambda_0 = 900$ nm for the scattering power law fit.

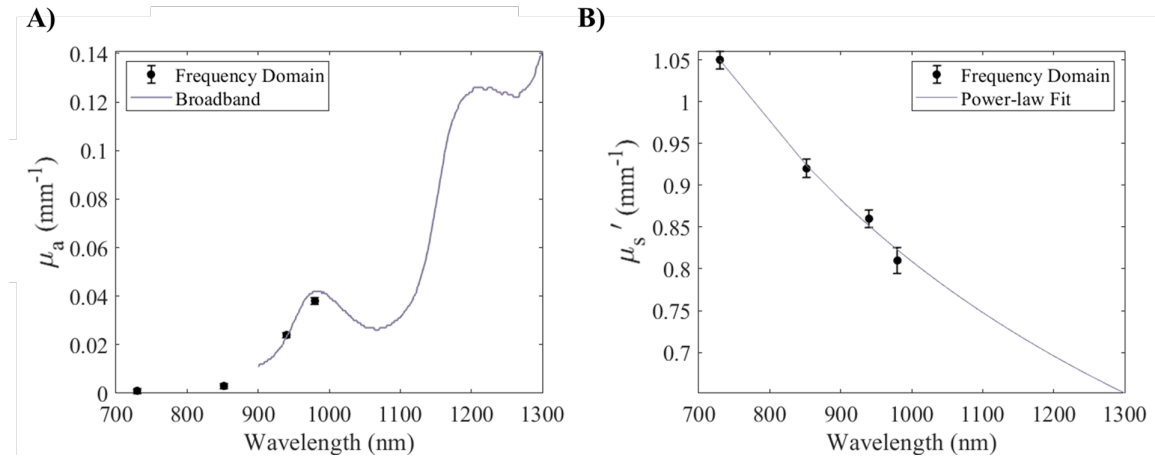


Figure 18 Example FD-Bb-SWIRS measurements of a liquid intralipid phantom composed of 1.5% lipid v/v calibrated against a 1% lipid volume/volume calibration liquid intralipid phantom. The FD-NIRS μ_a and μ_s' are overlaid with the respective CW-SWIRS spectra.

4.3: Validation Experiments

4.3.1 In Vitro Validations on Mineral Oil based Phantoms

In the first experiment, the FD-Bb-SWIRS system was used to measure solid mineral oil-based phantoms with different absorption values to determine the system's ability to measure μ_a spectra up to 1300 nm. Solid mineral oil-based phantoms were fabricated following the method described in Hacker *et al* [100]. In this protocol we substituted nigrosin dye with powdered carbon black dye (Jacquard Products, Healdsburg, CA). Carbon black has a flat μ_a spectra across the NIR and SWIR wavelength ranges [101] while the nigrosin μ_a spectrum decreases with wavelength [102]. Three 125 mL phantoms were fabricated with increasing carbon black dye concentrations: 0.05 , 0.08 , and 0.16 g/L. Each phantoms contained 100 mL of mineral oil (Sigma Aldrich, St. Louis, MO), 0.15 g of titanium dioxide (Sigma Aldrich, St. Louis, MO), 25.14 g of SEBS (polystyrene-block-poly(ethylene-ran-butylene)) (Sigma Aldrich, St. Louis, MO), and 6.70 g of LDPE (low-density polyethylene) (Alfa Aesar, Haverhill, MA). Measurements were taken with a SDS of 10 mm. The FD measurements taken in this experiment utilized wavelengths at 685, 730, 852, 915, and 980 nm FD wavelengths. However, data at 730 and 915 nm were excluded due to phase noise > 2 deg or amplitude noise $> 2\%$. The FD measurements were calibrated against a solid silicone calibration phantom (namely ACRIN9) with known optical properties.

4.3.2 In Vitro Validation on D₂O liquid Phantoms

In the second experiment, the FD-Bb-SWIRS system was used to measure liquid intralipid-based phantoms fabricated from a consistent concentration of intralipid solution (Patterson Veterinary, Houston, TX) and at different concentrations of deuterium oxide (D₂O) (Sigma Aldrich, St. Louis, MO) to test the feasibility of the system to measure changes in μ_a around the water absorption peaks at 980 and 1200 nm wavelengths. Measurements were taken from a solution of 1% lipids by volume held within a 10 cm × 7 cm × 2.5 cm opaque well, able to hold 150 mL of fluid. The lipid solution was incrementally diluted with a similar mixture of 1% lipids and D₂O over 10 titration steps of increasing D₂O from 0% to 90% D₂O. The solution was measured five times per titration step. Measurements were taken with a SDS of 10 mm at 730, 852, 940, and 980 nm FD wavelengths. FD measurements were calibrated against a separate 1% by volume lipid and deionized water (DI) solution. D₂O has approximately 1/10th the μ_a of DI water in the SWIR wavelength range [103]. Thus, as the D₂O replaced H₂O in the solution it was anticipated that the μ_a would decrease while μ_s' remained constant [46].

4.3.3 Ex vitro Validations on porcine samples during desiccation

In the final experiment, the FD-Bb-SWIRS system was validated in *ex vivo* measurements on porcine tissue to assess the ability of the system to monitor water changes in tissue. Measurements were performed on two different porcine tissue samples, a lean muscle (M) sample and a sample with a 7 mm adipose + skin layer on top of the muscle (muscle+adipose, or M+A) (Fig. 19). The samples were acquired fresh and refrigerated.

Before measurements, they were left at room temperature for one hour, assuming they had reached room temperature before the start of the experiment. In this experiment the SDS was set at 15 mm to allow for deeper light penetration. FD measurements were taken at 730, 852, and 915 nm wavelengths. Data at 685 and 980 nm were excluded as phase noise was > 2 deg or amplitude noise was $> 2\%$. Calibration of FD measurements was performed on a solid silicone calibration phantom (labeled as INO9) with known optical properties. The porcine samples were measured with the FD-Bb-SWIRS system in three locations by moving and replacing the probe between each measurement. These locations were marked for subsequent measurements. For the M+A sample, measurements were taken on top of the skin layer. After baseline measurements, the porcine samples were placed inside an electric vacuum oven at 30-40 °C for the next 8-hour desiccation period. The specified temperature range was selected to allow for a continuous evaporation of water, while not inducing protein denaturation [104]. Over the course of 8 hours, the porcine samples were removed once an hour to be weighed and optically measured with the FD-Bb-SWIRS system in the same locations as the baseline measurements. After 10 hours, the porcine sample continued to undergo desiccation and was weighed at every 12 hours until no further weight loss was observed due to water evaporation (after 177 hours in total). The water content at each desiccation time point x was calculated based on weight loss relative to the final recorded weight [105], as shown in Eq. 3:

$$C_x = \frac{m_x - m_c}{m_x} \times 100 (\%) \quad (3)$$

Here, C_x is the water content of the porcine sample at time x , m_x is the measured mass after x hours of desiccation, and m_c is the final mass of the porcine sample recorded at the end of the desiccation period (i.e., after 177 hours).

The μ_a spectra measured at the three locations for each desiccation time point were averaged to get tissue chromophore concentrations ([HbO₂], [Hb], [Water], [Lipid]). The fitting method for chromophore concentrations was carried out including a constant background absorption. Specifically, the model indicates that μ_a spectrum is dependent on the concentrations (C) and respective extinction coefficient spectra (ε) of the chromophores, such that $\mu_a(\lambda) = \sum_i C_i \varepsilon_i(\lambda) + \mu_{a,bkg}$. Here, a constant background absorption $\mu_{a,bkg}$ was added to account for tissue heterogeneity or missing chromophores [93]. Extinction coefficients ε of the four chromophores are based on values from literature, listed in the Appendix. In this experiment, we compared the water content extracted from our FD-Bb-SWIRS method with estimates derived from weight loss (using Eq. 3) and those obtained from FD-Bb-NIRS data (i.e., fitting was performed on the same optical data up to 1000 nm). This comparison aimed to highlight the advantages of the proposed FD-Bb-SWIRS over NIRS in terms of water fitting accuracy.

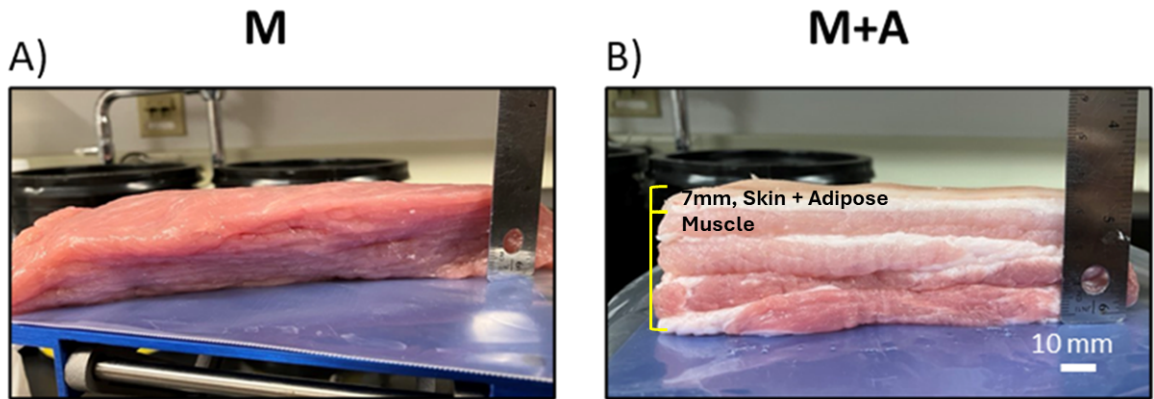


Figure 19 Photos of the two porcine samples, muscle (M) sample and muscle with an adipose layer (M+A) sample. Photos were taken at baseline (before desiccation).

4.4 Results

4.4.1 Uncertainty in Extracted Optical Properties using FD Model

Figure 20 illustrates the simulated uncertainties of extracted μ_a and μ'_s when using FD reflectance data obtained at different optical property values. When subjected to the same noise level in FD reflectance data, we observed increased variances in the recovered μ_a and μ'_s with increasing μ_a . Absorption uncertainty was notably higher in the region with high μ_a and low μ'_s (SWIR regime). In particular, we presented two sets of optical properties representing typical values for human muscle tissue at 800 nm (NIR) and 1200 nm (SWIR). Results indicated that the absorption uncertainty σ_{μ_a}/μ_a was approximately twice as high at 1200 nm compared to 800 nm. Similarly, scattering uncertainty $\sigma_{\mu'_s}/\mu'_s$ was about four times greater at 1200 nm than at 800 nm. The increased uncertainties in optical properties at 1200 nm are further shown by the higher standard deviations observed in the distributions of extracted μ_a and μ'_s , as shown in Fig. S6 A and B (Supplemental Material). Additionally, the differences between the means of these extracted optical property distributions and the simulated ground truth values are notably higher for high μ_a and low μ'_s values but remain relatively uniform otherwise (see Fig. 6S C and D).

The simulation results underscore the challenge of obtaining accurate optical property measurements using only FD technology in the SWIR, in contrast to the NIR. This serves

as motivation for this study to employ a combination of FD-NIRS and broadband CW-SWIRS techniques to improve the accuracy of optical property measurements.

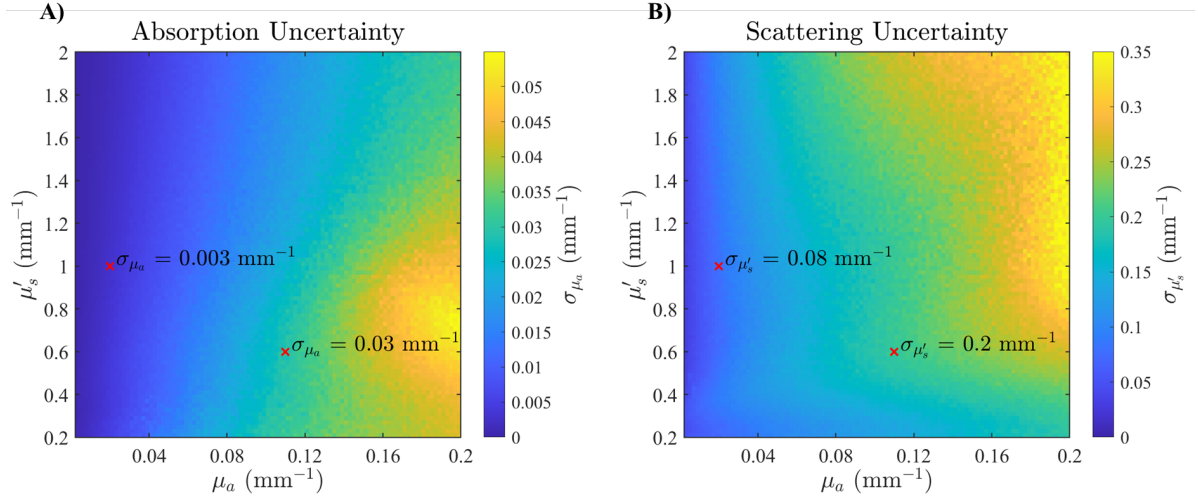


Figure 20 Uncertainties in A) μ_a and B) μ'_s obtained from simulations with frequency-domain (FD) reflectance data. Optical property examples (shown as red crosses) are shown for human muscle tissue at 800 nm ($\mu_a = 0.02 \text{ mm}^{-1}$, $\mu'_s = 1 \text{ mm}^{-1}$) and 1200 nm ($\mu_a = 0.11 \text{ mm}^{-1}$, $\mu'_s = 0.6 \text{ mm}^{-1}$). These plots are generated from values obtained from typical muscle tissue chromophore concentrations (Total Hemoglobin ([HbT]) = 117 μM , Oxygen Saturation (StO₂) = 65%, [Water] = 60%, [Lipid] = 20%) and scattering parameters ($\mu'_s(500 \text{ nm}) = 1.5 \text{ mm}^{-1}$, $b = 0.9$) [22,23,24,57,64,77,82,93,98,99].

4.4.2 In Vitro Validations on Mineral Oil based Phantoms

Figure 21 A and B show μ_a and μ'_s spectra obtained from the three solid mineral oil-based phantoms. FD measurements of μ_a and μ'_s are shown as means and standard deviations averaged from 300 sequential measurements without probe repositioning. As anticipated, μ_a increased linearly with increased carbon black concentration (Fig. 21 A,C) while μ'_s remained nearly constant (Fig. 21B). Though there was some fluctuation in μ'_s over the increasing carbon black concentration, there is no singular trend as seen in Fig. 21D, and thus any drift in the values can be attributed to instrumental/experimental noise or slight variations in phantom creation. All presented measurements were below the 2 degrees

phase error and 2% amplitude error. Lipids absorption peaks at 925 and 1210 nm were present in all phantoms, which is attributable to the previously reported spectra of mineral oil [106]. The broadband μ_a featured a prominent SWIR lipids peak at 1210 nm, approximately 5 times the magnitude of the peak at 925 nm. The slope values of μ_a changes vs carbon black concentrations shown in Fig. 21C are 0.23, 0.26, 0.22, and 0.26 mm⁻¹/(g/L) for 685, 852, 925, and 1210 nm, respectively.

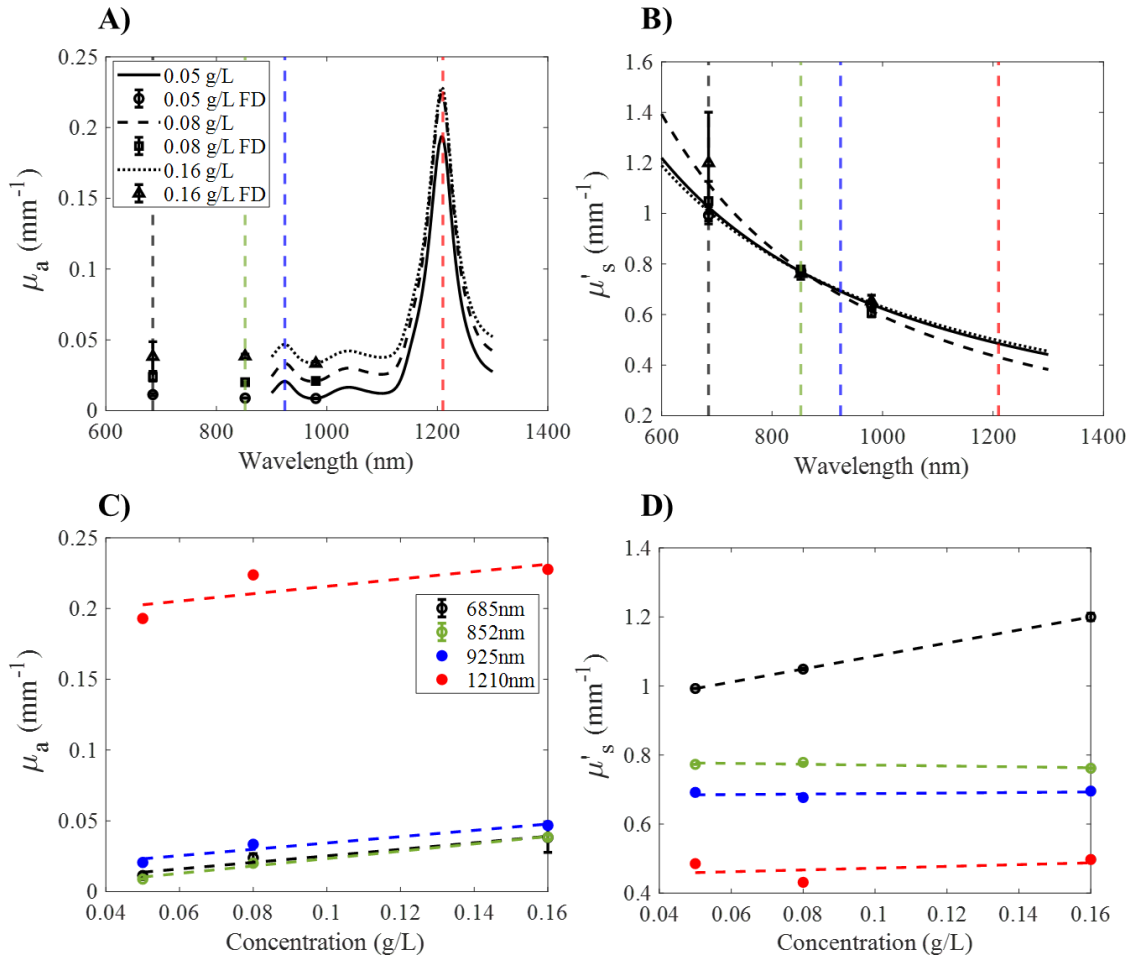


Figure 21 Spectra of A) μ_a and B) μ'_s of three solid mineral oil-based phantoms with carbon black concentrations at 0.05, 0.08, and 0.16 g/L. C) Values of μ_a D) values of μ'_s 685, 852, 925, and 1210 nm vs different the carbon black concentrations in the phantoms. Lines in (C and D) indicate the linear fits across all data points.

4.4.3 *In Vitro Validation on D₂O liquid Phantoms*

Figure 22 A and B show μ_a and μ_s' spectra obtained from the three solid mineral oil-based phantoms. FD measurements of μ_a and μ_s' are shown as means and standard deviations averaged from 300 sequential measurements without probe repositioning. As anticipated, μ_a increased linearly with increased carbon black concentration (Fig. 22 A,C) while μ_s' remained nearly constant (Fig. 22B). Though there was some fluctuation in μ_s' over the increasing carbon black concentration, there is no singular trend as seen in Fig. 22D, and thus any drift in the values can be attributed to instrumental/experimental noise or slight variations in phantom creation. All presented measurements were below the 2 degrees phase error and 2% amplitude error. Lipids absorption peaks at 925 and 1210 nm were present in all phantoms, which is attributable to the previously reported spectra of mineral oil [106]. The broadband μ_a featured a prominent SWIR lipids peak at 1210 nm, approximately 5 times the magnitude of the peak at 925 nm. The slope values of μ_a changes vs carbon black concentrations shown in Fig. 22C are 0.23, 0.26, 0.22, and 0.26 mm⁻¹/(g/L) for 685, 852, 925, and 1210 nm, respectively.

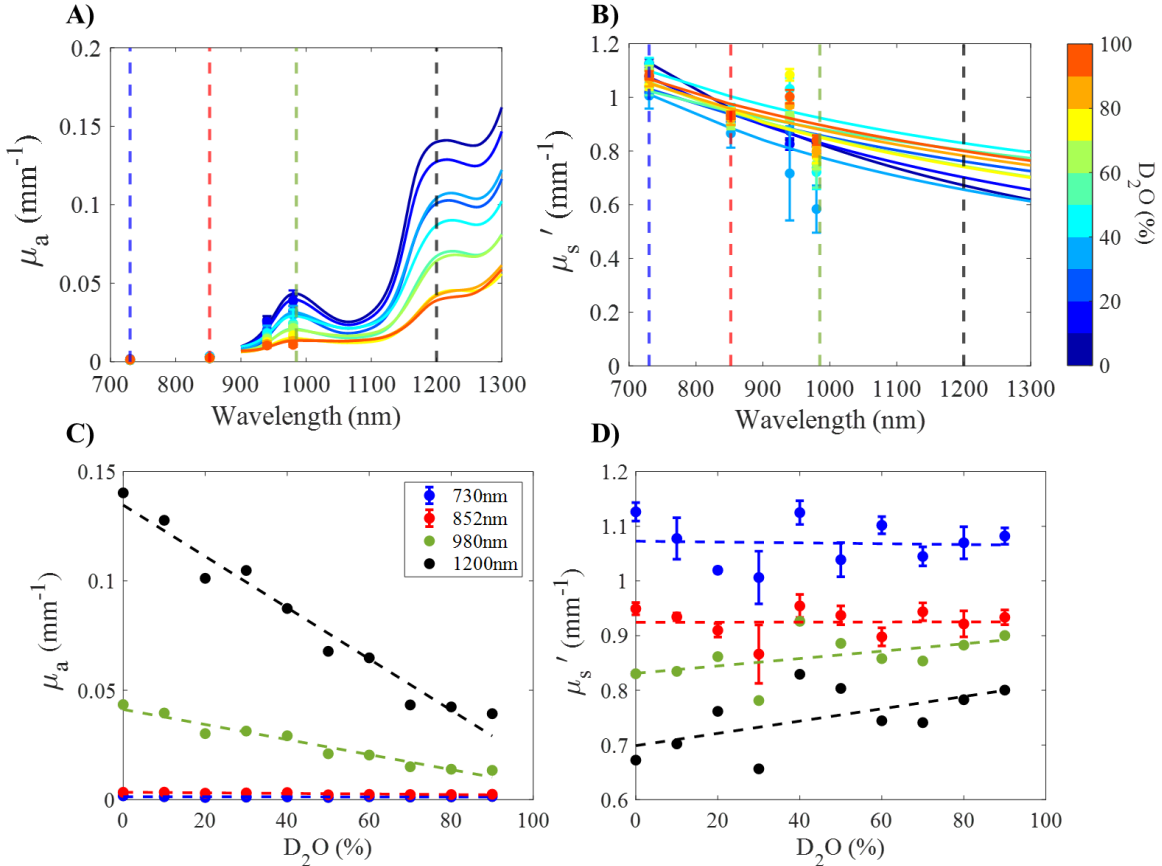


Figure 22 Spectra of A) μ_a and B) μ_s' of the ten titration steps. The titration was preformed from 0% D₂O to 90% D₂O. C) Values of μ_a and D) values of μ_s' at 730, 852 (from FD measurements), 980, and 1200 nm (from broadband measurements) vs the different D₂O concentrations. Lines in (C and D) indicate the linear fits over all data points.

4.4.4 Ex vitro Validations on porcine samples during desiccation

Figure 23 presents μ_a spectra measured from two porcine samples, one consisting solely of muscle (M) and the other with a layer of 7 mm adipose + skin at the top of the muscle (M+A). Fig. 23 also presents the tissue water concentrations [Water] derived from weight estimates (using Eq. 3), FD-Bb-SWIRS optical data, and FD-Bb-NIRS optical data (up to 1000 nm) for the two porcine samples during the desiccation. Measurements were taken from three distinct locations, with the probe being moved and repositioned between each

reading. The μ_a spectra were fit to the Beer's law to extract chromophore concentrations including a constant background absorption. The raw intensity measurements for the porcine samples are discussed in Supplemental Materials, Figure 12.

At baseline (prior to desiccation), the proposed FD-Bb-SWIRS method measured [Water] as 70 ± 4 % for the M sample and 40 ± 2 % for the M+A sample. The extracted [Lipid] was 9.3 ± 0.5 % for the M sample and 45.8 ± 0.7 % for the M+A sample. The constant absorption background $\mu_{a,bkg}$ was 0.003 ± 0.003 mm^{-1} for the M sample and $1.7 \pm 0.1 \times 10^{-6}$ mm^{-1} for the M+A sample. From baseline to the end of desiccation, [Lipid] measured by FD-Bb-SWIRS increased slightly in the M sample (from 9.3% to 11.9% on average) and remained relatively stable in the M+A sample (from 45.8% to 44.7% on average). Over the 8-hour desiccation period, the M sample exhibited minimal variation in the measured [Water], increasing slightly from an average of 70% at baseline to 72% after 8 hours. This negligible change closely aligned with weight-loss-based estimates (using Eq. 3), which indicated 71% at baseline and 68% after 8 hours. In contrast, the M+A sample showed a more pronounced decrease in FD-Bb-SWIRS measured [Water], dropping from an average of 40% at baseline to 26% after 8 hours. These measured values differed from the estimated water content from weight loss, which indicated 54% at baseline and 51% after 8 hours. Throughout the desiccation process, the FD-Bb-NIRS method consistently underestimated water content compared to both the FD-Bb-SWIRS chromophore extractions and the weight-loss-based estimates in both tissue samples (Figure 23 E and F).

The discrepancy in estimated water content between FD-Bb-SWIRS and weight estimates for the M+A sample is likely due to the relatively small 15 mm source-detector

distance, which likely resulted in increased sensitivity to the skin and adipose layers while providing much less sensitivity to the muscle layer [66,107]. Thus, the lower [Water] values measured in the M+A sample may be attributed to the lower water content in adipose tissue compared to muscle [84,108,109]. In contrast, the weight-loss-based water content estimates for the M+A sample likely reflect contributions from both muscle and adipose tissues.

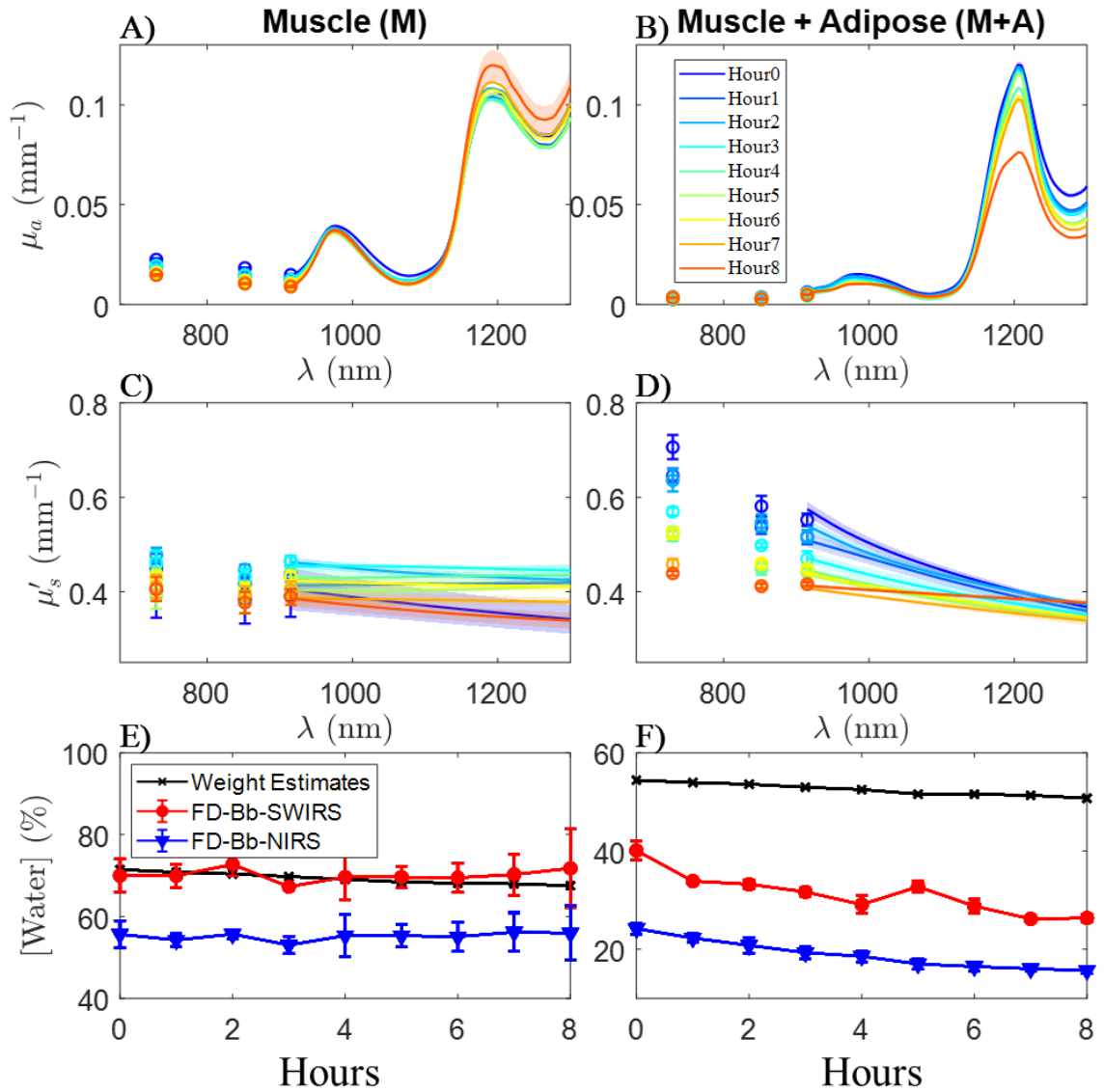


Figure 23 Optical properties and chromophore extraction results for two porcine tissues: a muscle (M) sample and a muscle with adipose layer (M+A) sample. Data were collected every hour over an 8-hour desiccation period. μ_a spectra A&B) and μ_s' spectra C&D) are presented for each desiccation hour, with values shown as means and standard errors based on three separate location measurements. Panels E&F) display the extracted water concentrations for both samples over time, with means and standard errors from measurements at three distinct locations.

4.5 Discussion

We presented here a combined FD and CW system to measure μ_a and μ_s' from 685 - 1300 nm. To the best of our knowledge, this is the first combined FD and CW system capable of quantifying water and lipids in the SWIR regime (i.e. > 1000 nm).

The system was shown to be sensitive to μ_a changes in mineral oil-based phantoms with increasing concentrations of carbon black. A similar trend in μ_a and carbon black concentration was observed in Maneas et al [110] in which μ_a increased linearly with carbon black concentration. The mineral oil-based phantoms also exhibited strong μ_a peaks at 925 and 1210 nm, characteristic of lipid absorption. Additionally, the FD-Bb-SWIRS system was shown to be sensitive to absorption changes due to water content in the D₂O titration experiment. Here, prominent absorption peaks were observed at 980 and 1200 nm, characteristic of water absorption.

The system was also able to quantify changes in μ_a and μ_s' , as well as water and lipid concentrations in *ex vivo* porcine tissues. To the best of our knowledge, this paper is the first to compare NIR vs. SWIR optical window in a hybrid FD and CW broadband system in terms of the accuracy of water content extraction in biological tissue. Our results demonstrated that the proposed FD-Bb-SWIRS system provided better estimations of tissue water content measured by weight-loss-based estimates. In this *ex vivo* experiment,

both lean muscle (M) and fatty muscle + adipose (M+A) porcine tissues were measured, which had substantially different properties and trends during desiccation. Optical measurements showed lower water content at baseline values in M+A than in M sample. This could be explained because in the M+A tissue, measurements were sensitive to the more superficial skin and adipose layers where there is a lower water content than in muscle [109]. Our optical measurements on M and M+A samples showed similar spectral features to those measured on porcine muscle and pure fat tissue samples, respectively, as reported in Damagatla et al [28]. Specifically, M sample showed clear water absorption peak at 980 and a broad peak at 1200 nm, while M+A sample showed a more prominent and narrow lipid absorption peak at 1210 nm. Bashkatov et al reported a muscle water content of $73 \pm 0.5\%$ [111] which is similar to our measurements of $70 \pm 4\%$ for the M sample at baseline. Lam et al reported averaged water contents of 43% and 56% for porcine tissue samples with thick and thin adipose tissue layer, respectively [45]. Our water content estimates for our M+A measurements are at $40 \pm 2\%$ aligning within the range of values reported from Lam et al. After 8 hours of desiccation, water changed more significantly in M+A sample (about an average 14%) as compared to M sample. This may be because the superficial tissues (e.g., skin and adipose) probed by our optical measurements may undergo different proportional changes in water content during the desiccation process compared to pure muscle tissue. When compared to prior dehydration assessments of porcine skin tissue our findings report similar trends. In Yu et al there is a marked decrease of $\sim 15\%$ in water over the first 8 hours of dehydration of a porcine dermis sample [105], which we see similar trends to in the M+A sample.

Compared to prior SWIR measurement techniques, the FD-Bb-SWIRS system presented here has several important and distinct characteristics. Importantly, the use of FD measurements provided absolute quantification of tissue optical properties both at the FD measurement wavelengths, and then from 900-1300 nm through scaling of our broadband CW spectroscopy data. In contrast, our prior work in the development of a CW wearable SWIR probe utilized multiple SDS as well as a deep neural network to extract water and lipid concentrations, without direct extraction of optical properties [46]. Similarly, other works such as Nachabe et al utilized spectral shape constraints to fit for scattering parameters and tissue chromophores directly without extracting tissue absorption [25]. Our method allows for more direct extractions of chromophores, such as water and lipids, from absorption measurements without the need for spectral constraint assumptions on raw optical data. Nachabe et al also differed from our own in that they used only CW measurements and utilized a very short SDS of 2.48 mm, whereas our system used either 10 mm or 15 mm SDS allowing for measurements of deeper tissue regions. Additionally, our measurements utilized both NIR and SWIR wavelength ranges so that concentrations of blood oxy- and deoxy-hemoglobin could be included in our chromophore fits in future work.

In comparison to prior works utilizing the NIR wavelength band to extract tissue water and lipids concentrations [45,90,112], our method captures both the first and second lipid and water absorption peaks. As expected from the known extinction values, our findings confirmed that the 1200 nm absorption peak is more sensitive to changes in water and lipids compared to the 900-1000 nm range. For example, in the D₂O-H₂O titration, the slope of

relationship between H_2O concentration and μ_a was approximately four times steeper at 1200 nm compared to 980 nm (Fig. 22C). This is likely to assist in the detection of more subtle changes in tissue water and lipid concentrations.

We have previously reported on extending SFDI to the SWIR wavelength band [47,95,97]. SFDI is non-contact and uses spatial modulation to extract quantitative optical properties over a wide field. One major difference between SWIR-SFDI measurements and the FD-Bb-SWIRS measurements presented here is the depth of penetration. SFDI has a relatively shallow penetration depth, typically ranging from a few hundred microns to approximately 3 mm [47,95]. In contrast, the direct-contact configuration and spatially separated source and detector fibers used in FD-Bb-SWIRS potentially allows for deeper tissue measurements, reaching up to ~8 mm inside the tissue for the SDS of 15 mm used in the *ex vivo* experiments [45,61].

The ability to non-invasively quantify water and lipid content using FD-Bb-SWIRS may be important for several clinical scenarios. For example, the volume status of patients receiving hemodialysis (HD) is not currently directly assessed and it is estimated that 20-50% of all dialysis patients are inadequately dialyzed [12,18,68,88]. Direct measurements of tissue water content with FD-Bb-SWIRS might help with the management of administration of dialysis for these patients. Similarly, this or similar technology could assist with monitoring fluid overload and edema in patients with cardiovascular disease, especially heart failure [82,83]. This technique may also be useful for non-invasive quantification of hydration level and body composition [84], such as monitoring intentional weight gain or loss, or in sports medicine [85]. Finally, changes in lipid concentrations

have been shown to relate to chemotherapeutic response in breast cancer [86,87,92,97,113].

One limitation of this work was the use of a relatively small SDS of 15 mm or less. This was primary due to the inability to collect useable measurements near the strong 1200 nm absorption peak of tissue at longer SDS. In the future this might be improved with higher illumination power near this wavelength band and/or improved detector sensitivity. Another limitation was the use of homogenous MC models, which are appropriate for homogenous liquid phantoms, but fail to capture the layered structure of tissue, including skin, adipose, and muscle [95,81].

4.6 Conclusion

In summary, in this work we designed and fabricated a FD-Bb-SWIR device for the characterization of tissue optical properties up to 1300 nm. The system's sensitivity to changes in μ_a at both the water and lipid absorption peaks in the NIR and SWIR was validated through both solid and liquid phantom titrations in the carbon black and D₂O experiments. Additionally, the system's ability to extract water concentration changes *ex vivo* was showcased via chromophore extractions during a porcine desiccation experiment. In the future, this technique has the potential to provide sensitive water and lipid measurements for a variety of clinical applications.

Chapter 5: Discussion and Conclusions

5.1 Summary of Findings

Presented here is the initial design and application of the FD-Bb-NIRS optical system for the noninvasive monitoring of tissue hydration during hemodialysis. The FD-Bb-NIRS system was used in a preliminary clinical study, in which twenty-seven patients undergoing hemodialysis were monitored continuously. The FD-Bb-NIRS system was able to capture distinct chromophore trends over the course of treatment. Group-level analyses revealed that Δ Water Ratio was the only optics based parameter that could, with statistical significance ($p=0.0313$), distinguish between patients who experienced intradialytic adverse events from those who did not. When considering multivariate classifications, a three-feature model utilizing Δ Water Ratio, and scattering parameters A and b were able to not only discriminate adverse events post dialysis but also showed potential for an early warning sign of adverse event by demonstrating strong discriminatory performance early in treatment. In contrast, currently clinically available metrics such as Crit-Line were not able to discriminate between the two groups.

Following our findings in the FD-Bb-NIRS study, the range of the hybrid FD+CW spectroscopy was extended into the SWIR wavelength range. The FD-Bb-SWIRS system was developed and validated, which was able to extract broadband absorption and reduced scattering between 900-1300nm. Validation experiments were performed with a carbon black titration on mineral oil phantoms, a D_2O liquid phantom titration, and a porcine tissue desiccation experiment. It has been demonstrated here that the FD-Bb-SWIRS system could accurately recover absorption and scattering spectra. The system also reported water

and lipid concentrations more accurately than the FD-Bb-NIRS system, proving that by utilizing the SWIRS wavelength range could provide heightened sensitivity to tissue hydration in future clinical studies.

By demonstrating both clinical feasibility in the NIR and technical feasibility in the SWIR, this work establishes a promising tool for comprehensive tissue hydration monitoring hemodialysis and related clinical settings.

5.2 Impact and Innovations

The clinical impact of this work lies in demonstrating that DOS technologies have the potential to provide meaningful insights into the fluid dynamics of patients during hemodialysis, a setting where current monitoring tools remain inadequate.

Hemodialysis patients face high risks of intradialytic adverse events due to fluid mismanagement. Often, clinical decisions are guided by crude indicators such as monitoring patients for secondary symptoms of discomfort or intermittent changes in blood pressure. By the time in which symptoms are occurring an adverse event has already occurred. Even widely used technologies such as Crit-Line hematocrit monitoring are limited in their ability to consistently predict adverse outcomes.

This dissertation showed that tissue-level optical biomarkers can bridge this gap. The Δ Water Ratio, proved to be a stable and physiologically relevant hydration metric, distinguished patients who experienced adverse events from those who did not, while scattering parameters offered complementary discriminatory power. Importantly, the integration of these metrics into a multivariate model enabled not only accurate classification of adverse events but also early prediction during treatment. This finding

highlights the potential for optical monitoring such as the FD-Bb-NIRS systems to serve as a real-time early warning system for hemodynamic instability, allowing clinicians to adjust ultrafiltration strategies before complications arise. Furthermore, by extending a FD+CW system into the SWIR range the existing technologies have been innovated upon and have allowed for future clinical monitoring systems that explore a more hydrodynamically sensitive range.

The ability to track hydration shifts within tissue also carries broader clinical implications. Our system could not only help guide dialysis treatments but could potentially be utilized in volume management in intensive care units, in monitoring cardiovascular disease, or in the monitoring or treatment of other chronic diseases where fluid imbalance drives morbidity. Apart from the critical care space this technology could be used in assessing hydration or lipid levels of athletes during training or allow for general practitioner doctors to track the lipid and hydration status of individuals undergoing intentional weight gain or weight loss.

5.3 Future Work

The work in this thesis provides many potential future directions, some of which are described below.

5.3.1 SWIRS Human Measurements (and updates to the FD-Bb-SWIRS System)

The FD-Bb-SWIRS system demonstrated a high sensitivity to changes in water (as shown in Chapter 4), however, transitioning to in vivo human measurements introduces new challenges. The high absorption properties of tissue in the SWIR range significantly

reduces light penetration and limits the useable SDS with the FD-Bb-SWIRS system. This absorption effect can make it difficult to obtain signals at depths sufficient for probing muscle and deep tissue. Figure 24 shows the spectrometer measurements of the forearm of a healthy volunteer at a 15 mm SDS with the FD-Bb-SWIRS system. The count level around 1200 nm is so close to dark that any attempts to extract broadband absorption would be unreliable.

There are several methods that could potentially resolve the current issue and allow for noninvasive tissue hydration monitoring with SWIRS wavelengths. First, by increasing the laser powers while ensuring compliance with ANSI safety standards, could help improve signal from tissue. In order to increase laser power without exceeding ANSI parameters each laser would have to be sequentially illuminated and measured, as currently all lasers are multiplexed. These modifications to the existing FD-Bb-SWIRS system could make it possible to use a longer SDS of 15-20 mm while still receiving adequate signal from tissue. This would allow for enhanced sensitivity to water and lipid changes in deep tissue, enabling meaningful hydration monitoring methods in clinical settings.

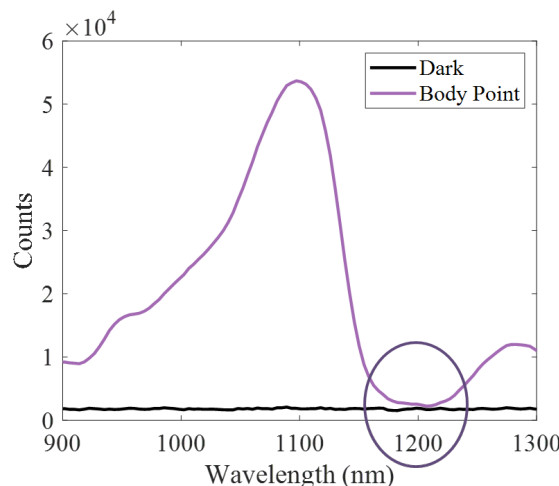


Figure 24 The raw spectrometer counts taken of a healthy volunteer's forearm compared to a dark calibration phantom at 15mm SDS.

5.3.2 Multi-Layer Monte Carlo Simulations

The MC simulation models utilized in this dissertation assumed a semi-infinite homogeneous media, which is a simplification of the complex layered anatomy encountered *in vivo*. Human tissue consists of layers of skin, adipose, vasculature, and muscle that all contribute uniquely to the absorption and scattering properties of the entire tissue. Future works should consider applying a multi-layer MC model incorporating the features of human tissue. Previous work conducted by our group has quantified the sensitivity of multi-layer MC models on tissue optical property extraction [117].

This would result in some changes to data acquisition in clinical and healthy volunteer studies. A colorimeter, or Fitzpatrick scale questionnaire should be used to estimate the participants' melanin concentration. Additionally, a handheld ultrasound can be used to estimate the skin and subdermal lipid thickness. All these parameters should be utilized to allow for more accurate MC modeling for optical feature extraction. Multi-layer simulations would enable more accurate inverse models, reduce partial volume effects, and improve chromophore recovery in heterogeneous tissues. These approaches could potentially assist in quantifying compartment-specific shifts, providing critical insight into whether optical signals primarily reflect vascular, interstitial, or intracellular fluid changes. Such refinements would strengthen the physiological interpretation of optical biomarkers and improve their clinical reliability.

5.3.3 Further Clinical Studies and Exploring the three-compartment model

A central challenge in dialysis care is balancing fluid removal with patient tolerance, which depends on interactions between three fluid compartments: vascular, interstitial, and intracellular (Figure 25). The vascular compartment is the direct target of ultrafiltration, with its volume continually replenished from the interstitial/cellular space (plasma refill). Based on the clinical understanding of the three compartment model, when ultrafiltration outpaces vascular refill, intradialytic hypotension and other complications arise [10,13-16,68].

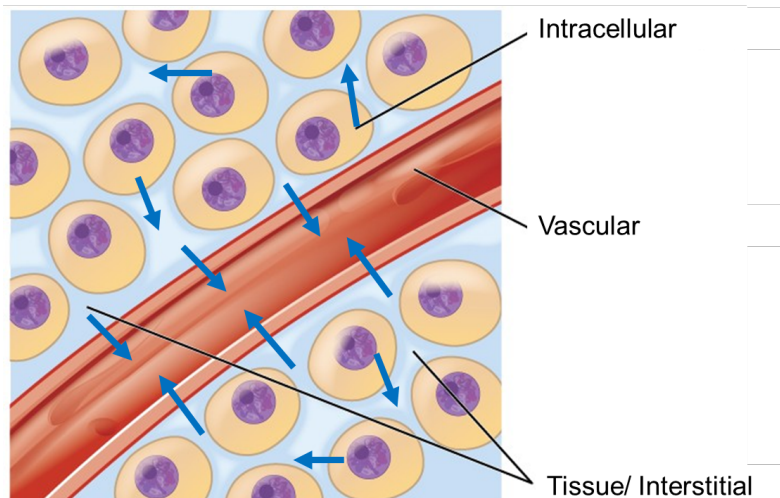


Figure 25 Diagram showing the three-compartment fluid model during dialysis. Blue arrows indicate the movement of water as fluid is removed from the vascular space by ultrafiltration, with sequential refilling first from the interstitial and then from the intracellular compartments. Future work will focus on identifying optical signatures corresponding to these compartmental shifts in tissue fluid during vascular refill. (Modified from OpenStax CNX (OpenStax.org))

Optical monitoring via the FD-Bb systems could provide a promising approach to exploring these compartmental dynamics in real time. Hemoglobin-based signals reflect vascular changes, while Δ Water Ratio may provide insight into shifts between interstitial

and intracellular water. Scattering parameters, which may be sensitive to cellular packing and size, may further inform on intracellular hydration changes. By combining these optical markers with models of fluid kinetics, it may be possible to track compartmental behavior during dialysis.

Future work should integrate optical data with exploratory three-compartment kinetic models to test whether these signals can quantify plasma refill rates, predict tolerance thresholds, or estimate if a patient is approaching “dry weight.” Longitudinal optical monitoring across multiple sessions could then validate whether compartmental signatures consistently predict individual patients’ risk of adverse events. Although exploratory, the three-compartment model represents a promising framework for linking optical biomarkers to clinically actionable fluid management strategies. This approach has the potential to move dialysis monitoring from crude, symptom-based assessments toward quantitative and patient-individualized guidance.

5.4 Overall Conclusion

This body of work has aimed to advance DOS technologies toward the noninvasive monitoring of tissue hydration during hemodialysis. The FD-Bb-NIRS and SWIRS systems discussed hold great potential for real-time assessment of fluid balance, offering information that is difficult to capture with current clinical tools. The systems and findings presented here establish a foundation for detecting water changes in tissue and demonstrate their relevance to patient outcomes. These results provide a first step toward bridging optical measurements with physiological changes during dialysis, and open new avenues for future investigations into more comprehensive, quantitative fluid monitoring.

APPENDIX

Chapter 2 Appendix

Chapter 2 Supplemental Figures:

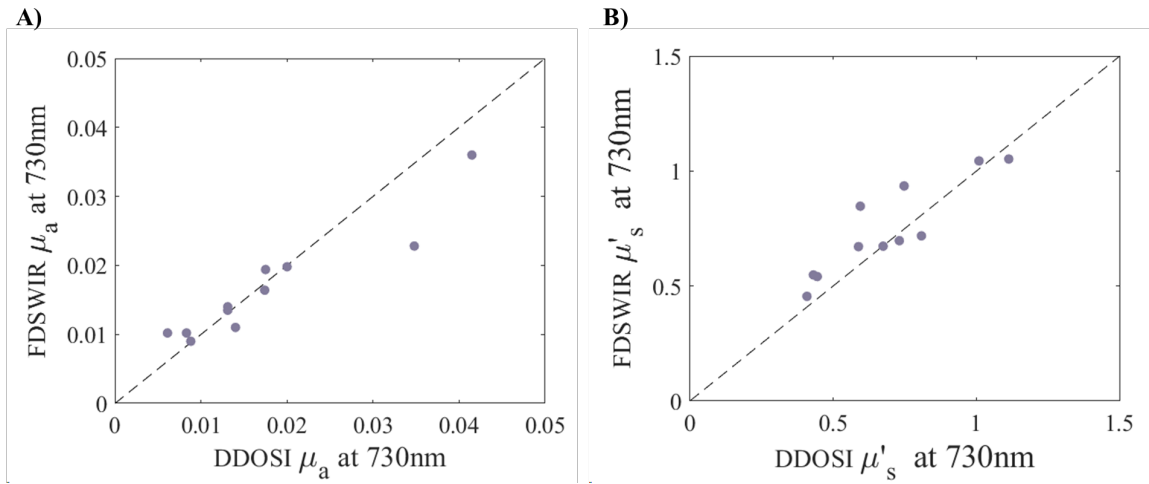


Figure S1 Validation measurements of 11 phantoms taken by the the FD-Bb-NIRS system against a gold standard Network Analyzer (NA). This graph compares A) μ_a and B) μ'_s of both systems at their overlapping wavelength (730 nm). The dashed line represents the identity line. The FD-Bb-NIRS system preformed comparably to the NA system in this validation test.

Chapter 3 Appendix

Chapter 3 Supplemental Figures:

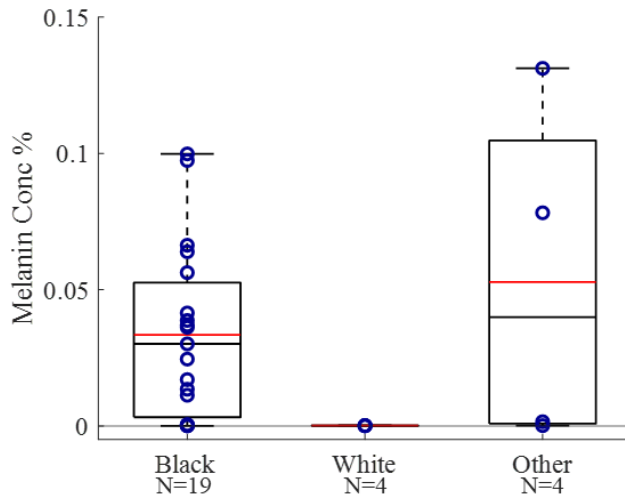


Figure S2 Box plot of [Melanin] across subject's (N=27) self-reported race, stratified by self-identified race into three groups: Black (N=19), White (N=4), and Other (N=4). [Melanin] was derived from baseline measurements taken of pre-dialysis. These findings reflect expected physiological variability in epidermal melanin content across racial groups.

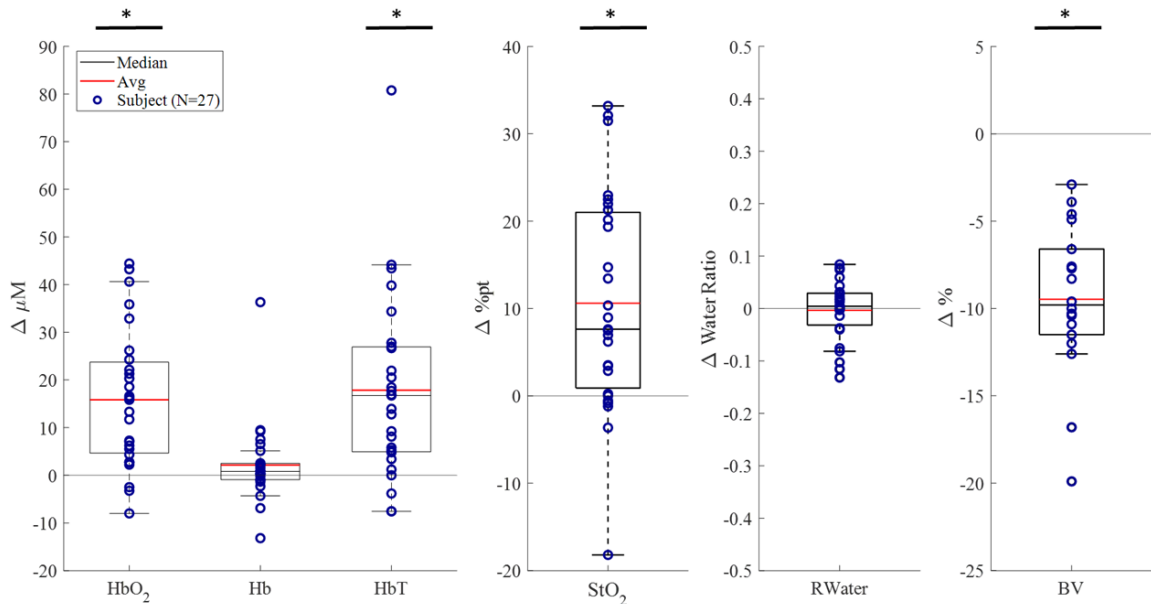


Figure S3 Box plots represent the absolute relative change (Δ) in the measured chromophore derived parameters for each subject (N=27): oxyhemoglobin (HbO₂), deoxyhemoglobin (Hb), total hemoglobin (HbT), tissue oxygen saturation (StO₂), Water Ratio (RWater), and relative

blood volume (BV) derived from crit line (N=19). A one-sample t-test was used to assess whether group means differed significantly from zero ($p < 0.05$). Statistically significant changes were observed in HbO₂, HbT, StO₂, and BV across the cohort.

Table S1 Demographic and treatment characteristics of subjects stratified by occurrence of intradialytic adverse events (N=18 with adverse events, N=9 without). Values are presented as mean \pm standard deviation unless otherwise indicated. Fluid removed represents the average ultrafiltration volume per session. Crit-Line data was available for a subset of participants (N=13 with adverse events, N=6 without) and refers to subjects whose hematocrit was continuously monitored during dialysis via the Fresenius Crit-Line IV Monitor.

	Adverse Events	No Adverse Events
Total	N=18	N=9
Crit-Line	N=13	N=6
Sex		
Male	N=11	N=5
Female	N=7	N=4
Race		
Black	N=12	N=7
White	N=1	N=2
Other	N=4	N=0
Ethnicity		
Hispanic	N=6	N=1
Non-Hispanic	N=12	N=7
Other	N=0	N=1
	Mean \pm Stdev	Mean \pm Stdev
Age	59.7 \pm 14.8 (Y.O)	57.0 \pm 13.7 (Y.O)
Height	1.72 \pm 0.1 (M)	1.68 \pm 0.1 (M)
Weight	78.8 \pm 16 (Kg)	79.0 \pm 15.2 (Kg)
Fluid Removed	1.5 \pm 0.9 (L)	1.7 \pm 0.5 (L)
	Median	Range
Dialysis duration	3	1-3.5 (Hr)
	3	2.25-3.5 (Hr)

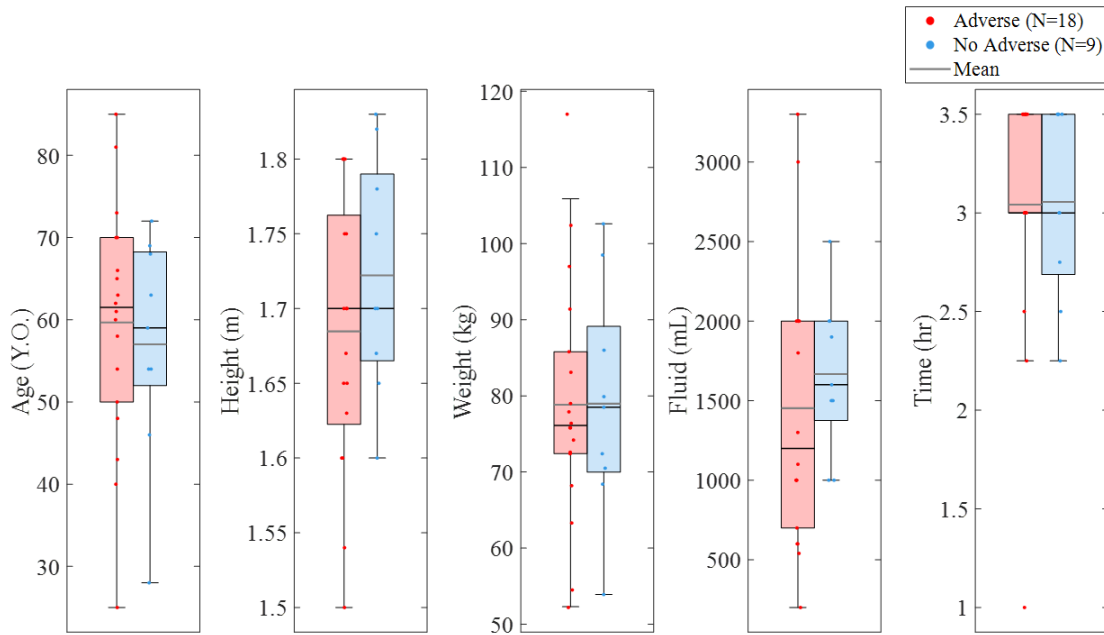


Figure S4 Box plots of the demographic and treatment characteristics are shown for subjects who experienced intradialytic adverse events (red, N=18) and those who did not (blue, N=9). Parameters include age, height, weight, fluid volume removed, and dialysis session duration. There is no statistically significant difference in the characteristics between the two groups.

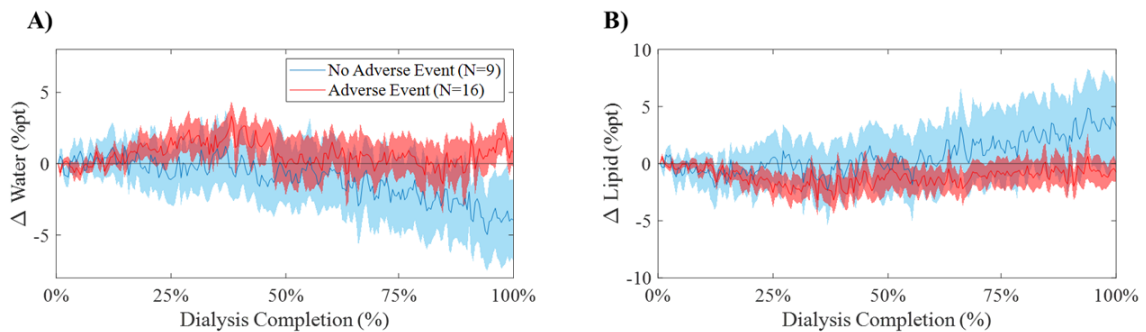


Figure S5 Longitudinal changes of A) $\Delta[\text{Water}]$ (%) and B) $\Delta[\text{Lipid}]$ (%), across subjects with (red, N=16) and without (blue, N=9) adverse events during dialysis. Solid lines represent mean absolute chromophore concentration change; shaded regions represent the standard error. Subjects who experienced adverse events demonstrated a relative increase in [Water] during dialysis, while those without adverse events showed progressive decreases in [Water]. Conversely, likely due to the partial volume effect, [Lipid] tended to decrease in the adverse group and increase slightly in the non-adverse group.

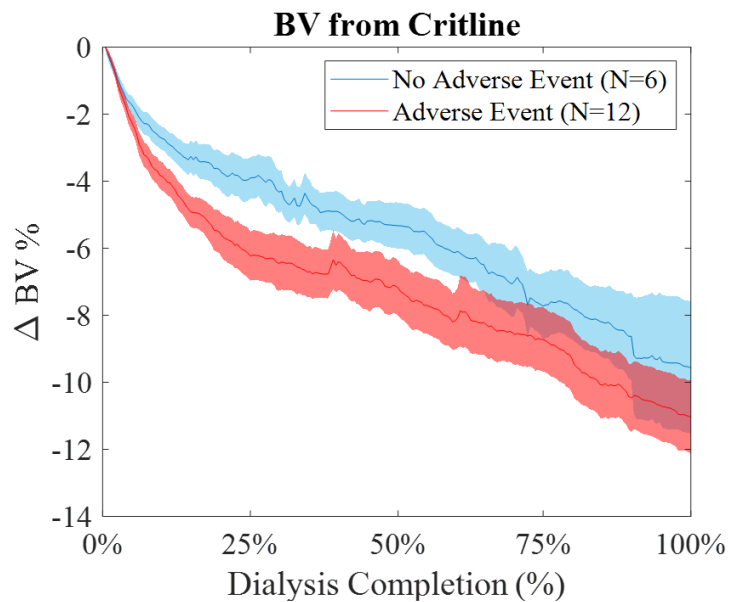


Figure S6 Longitudinal changes in relative blood volume change (Δ BV%) measured by Crit-Line over the course of dialysis for subjects with ($N = 12$, red) and without ($N = 6$, blue) intradialytic adverse events. Solid lines represent mean BV change; shaded regions represent the standard error. One subject was excluded from the analysis due to insufficient data points ($t \leq 114$ min) as described in Chapter 3.3. Δ BV% trends between groups were not statistically different.

Table S2 Comparison of absolute changes (Δ) in optical and clinical parameters between subjects with ($N=18$) and without ($N=9$) intradialytic adverse events. Reported values reflect the mean \pm standard deviation of changes from baseline to end of dialysis treatment for optically measured biomarkers: oxyhemoglobin ($[HbO_2]$), deoxyhemoglobin ($[Hb]$), total hemoglobin ($[HbT]$), tissue oxygen saturation (StO_2), and water ratio. Clinical measurements including relative blood volume (BV) as measured by Crit-Line, and systolic blood pressure (SBP). A two-sided unpaired t-test was performed to assess statistical differences between groups. Of the parameters evaluated, Water Ratio ($p = 0.044$) and SBP ($p = 0.039$) were significantly different between groups, with adverse event subjects exhibiting a relative increase in water ratio and a more pronounced decline in systolic blood pressure.

Δ	Adverse Events		No Adverse Events		P-Value (2-Sided t-test)
	Subjects	Mean \pm Stdev	Subjects	Mean \pm Stdev	
$[HbO_2]$ (μM)	N=18	13.79 ± 16.37	N=9	16.02 ± 11.39	0.718
$[Hb]$ (μM)	N=18	2.06 ± 6.56	N=9	1.01 ± 3.49	0.659

[HbT] (μM)	N=18	15.85 ± 18.00	N=9	17.03 ± 12.55	0.862
StO₂ (% pt)	N=18	10.25 ± 13.20	N=9	9.43 ± 14.52	0.884
Water Ratio	N=18	0.006 ± 0.034	N=9	-0.04 ± 0.085	0.044
SBP (mmHg)	N=18	-12.77 ± 21.94	N=8	5.00 ± 9.41	0.039
BV (%, Crit-Line)	N=13	-10.29 ± 4.89	N=6	-8.65 ± 3.30	0.468

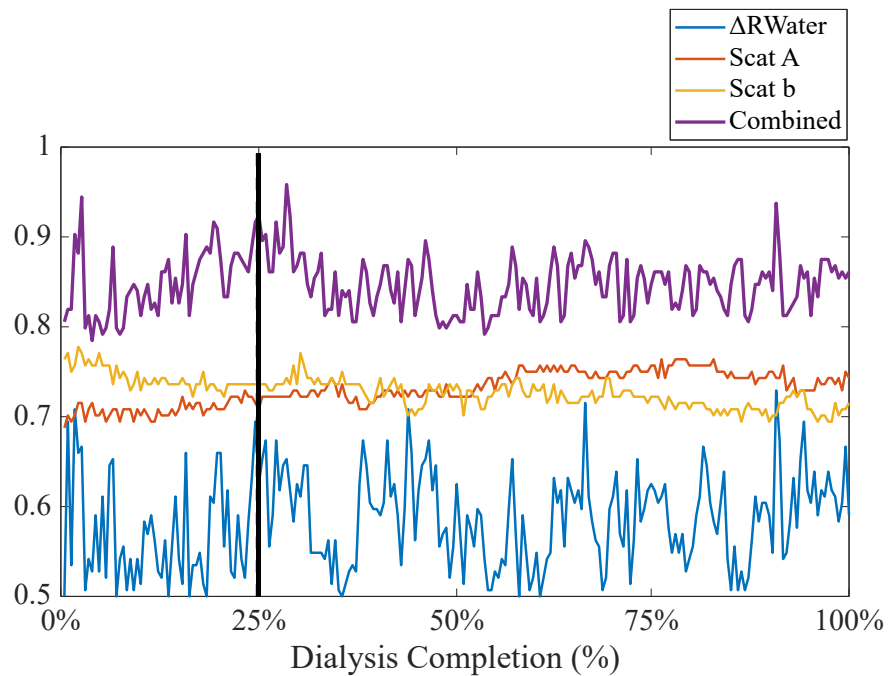


Figure S7 The AUC from the top-performing 3-feature classification models (Δ Water Ratio, A, b) and the combined features over the normalized time course of dialysis completion.

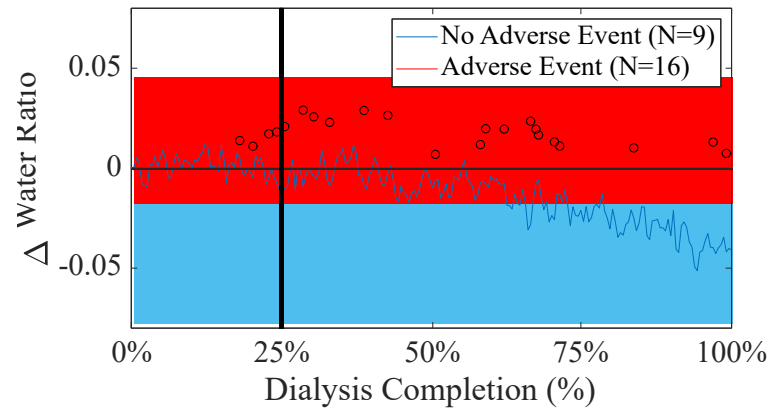


Figure S8 Time-normalized traces (mean \pm standard error) comparing chromophore extractions of subjects with adverse events (red, N=16) and without (blue, N=9) of the Δ Water Ratio (Two subjects with short-duration sessions ($t \leq 114$ min) were excluded from the normalized time trace). The black dots overlay indicate the timestamp of adverse events occurring. The average adverse event occurred at 51.72% \pm 24.84 % of dialysis completion

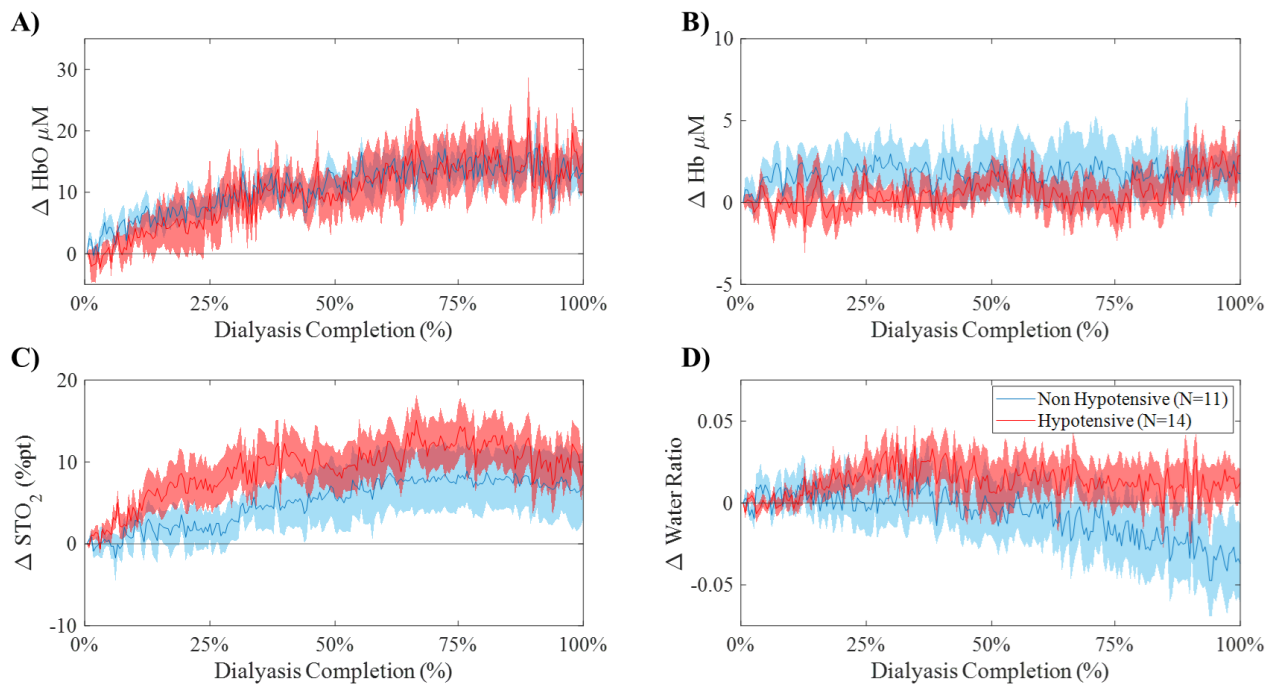


Figure S9 Time-normalized traces (mean \pm standard error) comparing chromophore extractions of subjects with Hypotensive events (red, N=14) and without (blue, N=11) A) Δ [HbO₂] B) Δ [Hb] C) Δ StO₂ D) Δ Water Ratio. Two subjects with short-duration sessions ($t \leq 114$ min) were excluded.

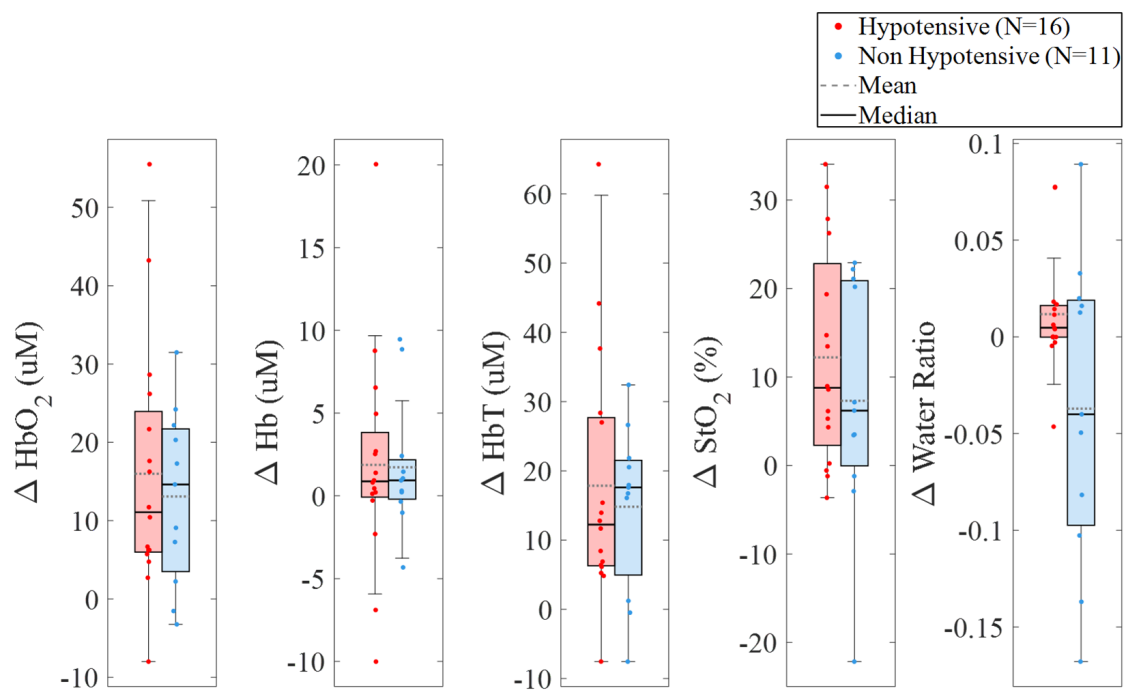


Figure S10 Boxplots of subject values and group means for the absolute Δ [HbO₂], Δ [Hb], Δ [HbT], Δ StO₂, and Δ Water Ratio from the beginning to end of dialysis. Hypotensive subjects are shown in red (N = 16), and non-Hypotensive subjects in blue (N = 11). A significant difference was observed for Δ Water Ratio ($p < 0.05$). No other parameters reached statistical significance.

Chapter 4 Appendix

The sources of tissue chromophore extinction coefficients used in this paper are as follows:

HbO₂ and Hb (430-599 nm): Scott Prohl OMLC [<https://omlc.org/spectra/hemoglobin/>], scaled to match with those at 600 nm. [114]

HbO₂ and Hb (600-1000 nm): Zijlstra et al [“Visible and Near Infrared Absorption Spectra of Human and Animal Haemoglobin determination and application”, First Edition, 2000] and Kou et al [Applied Optics, 1993].

HbO₂ and Hb (1001-2000 nm): Kuenstner and Norris [Journal of Near Infrared Spectroscopy, 1994], scaled to match with those at 1000 nm.

Water (430-559 nm): Pope and Fry et al [Applied Optics, 1997].

Water (600-2000 nm): Seglestein et al [1981]. Values overlap very well with Pope and Frye and no scaling was needed to match the two data sets.

Lipids (430-1098 nm): van Veen and Sterenborg et al [OSA Technical Digest (Optica Publishing Group), 2004].

Lipids (1100-2000 nm): Anderson et al [Lasers Surg. Med., 2006].

Water and Lipids (900-1600 nm): Nachabe et al [JBO, 2010].

Chapter 4 Supplemental Figures:

1. Simulations of extracted optical property uncertainties using FD model

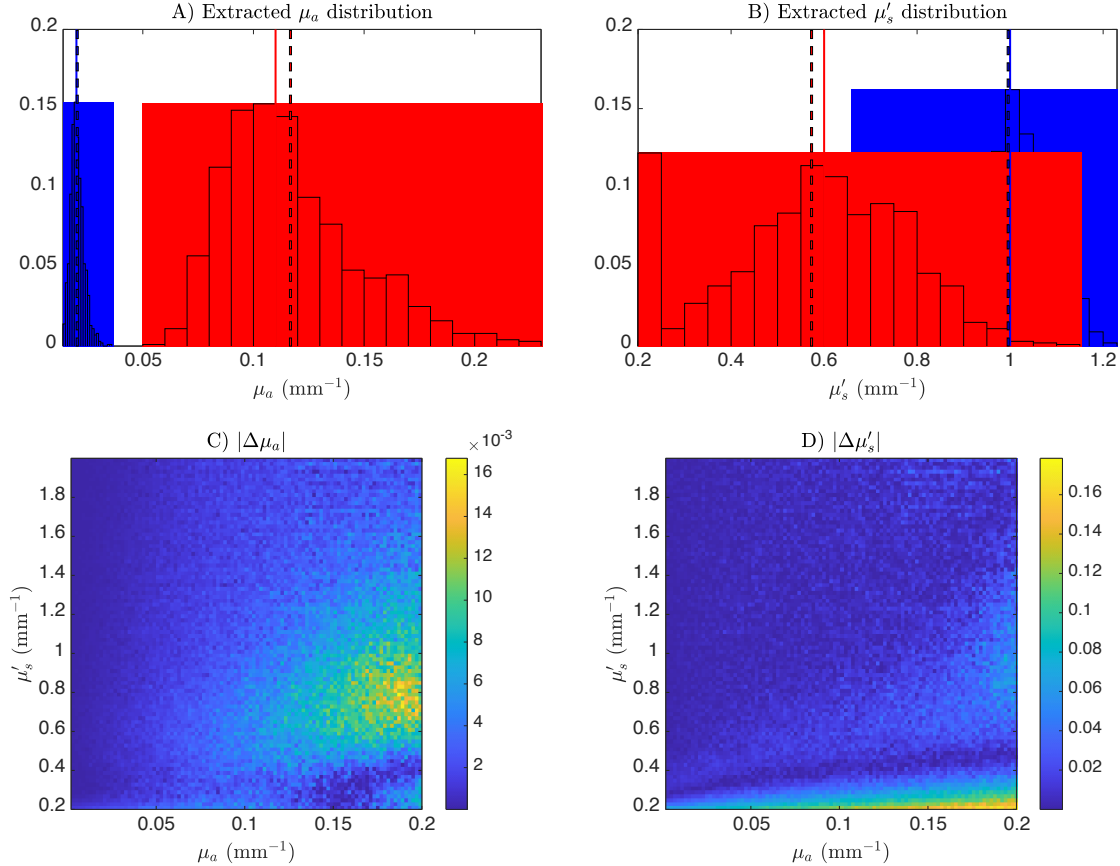


Figure S11 . Examples of extracted absorption (μ_a , panel A) and reduced scattering (μ'_s , panel B) distributions, showing for two sets of optical properties representing values for human muscle tissue at 800 nm ($\mu_a = 0.02 \text{ mm}^{-1}, \mu'_s = 1 \text{ mm}^{-1}$, shown in blue) and 1200 nm ($\mu_a = 0.11 \text{ mm}^{-1}, \mu'_s = 0.6 \text{ mm}^{-1}$, shown in red). Ground truth values are indicated by solid lines, while the distribution mean values are shown in dashed lines. Panels C and D display the absolute differences between the ground truth values and the distribution means across different μ_a and μ'_s values.

2. Ex Vivo Porcine Raw Intensity Measurements

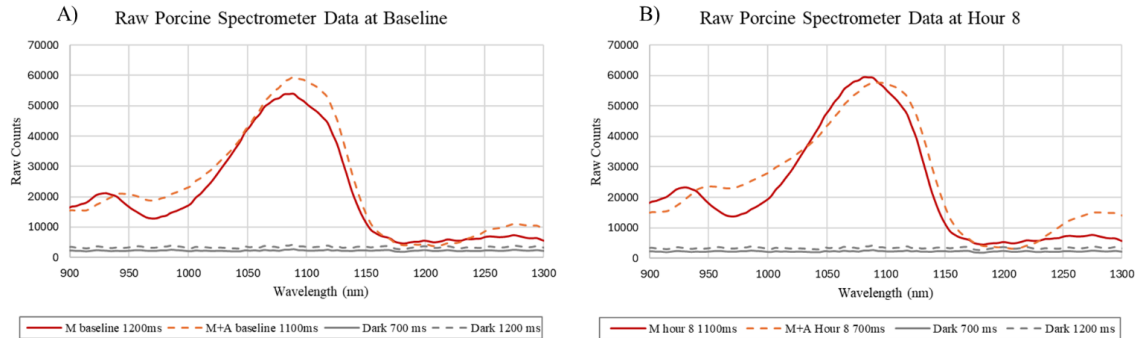


Figure S12 Example raw spectra at A) Baseline and B) Hour 8 for both M and M+A porcine samples as well as dark phantoms at similar integration times. All porcine sample spectrometer counts were several hundred counts above the dark phantom to ensure good SNR.

Throughout the ex vivo porcine desiccation experiment the spectrometer exposure time was adjusted for each measurement to ensure sufficient signal intensity count without saturating the detector. A dark phantom (fabricated with a high nigrosine concentration as an absorbing agent) was also measured using exposure time similar to those used for sample measurements. This allowed us to confirm that the sample measurements had intensity counts well above the dark phantom (dark noise) at all wavelengths. Looking at one of the lowest intensity periods 1200 nm, Baseline measurements: sample M had 1782 counts higher than dark phantom; sample M+A had 765 counts higher than dark phantom at the same integration times. At hour 8 of desiccation, sample M had 1594 counts higher than dark phantom; sample M+A had 1159 counts higher than dark phantom at the same integration times. All samples had counts several hundred counts above dark, indicating measurements were above the noise floor for all spectrometer measurements.

Chapter 5 Appendix

Chapter 5 Supplemental Figures

Bound water refers to water molecules that form hydrogen bonds with non-water molecules, most commonly proteins in biological tissue [59]. When water binds to protein, its vibrational modes are altered (see Chapter 1.1.3). The added molecular interactions cause the vibrational frequency of water to decrease, leading to a red shift of the absorption peaks. In addition, bound water spectra are expected to show peak broadening as well as shifting at ~ 980 and ~ 1200 nm, since each protein has a finite water binding capacity [59]. Given the higher sensitivity of water absorption in the SWIR range, a larger spectral shift was anticipated at 1200 nm compared to 980 nm.

To test this, five gelatin-based phantoms were prepared following Chung et al. [115] and measured with the FD-Bb-SWIRS system. Initial measurements showed on average water absorption peaks near 980 and 1200 nm were red-shifted, with the greater effect occurring at 1200 nm as predicted (Figure S13).

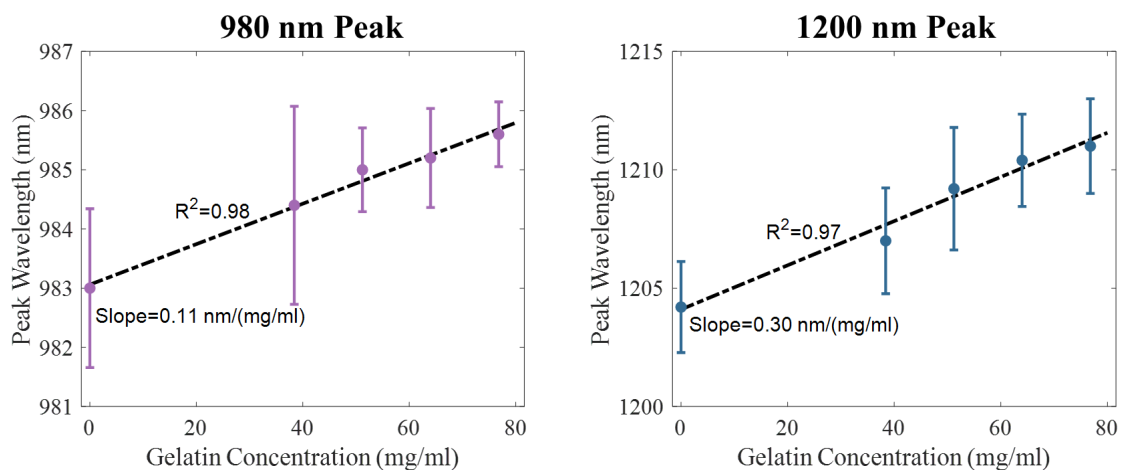


Figure S13 Effect of gelatin concentration on water absorption peak positions. (Left) Peak wavelength near the 980 nm water peak. (Right) Peak wavelength near the 1200 nm water peak. Both peaks experienced red shifts with increasing gelatin concentration, with the 1200 nm peak experiencing a ~3X greater shift than 980 nm. Error bars represent standard deviation across phantoms.

However, because gelatin contains a high collagen fraction, the contribution of collagen absorption was considered. Collagen density was quantified for each phantom, and the collagen spectra were subtracted to isolate water-specific effects. Figure S14 shows the absorption spectrum of collagen between 900 to 1200 nm [116]. Collagen has an absorption peak around 1190 nm and elevated absorption around 980 nm. After correcting for collagen content, the apparent water peak shifts were greatly reduced.

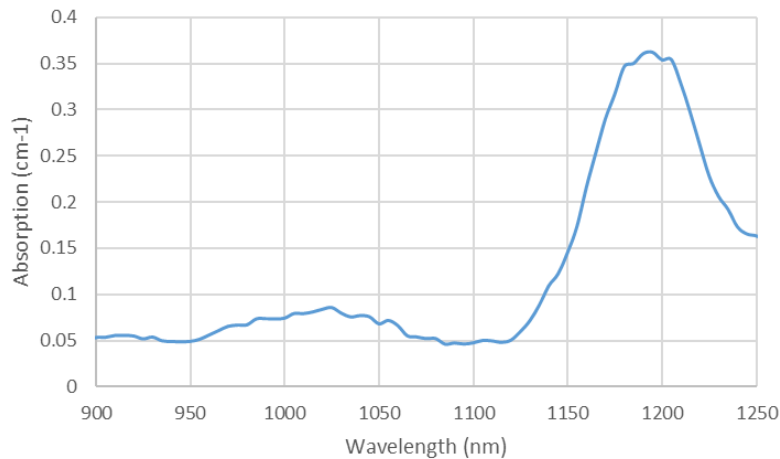


Figure S14 Collagen absorption spectrum from 900–1250 nm. Data is from Sekar et al 2017 [116]. Note the peak near ~1190 to 1200 nm and elevated absorption around 980 to 1000 nm these features greatly overlap with the water absorption peak features at 980 and 1200 nm. (See Figure 14 in chapter 4.1)

Analysis of the CW calibrated spectra provided further insight. When examining local minima around 980 and 1200 nm (Figure S15), minima positions (correlating to peak absorption) were more stable than in the initial FD-Bb-SWIRS results. Across gelatin

phantoms, no measurable shift was observed at 980 nm, while the 1200 nm peak shifted only \sim 4 nm between 0 and 24 g collagen.

Overall, these findings make it unclear whether the initially observed red shifts (Figure S13) reflect true bound water effects, or whether they are largely driven by the collagen contents within the gelatin phantoms.

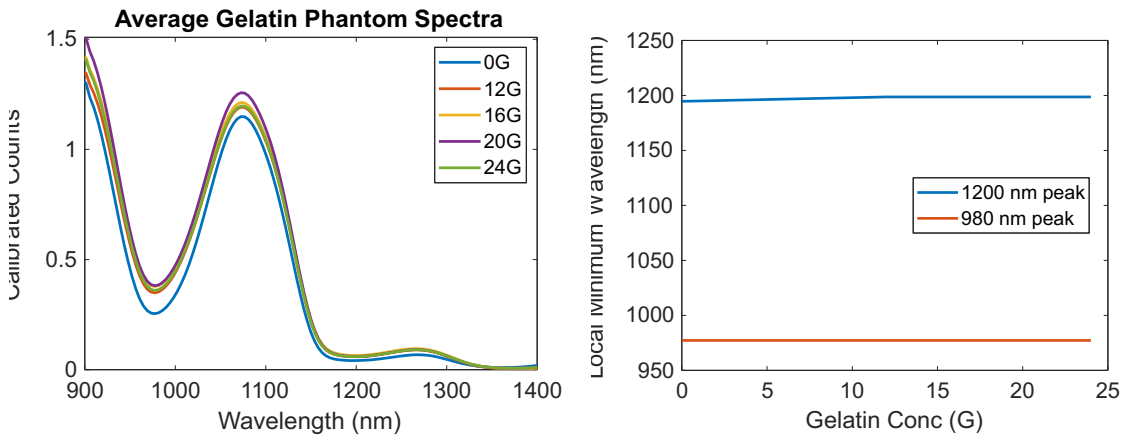


Figure S15 (Left) The average calibrated CW spectra of gelatin phantoms at varying collagen concentrations (0–24 g). **(Right)** The corresponding local minima at \sim 980 nm and \sim 1200 nm.

BIBLIOGRAPHY

- [1] R. Saran et al., “US Renal Data System 2019 Annual Data Report: Epidemiology of Kidney Disease in the United States,” *American Journal of Kidney Diseases*, vol. 75, no. 1. 2020. doi: 10.1053/j.ajkd.2019.09.003.
- [2] J. Himmelfarb, “Haemodialysis review article,” *N Engl J Med*, vol. 311, no. 3, 2010.
- [3] U.S Department of Health and Human Services, “Annual data report,” National Institute of Diabetes and Digestive and Kidney Diseases, <https://usrds-adr.niddk.nih.gov/2020/end-stage-renal-disease/1-incidence-prevalence-patient-characteristics-and-treatment-modalities> (accessed Sep. 3, 2025).
- [4] Centers for Disease Control and Prevention, “Underlying Cause of Death 1999-2019,” *CDC WONDER Online Database*, 2019.
- [5] Centers for Disease Control and Prevention, “Chronic Kidney Disease in the United States, 2021,” *Cdc*, vol. 1, 2021.
- [6] R. Agarwal, “Hypervolemia is associated with increased mortality among hemodialysis patients,” *Hypertension*, vol. 56, no. 3, 2010, doi: 10.1161/HYPERTENSIONAHA.110.154815.
- [7] R. O. Mathew et al., “Diagnosis and management of atherosclerotic cardiovascular disease in chronic kidney disease: a review,” *Kidney International*, vol. 91, no. 4. 2017. doi: 10.1016/j.kint.2016.09.049.
- [8] Okafor, UH , Uzoh . R, and Edeh. SO, “Premature termination of haemodialysis (PTHD) sessions in a tertiary hospital in Nigeria: Prevalence and causes,” *International Journal of Nephrology and Kidney Failure*, vol. 6, no. 4, 2020. doi:10.16966/2380-5498.201
- [9] Y. C. Tsai et al., “Association of fluid overload with cardiovascular morbidity and all-cause mortality in stages 4 and 5 CKD,” *Clinical Journal of the American Society of Nephrology*, vol. 10, no. 1, 2015, doi: 10.2215/CJN.03610414.
- [10] Kuipers J, Oosterhuis JK, Krijnen WP, Dasselaar JJ, Gaillard CA, Westerhuis R, Franssen CF. Prevalence of intradialytic hypotension, clinical symptoms and nursing interventions--a three-months, prospective study of 3818 haemodialysis sessions. *BMC Nephrol*. 2016 Feb 27;17:21. doi: 10.1186/s12882-016-0231-9.
- [11] Charra B et al., Clinical assessment of dry weight. *Nephrol Dial Transplant*. 1996.
- [12] A. D. Sinha, “Why assistive technology is needed for probing of dry weight,” in *Blood Purification*, 2011, vol. 31, no. 1–3. doi: 10.1159/000321840.

- [13] Kuipers, J., Oosterhuis, J.K., Krijnen, W.P. et al. Prevalence of intradialytic hypotension, clinical symptoms and nursing interventions - a three-months, prospective study of 3818 haemodialysis sessions. *BMC Nephrol* 17, 21 (2016). <https://doi.org/10.1186/s12882-016-0231-9>
- [14] Mehmet Kanbay, Lale A Ertuglu, Baris Afsar, Elif Ozdogan, Dimitrie Siriopol, Adrian Covic, Carlo Basile, Alberto Ortiz, An update review of intradialytic hypotension: concept, risk factors, clinical implications and management, *Clinical Kidney Journal*, Volume 13, Issue 6, December 2020, Pages 981–993, <https://doi.org/10.1093/ckj/sfaa078>
- [15] Hamrahan SM, Vilayet S, Herberth J, Fülop T. Prevention of Intradialytic Hypotension in Hemodialysis Patients: Current Challenges and Future Prospects. *Int J Nephrol Renovasc Dis.* 2023 Aug 1;16:173-181. doi: 10.2147/IJNRD.S245621. PMID: 37547077; PMCID: PMC10404053.
- [16] S. Dheenan and W. L. Henrich, “Preventing dialysis hypotension: A comparison of usual protective maneuvers,” *Kidney Int*, vol. 59, no. 3, 2001, doi: 10.1046/j.1523-1755.2001.0590031175.x.
- [17] S. McGee, W. B. Abernethy, and D. L. Simel, “Is this patient hypovolemic?,” *JAMA*, vol. 281, no. 11, 1999, doi: 10.1001/jama.281.11.1022.
- [18] C. Zoccali et al., “Chronic fluid overload and mortality in ESRD,” *Journal of the American Society of Nephrology*, vol. 28, no. 8, 2017, doi: 10.1681/ASN.2016121341.
- [19] Nesbitt. H, “Kidney health initiative (KHI): Fostering Innovation in fluid management,” *Kidney Health Initiative*, <https://khi.asn-online.org/pages/?ID=12#:~:text=Abstract,cramps%20and%20fatigue%20often%20occur>.
- [20] Chou JA, Kalantar-Zadeh K. Volume Balance and Intradialytic Ultrafiltration Rate in the Hemodialysis Patient. *Curr Heart Fail Rep.* 2017 Oct;14(5):421-427. doi: 10.1007/s11897-017-0356-6. PMID: 28803369; PMCID: PMC5693775.
- [21] T. Durduran, R. Choe, W. B. Baker, and A. G. Yodh, “Diffuse optics for tissue monitoring and tomography,” *Reports on Progress in Physics*, vol. 73, no. 7, p. 076701, Jul. 2010, doi: 10.1088/0034-4885/73/7/076701.
- [22] W. G. Zijlstra, A. Buursma, and O. W. van Assendelft, *Visible and Near Infrared Absorption Spectra of Human and Animal Haemoglobin*. London: CRC Press, 2021. [doi: 10.1201/9780429071096].

[23] Segelstein, DJ, "The complex refractive index of water" M.S thesis, Physics. University of Missouri-Kansas City. 1981. Available: <https://mospace.umsystem.edu/xmlui/handle/10355/11599>

[24] van Veen RL, Sterenborg HJ, Pifferi A, Torricelli A, Chikoidze E, Cubeddu R. Determination of visible near-IR absorption coefficients of mammalian fat using time- and spatially resolved diffuse reflectance and transmission spectroscopy. *J Biomed Opt.* 2005 Sep-Oct;10(5):054004. doi: 10.1117/1.2085149.

[25] Nachabé R, Hendriks BH, Desjardins AE, van der Voort M, van der Mark MB, Sterenborg HJ. Estimation of lipid and water concentrations in scattering media with diffuse optical spectroscopy from 900 to 1,600 nm. *J Biomed Opt.* 2010 May-Jun;15(3):037015. doi: 10.1117/1.3454392.

[26] S. Jacques and S. Prahl, "Extinction coefficient of melanin: Oregon Medical Laser Center," <https://omlc.org/spectra/melanin/extcoeff.html>

[27] M. B. Applegate, R. E. Istfan, S. Spink, A. Tank, and D. Roblyer, "Recent advances in high speed diffuse optical imaging in biomedicine," *APL Photonics*, vol. 5, no. 4, Apr. 2020, doi: 10.1063/1.5139647.

[28] F. Scholkmann et al., "A review on continuous wave functional near-infrared spectroscopy and imaging instrumentation and methodology," *Neuroimage*, vol. 85, pp. 6–27, Jan. 2014, doi: 10.1016/j.neuroimage.2013.05.004.

[29] Antonio Pifferi, Davide Contini, Alberto Dalla Mora, Andrea Farina, Lorenzo Spinelli, Alessandro Torricelli, "New frontiers in time-domain diffuse optics, a review," *J. Biomed. Opt.* 21(9) 091310 (17 June 2016) <https://doi.org/10.1117/1.JBO.21.9.091310>

[30] Cuccia DJ, Bevilacqua F, Durkin AJ, Ayers FR, Tromberg BJ. Quantitation and mapping of tissue optical properties using modulated imaging. *J Biomed Opt.* 2009 Mar-Apr;14(2):024012. doi: 10.1117/1.3088140. PMID: 19405742; PMCID: PMC2868524.

[31] R. Tao, J. Gröhl, L. Hacker, A. Pifferi, D. Roblyer, and S. E. Bohndiek, "Tutorial on methods for estimation of optical absorption and scattering properties of tissue," *J Biomed Opt.* vol. 29, no. 06, Jun. 2024, doi: 10.1117/1.JBO.29.6.060801.

[32] S. Fantini and A. Sassaroli, "Frequency-Domain Techniques for Cerebral and Functional Near-Infrared Spectroscopy," *Front Neurosci.* vol. 14, Apr. 2020, doi: 10.3389/fnins.2020.00300.

[33] A. Sassaroli and S. Fantini, “Comment on the modified Beer–Lambert law for scattering media,” *Phys. Med. Biol.* 49(14), N255–N257 (2004).
<https://doi.org/10.1088/0031-9155/49/14/N07>

[34] Fantini S, Hueber D, Franceschini MA, Gratton E, Rosenfeld W, Stubblefield PG, Maulik D, Stankovic MR. Non-invasive optical monitoring of the newborn piglet brain using continuous-wave and frequency-domain spectroscopy. *Phys Med Biol.* 1999 Jun;44(6):1543-63. doi: 10.1088/0031-9155/44/6/308. PMID: 10498522.

[35] Tobias JD, Johnson GA, Rehman S, Fisher R, Caron N. Cerebral oxygenation monitoring using near infrared spectroscopy during one-lung ventilation in adults. *J Minim Access Surg.* 2008 Oct;4(4):104-7. doi: 10.4103/0972-9941.45206. PMID: 19547695; PMCID: PMC2699221.

[36] A. Tank et al., “Diffuse optical spectroscopic imaging reveals distinct early breast tumor hemodynamic responses to metronomic and maximum tolerated dose regimens,” *Breast Cancer Research*, vol. 22, no. 1, p. 29, Dec. 2020, doi: 10.1186/s13058-020-01262-1.

[37] F. Bevilacqua, A. J. Berger, A. E. Cerussi, D. Jakubowski, and B. J. Tromberg, “Broadband absorption spectroscopy in turbid media by combined frequency-domain and steady-state methods,” *Appl Opt.*, vol. 39, no. 34, pp. 6498–6507, 2000, doi: 10.1364/AO.39.006498.

[38] De Blasi RA, Luciani R, Punzo G, Arcioni R, Romano R, Boezi M, Menè P. Microcirculatory changes and skeletal muscle oxygenation measured at rest by non-infrared spectroscopy in patients with and without diabetes undergoing haemodialysis. *Crit Care.* 2009;13 Suppl 5(Suppl 5):S9. doi: 10.1186/cc8007.

[39] Tank, A., Peterson, H.M., Pera, V. et al. Diffuse optical spectroscopic imaging reveals distinct early breast tumor hemodynamic responses to metronomic and maximum tolerated dose regimens. *Breast Cancer Res* 22, 29 (2020).
<https://doi.org/10.1186/s13058-020-01262-1>

[40] Shigeto Ueda, Darren Roblyer, Albert Cerussi, Amanda Durkin, Anais Leproux, Ylenia Santoro, Shanshan Xu, Thomas D. O'Sullivan, David Hsiang, Rita Mehta, John Butler, Bruce J. Tromberg; Baseline Tumor Oxygen Saturation Correlates with a Pathologic Complete Response in Breast Cancer Patients Undergoing Neoadjuvant Chemotherapy. *Cancer Res* 1 September 2012; 72 (17): 4318–4328.
<https://doi.org/10.1158/0008-5472.CAN-12-0056>

[41] O'Sullivan, T.D., Leproux, A., Chen, JH. et al. Optical imaging correlates with magnetic resonance imaging breast density and reveals composition changes during neoadjuvant chemotherapy. *Breast Cancer Res* 15, R14 (2013).
<https://doi.org/10.1186/bcr3389>

[42] Samuel S. Spink, Fei Teng, Vivian Pera, Hannah M. Peterson, Tim Cormier, Alexis Sauer-Budge, David A. Chargin, Sam Brookfield, Adam T. Eggebrecht, Naomi Yu Ko, Darren M. Roblyer, "High optode-density wearable diffuse optical probe for monitoring paced breathing hemodynamics in breast tissue," *J. Biomed. Opt.* 26(6) 062708 (2 June 2021)

[43] Bruce J. Tromberg, Zheng Zhang, Anaïs Leproux, Thomas D. O'Sullivan, Albert E. Cerussi, Philip M. Carpenter, Rita S. Mehta, Darren Roblyer, Wei Yang, Keith D. Paulsen, Brian W. Pogue, Shudong Jiang, Peter A. Kaufman, Arjun G. Yodh, So Hyun Chung, Mitchell Schnall, Bradley S. Snyder, Nola Hylton, David A. Boas, Stefan A. Carp, Steven J. Isakoff, David Mankoff; on behalf of the ACRIN 6691 investigators, Predicting Responses to Neoadjuvant Chemotherapy in Breast Cancer: ACRIN 6691 Trial of Diffuse Optical Spectroscopic Imaging. *Cancer Res* 15 October 2016; 76 (20): 5933–5944

[44] R. Nachabé, B. H. W. Hendriks, A. E. Desjardins, M. van der Voort, M. B. van der Mark, and H. J. C. M. Sterenborg, "Estimation of lipid and water concentrations in scattering media with diffuse optical spectroscopy from 900 to 1600 nm," *J Biomed Opt.* vol. 15, no. 3, p. 037015, 2010, doi: 10.1117/1.3454392.

[45] J. H. Lam, K. J. Tu, and S. Kim, "Narrowband diffuse reflectance spectroscopy in the 900–1000 nm wavelength region to quantify water and lipid content of turbid media," *Biomed Opt Express*, vol. 12, no. 6, p. 3091, Jun. 2021, doi: 10.1364/BOE.425451.

[46] S. S. Spink et al., "Shortwave infrared diffuse optical wearable probe for quantification of water and lipid content in emulsion phantoms using deep learning," *J Biomed Opt.* vol. 28, no. 09, Jun. 2023, doi: 10.1117/1.JBO.28.9.094808.

[47] Y. Zhao et al., "Shortwave-infrared meso-patterned imaging enables label-free mapping of tissue water and lipid content," *Nat Commun*, vol. 11, no. 1, p. 5355, Oct. 2020, doi: 10.1038/s41467-020-19128-7.

[48] L. A. Colucci et al., "Fluid assessment in dialysis patients by point-of-care magnetic relaxometry," *Sci Transl Med*, vol. 11, no. 502, 2019, doi: 10.1126/scitranslmed.aau1749.

[49] Campos I, Chan L, Zhang H, Deziel S, Vaughn C, Meyring-Wösten A, Kotanko P. Intradialytic Hypoxemia in Chronic Hemodialysis Patients. *Blood Purif.* 2016;41(1-3):177-87. doi: 10.1159/000441271.

[50] Pierro ML, Kainerstorfer JM, Civiletto A, Weiner DE, Sassaroli A, Hallacoglu B, Fantini S. Reduced speed of microvascular blood flow in hemodialysis patients versus healthy controls: a coherent hemodynamics spectroscopy study. *J Biomed Opt.* 2014 Feb;19(2):026005. doi: 10.1117/1.JBO.19.2.026005. PMID: 24522805; PMCID: PMC3922146.

[51] Thao Pham, Giles Blaney, Angelo Sassaroli, Cristianne Fernandez, Arushi Agarwal, Daniel Weiner, Sergio Fantini, "Blood-pressure-induced oscillations of cerebral hemodynamics during hemodialysis," *Proc. SPIE 11629, Optical Techniques in Neurosurgery, Neurophotonics, and Optogenetics, 1162922* (9 March 2021); <https://doi.org/10.1117/12.2577674>

[52] G. M. Hale and M. R. Querry, "Optical Constants of Water in the 200-nm to 200- μ m Wavelength Region," *Appl Opt*, vol. 12, no. 3, 1973, doi: 10.1364/ao.12.000555.

[53] M. Stomp, J. Huisman, L. J. Stal, and H. C. P. Matthijs, "Colorful niches of phototrophic microorganisms shaped by vibrations of the water molecule," *ISME Journal*, vol. 1, no. 4. 2007. doi: 10.1038/ismej.2007.59.

[54] S. T. van der Post et al., "Strong frequency dependence of vibrational relaxation in bulk and surface water reveals sub-picosecond structural heterogeneity," *Nat Commun*, vol. 6, 2015, doi: 10.1038/ncomms9384.

[55] H. Buiteveld, J. H. M. Hakvoort, and M. Donze, "Optical properties of pure water" in *Ocean Optics XII*, 1994, vol. 2258. doi: 10.1117/12.190060.

[56] K. Buijs and G. R. Coppin, "Near-infrared studies of the structure of water. I. Pure water," *J Chem Phys*, vol. 39, no. 8, 1963, doi: 10.1063/1.1734579.

[57] L. Kou, D. Labrie, and P. Chylek, "Refractive indices of water and ice in the 0.65- to 2.5- μ m spectral range," *Appl. Opt.* 32, 3531-3540 ,1993, doi: 10.1364/AO.32.003531

[58] J. Kim, J. Y. Lee, S. Lee, B. J. Mhin, and K. S. Kim, "Harmonic vibrational frequencies of the water monomer and dimer: Comparison of various levels of ab initio theory," *J Chem Phys*, vol. 102, no. 1, 1995, doi: 10.1063/1.469404.

[59] J. P. C. M. Peters, F. J. Vergeldt, R. M. Boom, and A. J. van der Goot, "Water-binding capacity of protein-rich particles and their pellets," *Food Hydrocoll*, vol. 65, 2017, doi: 10.1016/j.foodhyd.2016.11.015.

[60] A. Torjesen, R. Istfan, and D. Roblyer, "Ultrafast wavelength multiplexed broad bandwidth digital diffuse optical spectroscopy for in vivo extraction of tissue optical properties," *J Biomed Opt*, vol. 22, no. 3, p. 036009, Mar. 2017,doi: 10.1117/1.JBO.22.3.036009.

- [61] R. Istfan, C. A. Gómez, M. Applegate, D. Rozenberg, W. D. Reid, and D. Roblyer, “Hemodynamics of the sternocleidomastoid measured with frequency domain near-infrared spectroscopy towards non-invasive monitoring during mechanical ventilation,” *Biomed Opt Express*, vol. 12, no. 7, p. 4147, Jul. 2021, doi: 10.1364/BOE.430423.
- [62] Suciu D, Pham T, Wei LL, Guruprasad S, Roblyer D. Frequency domain broadband short-wave infrared spectroscopy for measurement of tissue optical properties from 685 to 1300 nm. *J Biomed Opt*. 2025 Apr;30(4):045001. doi: 10.1117/1.JBO.30.4.045001.
- [63] C. A. Gómez, L. Brochard, E. C. Goligher, D. Rozenberg, W. D. Reid, and D. Roblyer, “Combined frequency domain near-infrared spectroscopy and diffuse correlation spectroscopy system for comprehensive metabolic monitoring of inspiratory muscles during loading,” *J Biomed Opt*, vol. 29, no. 03, Mar. 2024, doi: 10.1117/1.JBO.29.3.035002.
- [64] A. N. Bashkatov et al., “Optical properties of human skin, subcutaneous and mucous tissues in the wavelength range from 400 to 2000 nm,” *J. Phys. D Appl. Phys.*, 38 (15), 2543 –2555 <https://doi.org/10.1088/0022-3727/38/15/004> (2005). Google Scholar
- [65] R. L. Harrison, “Introduction to Monte Carlo simulation,” in *AIP Conference Proceedings*, 2009, vol. 1204. doi: 10.1063/1.3295638.
- [66] S. L. Jacques and L. Wang, “Monte Carlo Modeling of Light Transport in Tissues,” in *Optical-Thermal Response of Laser-Irradiated Tissue*, 1995. doi: 10.1007/978-1-4757-6092-7_4.
- [67] Q. Fang and D. A. Boas, “Monte Carlo Simulation of Photon Migration in 3D Turbid Media Accelerated by Graphics Processing Units,” *Opt Express*, vol. 17, no. 22, 2009, doi: 10.1364/oe.17.020178.
- [68] D. Bregman H, *Handbook of Dialysis*. New York: Dauugirdas JT IT, 1994.
- [69] S. Ishibe and A. J. Peixoto, “Methods of assessment of volume status and intercompartmental fluid shifts in hemodialysis patients: Implications in clinical practice,” *Seminars in Dialysis*, vol. 17, no. 1. 2004. doi: 10.1111/j.1525-139X.2004.17112.x.
- [70] C. Crepaldi, S. Soni, C. Y. Chionh, P. Wabel, D. N. Cruz, and C. Ronco, “Application of body composition monitoring to peritoneal dialysis patients.,” *Contrib Nephrol*, vol. 163, 2009, doi: 10.1159/000223772.

[71] Balter P, Artemyev M, Zabetakis P. Methods and challenges for the practical application of Crit-Line™ monitor utilization in patients on hemodialysis. *Blood Purif.* 2015;39(1-3):21-4. doi: 10.1159/000368936. Epub 2015 Jan 20. PMID: 25660221.

[72] R. T. Gansevoort et al., “Chronic kidney disease and cardiovascular risk: Epidemiology, mechanisms, and prevention,” *The Lancet*, vol. 382, no. 9889. 2013. doi: 10.1016/S0140-6736(13)60595-4.

[73] P. Wabel, P. Chamney, U. Moissl, and T. Jirka, “Importance of whole-body bioimpedance spectroscopy for the management of fluid balance,” in *Blood Purification*, 2009, vol. 27, no. 1. doi: 10.1159/000167013.

[74] National Kidney Foundation. Page Title: “KDOQI Clinical Practice Guidelines for Cardiovascular Disease in Dialysis Patients”. Website Title: “NKF KDOQI GUIDELINES”. Available: https://kidneyfoundation.cachefly.net/professionals/KDOQI/guidelines_cvd/intradialytic.htm

[75] Blaney G, Curtsmith P, Sassaroli A, Fernandez C, Fantini S. Broadband absorption spectroscopy of heterogeneous biological tissue. *Appl Opt.* 2021 Sep 1;60(25):7552-7562. doi: 10.1364/AO.431013. PMID: 34613221; PMCID: PMC11407782.

[76] I. W. Selesnick, H. L. Graber, Y. Ding, T. Zhang and R. L. Barbour, "Transient Artifact Reduction Algorithm (TARA) Based on Sparse Optimization," in *IEEE Transactions on Signal Processing*, vol. 62, no. 24, pp. 6596-6611, Dec.15, 2014, doi: 10.1109/TSP.2014.2366716.

[77] S. L. Jacques, “Optical properties of biological tissues: a review,” *Phys Med Biol.*, vol. 58, no. 11, pp. R37–R61, Jun. 2013, doi: 10.1088/0031-9155/58/11/R37.

[78] Tobias A, Ballard BD, Mohiuddin SS. Physiology, Water Balance. [Updated 2022 Oct 3]. In: StatPearls [Internet]. Treasure Island (FL): StatPearls Publishing; 2025 Jan-. Available from: <https://www.ncbi.nlm.nih.gov/books/NBK541059/>

[79] Flythe JE, Kimmel SE, Brunelli SM. Rapid fluid removal during dialysis is associated with cardiovascular morbidity and mortality. *Kidney Int.* 2011 Jan;79(2):250-7. doi: 10.1038/ki.2010.383. Epub 2010 Oct 6. PMID: 20927040; PMCID: PMC3091945.

[80] A. Pilvar, J. Plutzky, M. C. Pierce, and D. Roblyer, “Shortwave infrared spatial frequency domain imaging for non-invasive measurement of tissue and blood optical properties,” *J Biomed Opt*, vol. 27, no. 06, Jun. 2022, doi: 10.1117/1.JBO.27.6.066003.

- [81] S. Tabassum, V. Pera, G. Greening, T. J. Muldoon, and D. Roblyer, “Two-layer inverse model for improved longitudinal preclinical tumor imaging in the spatial frequency domain,” *J Biomed Opt*, vol. 23, no. 07, p. 1, Jul. 2018, doi: 10.1117/1.JBO.23.7.076011.
- [82] T. J. Allen, A. Hall, A. P. Dhillon, J. S. Owen, and P. C. Beard, “Spectroscopic photoacoustic imaging of lipid-rich plaques in the human aorta in the 740 to 1400 nm wavelength range,” *J Biomed Opt*, vol. 17, no. 6, 2012, doi: 10.1117/1.JBO.17.6.061209.
- [83] Z. Abassi, E. E. Khoury, T. Karram, and D. Aronson, “Edema formation in congestive heart failure and the underlying mechanisms,” *Front Cardiovasc Med*, vol. 9, Sep. 2022, doi: 10.3389/fcvm.2022.933215.
- [84] S. Shenoy, S. Shrivastava, J. Sandhu, B. Malhotra, and S. Gupta, “Development and Validation of a Skin Fold Thickness Prediction Equation for Asian Indians Using Hydrodensitometry,” *J Obes Overweight*, vol. 2, no. 1, Feb. 2016, doi: 10.15744/2455-7633.2.102.
- [85] G. Ganesan et al., “Diffuse optical spectroscopic imaging of subcutaneous adipose tissue metabolic changes during weight loss,” *Int J Obes*, vol. 40, no. 8, pp. 1292–1300, Aug. 2016, doi: 10.1038/ijo.2016.43.
- [86] S. Vasudevan et al., “Method for quantitative broadband diffuse optical spectroscopy of tumor-like inclusions,” *Appl. Sci.*, 10 (4), 1419 <https://doi.org/10.3390/app10041419> (2020).
- [87] Q. Zhu and S. Poplack, “A review of optical breast imaging: multi-modality systems for breast cancer diagnosis,” *Eur. J. Radiol.*, 129 109067 <https://doi.org/10.1016/j.ejrad.2020.109067> EJRADR 0720-048X (2020).
- [88] L. E. Armstrong, “Assessing hydration status: the elusive gold standard,” *J. Am. Coll. Nutr.*, 26 575S –584S <https://doi.org/10.1080/07315724.2007.10719661> JONUDL 0731-5724 (2007).
- [89] I. Çilesiz and A. J. Welch, “Light dosimetry: effects of dehydration and thermal damage on the optical properties of the human aorta,” *Appl. Opt.*, 33 (16), 3571 <https://doi.org/10.1364/AO.33.003571> APOPAI 0003-6935 (1994).
- [90] R. V. Warren et al., “Diffuse optical spectroscopic method for tissue and body composition assessment,” *J. Biomed. Opt.*, 27 (6), 065002 <https://doi.org/10.1117/1.JBO.27.6.065002> JBOPFO 1083-3668 (2022).

[91] R. H. Wilson et al., “Quantitative short-wave infrared multispectral imaging of in vivo tissue optical properties,” *J. Biomed. Opt.*, 19 (8), 086011 <https://doi.org/10.1117/1.jbo.19.8.086011> JBOPFO 1083-3668 (2014).

[92] X. Zhou et al., “Review of recent advances in frequency-domain near-infrared spectroscopy technologies,” *Biomed. Opt. Express*, 14 (7), 3234 <https://doi.org/10.1364/boe.484044> BOEICL 2156-7085 (2023).

[93] A. Cerussi et al., “Predicting response to breast cancer neoadjuvant chemotherapy using diffuse optical spectroscopy,” *Proc. Natl. Acad. Sci. U. S. A.*, 104 (10), 4014 – 4019 <https://doi.org/10.1073/pnas.0611058104> (2007). Google Scholar

[94] V. Damagatla et al., “Use of bioresorbable fibers for short-wave infrared spectroscopy using time-domain diffuse optics,” *Biomed. Opt. Express*, 15 (9), 5041 <https://doi.org/10.1364/BOE.531681> BOEICL 2156-7085 (2024).

[95] A. Pilvar et al., “Shortwave infrared spatial frequency domain imaging for non-invasive measurement of tissue and blood optical properties,” *J. Biomed. Opt.*, 27 (6), 066003 <https://doi.org/10.1117/1.JBO.27.6.066003> JBOPFO 1083-3668 (2022).

[96] A. Pilvar, J. Plutzky and D. Roblyer, “Enhanced peripheral tissue oxygenation and hemoglobin concentration after a high-fat meal measured with spatial frequency domain imaging,” *Biophotonics Discov.*, 1 (2), 025004 <https://doi.org/10.1117/1.BIOS.1.2.025004> (2024).

[97] A. Pilvar et al., “Feasibility of postprandial optical scattering of lipoproteins in blood as an optical marker of cardiovascular disease risk: modeling and experimental validation,” *J. Biomed. Opt.*, 28 (6), 065002 <https://doi.org/10.1117/1.JBO.28.6.065002> JBOPFO 1083-3668 (2023).

[98] R. M. Pope and E. S. Fry, “Absorption spectrum (380–700 nm) of pure water II integrating cavity measurements,” *Appl. Opt.*, 36 (33), 8710 <https://doi.org/10.1364/AO.36.008710> APOPAI 0003-6935 (1997).

[99] J. T. Kuenstner and K. H. Norris, “Spectrophotometry of human hemoglobin in the near infrared region from 1000 to 2500 nm,” *J. Near Infrared Spectrosc.*, 2 (2), 59 –65 <https://doi.org/10.1255/jnirs.32> (1994).

[100] L. Hacker et al., “A stable phantom material for optical and acoustic imaging,” *J. Vis. Exp.*, 196 e65475 <https://doi.org/10.3791/65475> (2023).

[101] D. Han et al., “Thermal properties of carbon black aqueous nanofluids for solar absorption,” *Nanoscale Res. Lett.*, 6 (1), 457 <https://doi.org/10.1186/1556-276X-6-457> NRNAAD 1556-276X (2011).

[102] C.-H. Hung et al., “Broadband absorption and reduced scattering spectra of in-vivo skin can be noninvasively determined using δ -P₁ approximation based spectral analysis,” *Biomed. Opt. Express*, 6 (2), 443 <https://doi.org/10.1364/BOE.6.000443> BOEICL 2156-7085 (2015).

[103] S. Kedenburg et al., “Linear refractive index and absorption measurements of nonlinear optical liquids in the visible and near-infrared spectral region,” *Opt. Mater. Express*, 2 1588 –1611 <https://doi.org/10.1364/OME.2.001588> (2012).

[104] J. Lepock, H. Frey and K. Ritchie, “Protein denaturation in intact hepatocytes and isolated cellular organelles during heat shock,” *J. Cell Biol.*, 122 (6), 1267 –1276 <https://doi.org/10.1083/jcb.122.6.1267> JCLBA3 0021-9525 (1993).

[105] T. Yu et al., “Quantitative analysis of dehydration in porcine skin for assessing mechanism of optical clearing,” *J. Biomed. Opt.*, 16 (9), 095002 <https://doi.org/10.1117/1.3621515> JBOPFO 1083-3668 (2011).

[106] P. Przybylek, “Determination of mineral oil concentration in the mixture with synthetic ester using near-infrared spectroscopy,” *Energies*, 16 (17), 6381 <https://doi.org/10.3390/en16176381> NRGSDB 0165-2117 (2023).

[107] S. L. Jacques, “Chapter 5 Monte Carlo modeling of light transport in tissue (steady state and time of flight),” *Optical-Thermal Response of Laser-Irradiated Tissue*, 109 – 143 2nd ed. Springer, London (2011). Google Scholar

[108] K. J. Hackney et al., “Skeletal muscle volume following dehydration induced by exercise in heat,” *Extrem. Physiol. Med.*, 1 (1), 3 <https://doi.org/10.1186/2046-7648-1-3> (2012).

[109] S. Shenoy et al., “Development and validation of a skin fold thickness prediction equation for Asian Indians using hydrodensitometry,” *J. Obes. Overweight*, 2 (1), <https://doi.org/10.15744/2455-7633.2.102> (2016).

[110] E. Maneas et al., “Gel wax-based tissue-mimicking phantoms for multispectral photoacoustic imaging,” *Biomed. Opt. Express*, 9 (3), 1151 <https://doi.org/10.1364/BOE.9.001151> BOEICL 2156-7085 (2018).

[111] H. H. Mitchell et al., “The chemical composition of the adult human body and its bearing on the biochemistry of growth,” *J. Biol. Chem.*, 158 (3), 625 –637 [https://doi.org/10.1016/S0021-9258\(19\)51339-4](https://doi.org/10.1016/S0021-9258(19)51339-4) JBCHA3 0021-9258 (1945).

[112] S. Merritt et al., “Comparison of water and lipid content measurements using diffuse optical spectroscopy and MRI in emulsion phantoms,” *Technol. Cancer Res. Treat.*, 2 (6), 563 –569 <https://doi.org/10.1177/153303460300200608> (2003).

[113] B. J. Tromberg, TM2B.2 OSA, Washington, D.C. (2016).

[114] S. Prahl, "Optical absorption of hemoglobin," <https://omlc.org/spectra/hemoglobin/>

[115] S. H. Chung et al., "In vivo water state measurements in breast cancer using broadband diffuse optical spectroscopy," *Phys Med Biol*, vol. 53, no. 23, 2008, doi: 10.1088/0031-9155/53/23/005.

[116] Sekar SK, Bargigia I, Mora AD, Taroni P, Ruggeri A, Tosi A, Pifferi A, Farina A. Diffuse optical characterization of collagen absorption from 500 to 1700 nm. *J Biomed Opt*. 2017 Jan 1;22(1):15006. doi: 10.1117/1.JBO.22.1.015006. PMID: 28138693.

[117] Carlos A. Gómez, Darren Roblyer, "Effects of skin tone and adipose thickness on frequency domain near-infrared spectroscopy and diffuse correlation spectroscopy," *Biophoton. Discovery* 2(1) 012503 (6 December 2024) <https://doi.org/10.1117/1.BIOS.2.1.012503>

[118] Mourant JR, Freyer JP, Hielscher AH, Eick AA, Shen D, Johnson TM. Mechanisms of light scattering from biological cells relevant to noninvasive optical-tissue diagnostics. *Appl Opt*. 1998 Jun 1;37(16):3586-93. doi: 10.1364/ao.37.003586. PMID: 18273328.

[119] Tabassum S, Tank A, Wang F, Karrobi K, Vergato C, Bigio IJ, Waxman DJ, Roblyer D. Optical scattering as an early marker of apoptosis during chemotherapy and antiangiogenic therapy in murine models of prostate and breast cancer. *Neoplasia*. 2021 Mar;23(3):294-303. doi: 10.1016/j.neo.2021.01.005. Epub 2021 Feb 9. PMID: 33578267; PMCID: PMC7881266.

[120] Bigio, I. J., & Fantini, S. (2016). Quantitative Biomedical Optics: Theory, Methods, and Applications. Cambridge: Cambridge University Press.

CURRICULUM VITAE

DIANA SUCIU

(860)-368-1239 |  dsuciu@bu.edu |  [LINKEDIN](#) | Boston, MA

SUMMARY

Results-driven individual with a solid track record in delivering quality work, specializing in biomedical device design and clinical trial research. Strong track record in driving research projects from concept through to clinical trial, ensuring alignment with industry standards and regulatory requirements. Proven ability to lead multidisciplinary teams and deliver innovative solutions through collaboration and effective communication.

EDUCATION

BOSTON UNIVERSITY BOSTON, MA
PH.D, BIOMEDICAL ENGINEERING – OPTICS AND MEDICAL DEVICES
 2020- 2025

CASE WESTERN RESERVE UNIVERSITY CLEVELAND, OH
MS, BIOMEDICAL ENGINEERING – NEURAL ENGINEERING
 2016-2018
BS, BIOMEDICAL ENGINEERING – DEVICES & INSTRUMENTATION
 2013-2017

RESEARCH PROJECTS

BOSTON UNIVERSITY
 APRIL 2021– PRESENT

ADVISOR: DR. DARREN ROBLYER BOSTON, MA

- *Created a prototype combined frequency domain-broadband diffuse optical spectroscopy system for continuous, non-invasive human measurements.*
- *Conducted a multi-year clinical trial testing a prototype optical device on patients undergoing hemodialysis to monitor fluid volume status and tissue optical properties.*
- *Collaborated with multidisciplinary teams to design, implement, and analyze clinical protocols, including patient recruitment, data collection, and analysis.*
- *Managed all stages of the trial, including regulatory compliance, data integrity, and reporting of findings.*

CASE WESTERN RESERVE UNIVERSITY NEURAL ENGINEERING CENTER
SEPTEMBER 2015 –AUGUST 2018

ADVISOR: DR. DOMINIQUE DURAND

CLEVELAND, OH

- *Designed a series of experiments to test correlations between metastatic breast cancer growth and neural activity in mice under mentorship of Dr. Dominique Durand.*
- *Performed data analysis on long-term neural recordings and bioluminescence imaging (BLI) to identify correlations between neural activity and tumor growth.*
- *Developed and implemented surgical techniques to safely implant electrodes into mice with breast cancer.*
- *Designed and created custom microelectrodes for neural signal recording and stimulation, enabling precise monitoring of neural activity in vivo*

WORK EXPERIENCE

BIOMEDICAL ENGINEER
2019-2020

DEPARTMENT OF VETERAN'S AFFAIRS

CLEVELAND, OH

- *Designed and implemented experiments focused on restoring sensation to patients with missing lower limbs as part of Dr. Ronald Triolo's research initiatives.*
- *Developed and programmed wearable stimulator devices to provide continuous lower limb sensation for patients enrolled in a take-home pilot study.*
- *Prepared monthly and quarterly reports for DARPA and the Department of Defense (DoD) to communicate progress, results, and ongoing research developments.*
- *Managed lab environment, ensuring daily technical staff availability and providing support to maintain efficient day-to-day operations.*

RESEARCH ENGINEER
2018-2019

CLEVELAND CLINIC

CLEVELAND, OH

- *Wrote and submitted grant proposals to secure funding for research initiatives at the Cleveland Clinic Hand Research Laboratory.*

- *Designed and implemented experiments for clinical trials focused on alleviating symptoms of carpal tunnel syndrome.*
- *Conducted preliminary clinical studies on patients with carpal tunnel syndrome, analyzing data and reporting findings.*
- *Composed, submitted, and managed Institutional Review Board (IRB) applications and other essential research documentation as the Hand Lab's study coordinator.*
- *Mentored graduate students, providing support through study design, research, and thesis writing in preparation of academic milestones.*

PUBLICATIONS

- **Suciù, D., Pham, T., Lin, L., Guruprasad, S., & Roblyer, D.** (April 2025). “Frequency Domain Broadband Shortwave Infrared Spectroscopy for Measurement of Tissue Optical Properties from 685 – 1300 nm”. *Journal of Biomedical Optics*. doi: [10.1117/1.JBO.30.4.045001](https://doi.org/10.1117/1.JBO.30.4.045001)
- **McCallum, G. A., Shiralkar, J., Suciu, D., Covarrubias, G., Yu, J. S., Karathanasis, E., & Durand, D. M.** (2020). “Chronic Neural Activity Recorded within Breast Tumors”. *Scientific Reports*, 10, Article 14824. doi: [10.1038/s41598-020-71670-y](https://doi.org/10.1038/s41598-020-71670-y).
- **Suciù, D. J.** (2018). “Neural Activity Within Solid Breast Tumors and the Implications on Metastasis” (Master’s Thesis). Case Western Reserve University: [OhioLink](#).
- **Suciù, D.** (2015). “Contraception or Bust: Marketing Around the Comstock Laws”. *Essay winner for USNA 287Q Gothic Science, SAGES 2015, Case Western Reserve University. Republished (2020) by the Dittrick Museum of Medical History.*

CONFERENCES

- **Suciù, D., Pham, T., Lin Wei, L., Chitalia, V., & Roblyer, D.** (2025). “Broadband Frequency Domain Near Infrared Spectroscopy for Fluid Volume Status Monitoring During Hemodialysis”. *Oral presentation at SPIE 13314, Optical Tomography and Spectroscopy of Tissue XVI, San Francisco, CA.*
- **Pham, T., Suciu, D., Lin Wei, L., Guruprasad, s., & Roblyer, D.** (2025). “Frequency-Domain Broadband Shortwave Infrared Spectroscopy for Noninvasive Monitoring of Tissue Optical Properties”. *Oral presentation at SPIE 13314, Optical Tomography and Spectroscopy of Tissue XVI, San Francisco, CA.*
- **Suciù, D., Pham, T., Lin, L., Chitalia, V., & Roblyer, D.** (2024). “Frequency Domain Shortwave Infrared Spectroscopy for Non-Invasive Measurement of Tissue Optical Properties”. *Oral presentation at SPIE 12827-27, Multiscale Imaging and Spectroscopy, San Francisco, CA.*

PROFESSIONAL DEVELOPMENT

- *C3i Advanced Product Development Course, Virtual Fall 2022 - Spring 2023*
- *Presented “Optical Kidney Dialysis Monitoring Project” C3i Conference, Dallas, TX (oral presentation) April 2023*
- *eC3i Product Development Course, Virtual Summer 2022*

PROFESSIONAL SOCIETIES

Order of the Engineer*2017-Present****Society of Photo-Optical Instrumentation Engineers (SPIE)****2021-Present****The National Society of Collegiate Scholars****2016-Present****Women in Science and Engineering (WISE)****2013-Present*

LEADERSHIP POSITIONS

Volunteer and Teacher - Society of Creative Anacronyms*2018-Present****Lab Manager- Cleveland Clinic****2018****President - Case Western Medieval Combat Club****2014-2017****Lead Teacher- i2Camp, Cybersecurity****Summer 2016****Teacher’s Aide-i2Camp, Robotics and Electronics****Summer 2014*

Skills

Technical Skills: DOS, BLI, Ultrasound Imaging, MRI Segmentation, Onshape, Prototyping, Data Analysis

Machining Skills: Soldering, 3D Printing, Drill Press, Band Saw, Dermal, Molding, Casting

Clinical Trial Skills: Grant Writing, Management, IRB Document Organization, Regulatory compliance, Recruitment

Interpersonal Skills: Positive Influence/Leadership in Team Based Environments, Conflict Resolution, Attention to Detail

Programing Languages: Matlab, Python, Arduino, R